UNIVERSITY OF BELGRADE

FACULTY OF PHYSICS

Miloš Lj. Ranković

Photon and electron action spectroscopy of trapped biomolecular ions - From isolated to nanosolvated species

Ph.D. Thesis

INSTITUTE OF PHYSICS BELGRADE

Belgrade, 2016.

UNIVERZITET U BEOGRADU

FIZIČKI FAKULTET

Miloš Lj. Ranković

Fotonska i elektronska akciona spektroskopija trapiranih biomolekularnih jona - od izolovanih do nanosolvatisanih čestica

Doktroska Disertacija

INSITUT ZA FIZIKU U BEOGRADU

Beograd, 2016.

Podaci o mentoru i članovima komisije

Mentor: dr Aleksandar Milosavljević, Naučni savetnik,
Institut za fiziku u Beogradu

Članovi komisije:

dr Bratislav Marinković
Naučni savetnik, Institut za fiziku u Beogradu

dr Alexandre Giuliani
Beamline scientist, synchrotron SOLEIL, France

Prof. dr Dragoljub Belić
Redovni profesor, Fizički fakultet, Univerzitet u Beogradu

Prof. dr Goran Poparić
Vanredni profesor, Fizički fakultet, Univerzitet u Beogradu

Prof. dr Nataša Nedeljković
Redovni profesor, Fizički fakultet, Univerzitet u Beogradu

Acknowledgements

The work presented in this Thesis was performed both in the Laboratory for Atomic Collision Processes, Institute of Physics Belgrade and at the beamlines DESIRS and PLEIADES of the SOLEIL synchrotron, France, during multiple beamtimes. All experiments were carried out under the supervision of my advisor Dr. Aleksandar Milosavljević, to whom I express my sincere gratitude. I would also like to thank Aleksandar for his help in writing this Thesis, his patience during the years, for answering all of my questions, for numerous advice and suggestions, for his trust and for always inspiring me to go forward.

During the past four years, we closely worked with Dr. Alexandre Giuliani from the SOLEIL, who always encouraged and supported me during my work as a Ph.D. student. I am very grateful for his suggestions, patience and help in both conducting the experiments and understanding the obtained results.

I would also like to thank Dr. Laurent Nahon, the DESIRS beamline manager, Dr. Cristophe Nicolas, the PLEIADES beamline scientist, Dr. Viktor Cerovski from Belgrade and Dr. Francis Canon from Dijon, for their help and interesting discussions during the beamtimes, as well as the SOLEIL general staff for running the beam smoothly.

I would like to thank Dr. Alexandre Giuliani, Dr. Bratislav Marinković, Prof. Dr. Dragoljub Belić, Prof. Dr. Goran Poparić and Prof. Dr. Nataša Nedeljković for accepting to be in the Commission Panel for the assessment of my Thesis, and for very useful suggestions and comments.

I am grateful to our technician Mr. Miroslav Maksimović for very useful suggestions and help in designing and assembling the experimental parts. Also, I would like to thank my father Mr. Ljubiša Ranković and Mr. Živko Sević for their help in designing and testing the custom electrical circuits.

I would like to thank my colleagues from the Institute of Physics in Belgrade, Dr. Jelena Maljković, Dr. Sanja Tošić, Dr. Predrag Kolraž, Dr. Dragutin Šević, Dr. Maja Rabasović, Dr. Jozo Jureta, Dr. Branko Tomčik, Mr. Andrej Bunjac, Dr. Nenad Simonović, Dr. Duška Popović and Dr. Tasko Grozdanov for their support and useful suggestions. I would like to thank Ph.D. students Mr. Ilija Simonović, Mrs. Tatjana Agatonović-Jovin and Ms. Nataša Tomić for their support during the hard times.

Finally, I am very grateful to my family, friends and Ms. Aleksandra Terzić for their understanding, help and support.

Belgrade, 15.04.2016.

Photon and electron action spectroscopy of trapped biomolecular ions – From isolated to nanosolvated species

In an effort to understand the vast complexity of the underlying processes within a cell at a molecular level, the first step lies in revealing the fundamental physical and chemical properties, as well as the structure, of biopolymers (proteins and DNA). With the development of modern experimental techniques it has become possible to study these large molecules under well-defined conditions in the gas phase, by closely inspecting their interactions with energetic photons and electrons.

In this Thesis, we present the experimental setups for the action spectroscopy of peptides, proteins and nucleotides, as well as the hydrated complexes (hydrated nucleotides), in the gas phase. We present the details and the operation of the two experimental setups based on coupling the linear quadrupole ion trap with: (1) a VUV or a soft X-ray synchrotron beamline and (2) a focusing electron gun.

In the case (1), the existing experimental setup consisting of a commercial quadrupole ion trap mass spectrometer (LTQ XL from Thermo Scientific), equipped with an electrospray ion source, was coupled to the VUV beamline DESIRS and the soft X-ray beamline PLEIADES at the synchrotron SOLEIL (France). The setups were used to study the photo-induced ionization/fragmentation of trapped biopolymers and nanosolvated species. The results obtained with this setups include VUV action spectroscopy of protonated Leucine-Enkephalin peptide (both a monomer and a dimer) and a nanosolvated nucleotide Adenosine monophosphate (AMP), in (5-15) eV photon energy range. The inner-shell action spectroscopy in the soft X-ray energy range (around C and N K-edge), was performed for multiply charged precursor of Ubiquitin protein. The photo-dissociation and photo-fragmentation ion yields for several fragment ions from all above mentioned macromolecules were extracted and the obtained spectral features were discussed considering relevant photon-induced processes.

In the case (2), new experimental setup was developed by coupling the same LTQ XL ion trap with a focusing electron gun, in order to perform an electron activation tandem mass spectrometry, as well as an electron-impact action spectroscopy of trapped biopolymer ions. The ion optic simulations using SIMION program were performed in order to investigate the propagation of the electron beam in the RF+DC ion trap. Tests measurements for electron-induced fragmentation of Substance P, Melittin and Ubiquitin are presented for the impact energy of 300 eV. Finally, we present the electron-impact inner-shell action spectroscopy of the multiply charged Ubiquitin protein, in the vicinity of C K-edge energies of (280-300) eV. The electron-impact results are compared with the soft X-ray photon-impact action spectroscopy results obtained for the same target.

Keywords: Mass spectrometry, Action spectroscopy, Photo-dissociation, Electron-induced dissociation, Synchrotron radiation, Electrospray ionization, Linear quadrupole ion trap, SIMION, Peptides, Proteins, Hydrated nucleotides.

Scientific field: Physics
Field of academic expertise: Atomic and molecular physics
UDC number: 539.2

Fotonska i elektronska akciona spektroskopija trapiranih biomolekularnih jona - od izolovanih do nanosolvatisanih čestica

U nastojanju da se razume ogromna složenost procesa u okviru ćelije na molekulskom nivou, prvi korak je otkrivanje fundamentalnih fizičko-hemijskih osobina, kao i strukture biopolimera (proteina i DNK). Razvojem savremenih eksperimentalnih tehnika omogućeno je proučavanje velikih biološki relevantnih molekula pod jasno definisanim uslovima u gasnoj fazi, izučavanjem njihovih interakcija sa fotonima i elektronima velikih energija.

U ovom radu su predstavljene eksperimentalne postavke za akcionu spektroskopiju peptida, proteina, nukleotida, kao i nanosolvatisanih kompleksa (hidratisani nukleotidi) u gasnoj fazi. Prikazani su detalji i princip rada dve eksperimentalne postavke zasnovane na povezivanju linearne kvadrupolne jonske zamke sa: (1) sinhrotronskim fotonskim mlazom (VUV i meki X-zraci) i (2) fokusirajućim elektronskim topom.

U slucaju (1), postojeća eksperimentalna aparatura koja sadrži linearnu kvadrupolnu jonsku zamku u okviru komercijalnog masenog spektrometra (LTQ XL od firme Thermo Scientific) povezana je sa VUV mlaznom linijom DESIRS i mlaznom linijom za meke X-zrake PLEIADES na sinhrotronu SOLEIL (Francuska). Aparatura je upotrebljena za izučavanje foto-indukovanih procesa jonizacije i fragmentacije zarobljenih jona biopolimera i nanosolvatisanih čestica. Rezultati dobijeni na ovoj aparaturi uključuju VUV akcionu spektroskopiju protonisanog leucin-enkefalin peptida (monomer i dimer), kao i nanosolvatisanog nukleotida adenosin monofosfata (AMP), u opsegu energija fotona od (5-15) eV. Akciona spektroskopija unutrašnje ljuske koristeći meke X-zrake (u oblasti C i N K-ljuske), urađena je za višestruko naelektrisani prekursor proteina ubikuitin. Za sve gore pomenute makromolekule, izučavani su absorpcioni spektri za neke od dobijenih jonskih produkata, pri čemu su analizirane uočene spektralne karakteristike dobijene u pomenutim fotonski indukovanim procesima.

U slucaju (2) razvijen je novi eksperimentalni sistem zasnovan na povezivanju iste LTQ XL jonske zamke sa elektronskim topim sa mlazom elektrona srednjih energija, koja omogućava tandem masenu spektrometriju i elektronski indukovanu akcionu spektroskopiju zarobljenih jona biopolimera. Korišćenjem programa SIMION, urađene su simulacije sa ciljem ispitivanja transmisije elektrona kroz jonsku zamku sa RF+DC potencijalima. Inicijalni testovi aparature uradjeni su fragmentacijom peptida supstance P i melitin, kao i ubikuitin proteina pri energijama elektrona u oblasti oko 300 eV. Na kraju, prikazani su rezultati elektronski-indukovane akcione spektroskopije višestruko naelektrisaniog jona ubikuitin proteina, u oblasti energija oko C K-ljuske (280-300) eV. Ovi rezultati su upoređeni sa rezultatima dobijenim za istu metu pri fotonski-indukovanim (X-zraci) procesima iz iste oblasti energija.

Ključne reči: Masena spektrometrija, Akciona spektroskopija, Foto-disocijacija, Elektronski indukovana disocijacija, Sinhrotronsko zračenje, Linearna kvadrupolna jonska zamka, Peptidi, Proteini, Hidratisani nukleotidi.

Naučna oblast: Fizika
Uža naučna oblast: Fizika atoma i molekula
UDK broj: 539.2

Contents

Biography

Publications

1 Introduction

The possibility to experimentally investigate the interactions of photons and electrons with large biopolymers such as peptides, proteins, nucleotides or complex weakly bound biological systems (for example hydrated biopolymers), in the gas phase under well-defined conditions, is of a great scientific importance. Such investigations provide more insights into fundamental physical and chemical properties, which lead to a better understanding of both their biological functions in the living organisms and the radiation damage on the molecular level.

A vast number of experimental studies performed on biopolymers are focused on revealing their electronic structures, ionization energies, bond energies, primary structures (amino acid sequences) and secondary structures (three-dimensional arrangements). It is also important to explore correlations between the electronic structure of large biopolymers, which is defined by their atomistic representation (governed by the laws of quantum mechanics) and the spatial arrangement of these macromolecules (which defines their active biological function). Understanding these relations could help developing a method for modeling the functions of biopolymers - a subject of much interest in the wide field of science.

Moreover, the study of the interaction of photons and electrons with isolated biological macromolecules helps to understand the radiation damage processes, which is important for the development of new and more efficient methods in medicine, for example in the therapy of cancers [1]. The interaction of UV radiation with DNA molecule was for many years a subject of an intensive theoretical and experimental research. It is known that DNA molecule very efficiently absorbs electromagnetic radiation in the ultraviolet (UV) region, but on the other hand, it is rather stable against the UV-induced destruction.

Out of all secondary products generated by the primary radiation, electrons are the most abundant. They can effectively interact with the constituents of DNA and induce braking of single and double chains of DNA (single and double strand brakes). Therefore, a huge number of studies of the interactions of electrons and isolated molecules, which are parts of the large macromolecules [2, 3] have been performed. However, the majority of the experimental research, both for the photons and electrons, has been conducted either with solvents or with relatively small molecules, which are isolated parts of the biopolymers.

1.1 Ion spectroscopy

In order to study the interaction of electrons and photons with large isolated biopolymers, it is necessary to somehow transfer these molecules in the gas phase. At the end of the last century, modern ionization techniques were developed, which enabled the isolation and the study of large molecular ions, in the gas phase. For example, electrospray ionization (ESI) [4] is a method which allows for very large (kDa) and fragile biomolecules to be introduced from a solution, without degradation, into the gas phase. Furthermore, these ions can be isolated in a variety of high charge states (which is determined by the number of added or removed protons). The development of modern ionization techniques enabled the use of the mass spectrometry (MS) method for investigating the structure of macromolecules. Particularly, the ability of MS to selectively manipulate with ions according to their mass to charge ratio - m/z [5], coupled with spectroscopic techniques, lead to a new field called ion spectroscopy.

However, photon or electron spectroscopy of large macromolecular ions in the gas phase remains experimentally very challenging. First of all, due to the space charge, it is impossible to obtain a high concentration of target particles in the interaction volume. On the other hand, the classical sources of high-energy photons cannot provide sufficient beam intensities that would allow obtaining measurable and statistically reliable results in classical crossed beam experiments. Therefore, vacuum UV (VUV) and X-ray spectroscopy of macromolecular ions in the gas phase, were practically inaccessible until recently. Nevertheless, the experimental techniques based on isolation (trapping) of size-selected clusters [6] and Xenon ions [7], have demonstrated the possibilities to apply this method on biological macromolecules.

The first coupling of a linear ion trap integrated within the commercial mass spectrometer (Thermo Scientific LTQ XL) to the VUV beamline DESIRS [8] at the synchrotron SOLEIL facility in France, has been done by A. Milosavljević et al [9–12]. A similar project with coupling an ion trap to the VUV beamline at the synchrotron BESSY II in Germany was carried out by S. Bari et al [13] and O. Gonzalez et al [14]. These experimental setups offer a unique opportunity to study photo-induced dynamics and electronic properties of macromolecules (for example proteins), using action spectroscopy of trapped ions in a high vacuum. Moreover, these experiments demonstrated that high-energy photons can be used as a new activation method intended for protein sequencing, which allows fast and intensive fragmentation, as well as the mapping of weakly bound complexes [15].

The protein damage also needs to be taken into account in order to perform realistic modeling of the radiation damage. So far, the majority of the reported experimental results were focused on VUV photon interaction with their building blocks - amino acids (for example [16, 17]). However, proteins do not necessarily have to inherit the VUV/X-ray susceptibility of their constituent amino acids. Recently, A. Milosavljević et al [18] demonstrated that an isolated protein was very resistant to soft X-ray fragmentation in comparison with isolated amino acids. Therefore, the studies of energetic photon interactions with the isolated polymers of amino acids (peptides) are also very important.

The structure and function of biomolecules are closely linked with their aqueous environment. For this reason, there has been a long standing effort to understand the influence of solvent molecules in the immediate surroundings on the three-dimensional structure of biopolymers (such as proteins and DNA) [19]. It is believed that the weak molecular interactions play an important role in the folding of the protein and formation of macromolecular complexes. The solvation may play a key role in this process. Hence, studies of nanosolvated systems under well-defined conditions could help bridging the gap between the results obtained for biomolecules isolated in the gas phase and their applications in real biological systems.

Finally, the experimental research of interaction of electrons with trapped molecular ions represents an additional level of challenge. Unlike photons, electrons are charged particles and therefore are susceptible to electric fields that are used to capture ions, as well as by the space charge effects induced by the tightly packed ions. On the other hand, the electron beam itself can disturb the electric fields inside the ion trap, which are necessary for an efficient ion trapping. The first experiments of this type that are focused on the interaction of electrons with large isolated biopolymers were made with very low-energy electrons in the experiments involving Furrier transform ion cyclotron resonance (FT-ICR) ion traps. The first experiments of this type were carried out in the group of Zubarev [20, 21]. However, the work of this and other groups was primarily focused on the development of a new activation method for the protein sequencing, but not for the electron spectroscopy of large biopolymers over a wide range of energies.

2 Biomolecules

2.1 Amino acids

Amino acids are organic molecules, which contain an amino group (-NH_2) and a carboxylic acid group (-COOH), as depicted in Figure 2.1. Taking all combinations into account there is an infinite number of amino acids which could be formed, but only around 22 can be found in nature [22, 23]. Each standard amino acid is characterized by a different functional side chain, which is attached to the alpha Carbon C_α (see Figure 2.1). The standard amino acids are joined with one and three letter code [24].

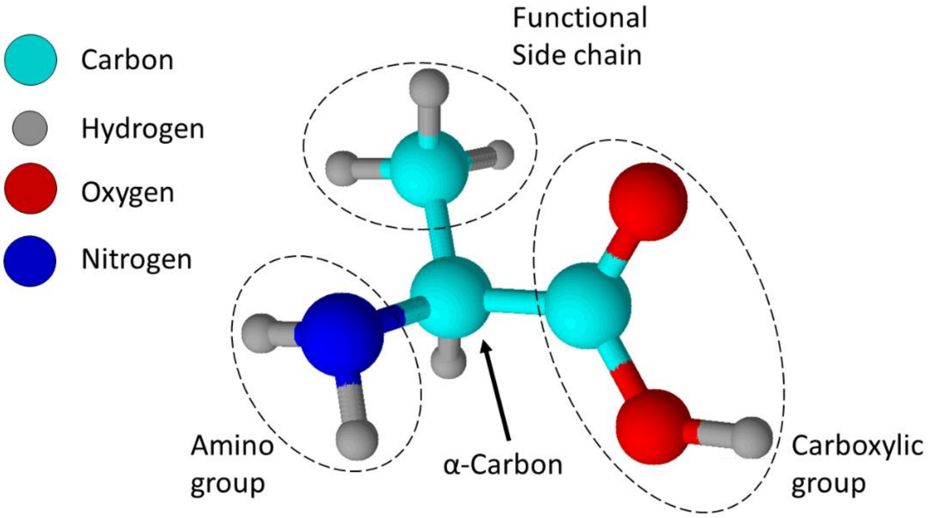

Figure 2.1 - Representation of Alanine amino acid. Alpha Carbon - C_α is the so-called backbone Carbon atom which binds all three functional groups.

2.2 Peptides

Peptides are organic molecules consisted of two or more amino acids linked together through the so-called peptide bonds. This bond is formed when the amino group of one amino acid reacts with the carboxyl group of another amino acid resulting in a covalent bond between the Nitrogen (N) and the Carbon (C). During this process, a water molecule is released, as depicted in Figure 2.2. The peptide C-N bond has partially double bond properties because it is influenced by two strong resonance electron structures. One such structure is a double bond between C and Oxygen (O) atoms and the other one is a double bond between C and N atoms. Atoms O, C, N and Hydrogen (H) involved in this bond belong to a peptide group. The coulomb interaction between atoms from a peptide group creates such electron density distribution that the involved atoms are approximately arranged in a plane. Because of this, the peptide bond is prone to rotation along the axis defined by the peptide bond. This gives peptides the possibility to change their three-dimensional structure by folding.

Peptides are named by the sequence of appearance of their amino acids starting from the N-terminal part of the peptide. This amino acid sequence is also termed the primary structure of the peptide. The spatial arrangement is termed the secondary structure.

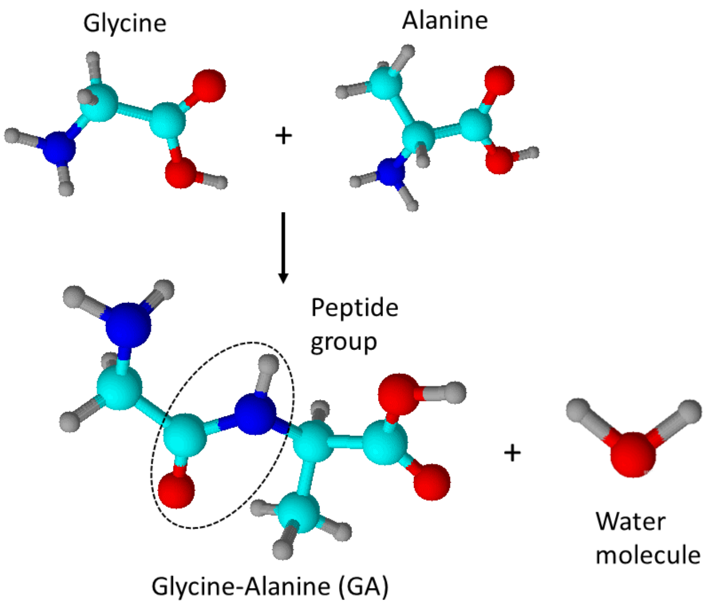

Figure 2.2 - Schematic representation of a formation of a dipeptide composed of amino acids Glycine and Alanine. In this process, a water molecule is released.

The side of the peptide bearing the NH_2 group is termed the N-terminal part. Likewise, the other side of the peptide bearing the acidic function is termed the C-terminal part. A standard nomenclature of the fragments is proposed in [24]. The fragments containing the N-terminal are termed a_{n}-, b_{n}-, and c_{n}- fragments, while the ones containing the C-terminal are termed x_n, y_n, and z_n- fragments (Figure 2.3). The number n in the subscript indicate the number of amino acid residues.

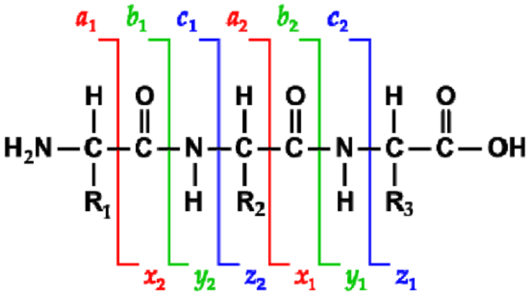

Figure 2.3 - Nomenclature for peptide fragmentation. Image adopted from [25].

Peptides can be linked together to form a large polymer chain called proteins, which can consist up to thousands of amino acid residues [23]. Finding a protein sequence is called protein sequencing. It is found that the three-dimensional structure of a protein is closely related to its biological activity in a living cell [26]. Therefore, a very important goal of mass spectrometry (Section 4.2) is to obtain the primary structure of a protein.

3 Density functional theory (DFT)

Description and evolution of any system in the molecular physics or quantum chemistry is given by the time-dependent non-relativistic Schrödinger equation:

$$\hat{H}\Psi_i = E_i \Psi_i \tag{3.1}$$

Hamiltonian $\hat{H}$ of the system that consists of M nuclei and N electrons can be written as:

$$\hat{H} = -\frac{1}{2}\sum_{i=1}^{N}\nabla_i^2 - \frac{1}{2}\sum_{A=1}^{M}\frac{1}{M_A}\nabla_A^2 - \sum_{i=1}^{N}\sum_{A=1}^{M}\frac{Z_A}{r_{iA}} + \sum_{i=1}^{N}\sum_{j>i}^{M}\frac{1}{r_{ij}} + \sum_{A=1}^{N}\sum_{B>A}^{M}\frac{Z_A Z_B}{R_{AB}} \tag{3.2}$$

Numerators A, B run over all nuclei and i, j run over all electron coordinates. The first two terms are the kinetic energy of electrons and nuclei respectively. The remaining three terms are the electrostatic interaction between nuclei and electrons, the repulsive electron-electron interaction and the repulsive nucleus-nucleus interaction, respectively.

In the Born-Oppenheimer approximation (BOA), due to the large mass difference, the electrons can be considered to move in the fields of the much slower nuclei, while the kinetic energy of the nuclei is a constant (set to zero). Therefore, in BOA the electronic Hamiltonian is given by the following equation:

$$\hat{H}_{elec} = -\frac{1}{2}\sum_{i=1}^{N}\nabla_i^2 - \sum_{i=1}^{N}\sum_{A=1}^{M}\frac{Z_A}{r_{iA}} + \sum_{i=1}^{N}\sum_{j>i}^{M}\frac{1}{r_{ij}} = \hat{T} + \hat{V}_{Ne} + \hat{V}_{ee} \tag{3.3}$$

$$\hat{H}_{elec}\psi_{elec} = E_{elec}\psi_{elec} \tag{3.4}$$

$$E_{tot} = E_{elec} + E_{nucl} \text{ where } E_{nucl} = \sum_{A=1}^{N}\sum_{B>A}^{M}\frac{Z_A Z_B}{R_{AB}} \tag{3.5}$$

The electronic Hamiltonian $\hat{H}_{elec}$ is rewritten as the sum of electron kinetic energy $\hat{T}$, external (nuclear) potential $\hat{V}_{Ne}$, and electron-electron interaction $\hat{V}_{ee}$. Schrödinger equation (3.4) can now be solved for electronic energies E_{elec} and wave functions ψ_{elec} depending on static nuclear coordinates.

The Hartree-Fock (HF) method states that N-body wave function for a fermionic system in the ground state Ψ_0, can be approximated with the Slater determinant, composed from one body wave functions:

$$\Psi_0 \approx \Psi_{HF} = \frac{1}{\sqrt{N}} \begin{vmatrix} \psi_1(\vec{x}_1) & \psi_2(\vec{x}_1) & \cdots & \psi_N(\vec{x}_1) \\ \psi_1(\vec{x}_2) & \psi_2(\vec{x}_2) & \cdots & \psi_N(\vec{x}_2) \\ \vdots & \vdots & \ddots & \vdots \\ \psi_1(\vec{x}_N) & \psi_2(\vec{x}_N) & \cdots & \psi_N(\vec{x}_N) \end{vmatrix} \tag{3.6}$$

First Hohenberg-Kohn theorem [27] demonstrates that the electron density of the ground state ρ_0 for any electronic system uniquely determines the Hamiltonian operator, which describes all properties of the given system. The energy of the ground state is a functional[1] of this density and is given by the relation:

$$E_0(\rho_0) = T(\rho_0) + E_{Ne}(\rho_0) + E_{ee}(\rho_0) \tag{3.7}$$

Second Hohenberg-Kohn theorem states that functional for which the true ground state is obtained, is the one which yields the lowest energy:

$$E_0(\rho_0) \leq E(\rho) = T(\rho) + E_{Ne}(\rho) + E_{ee}(\rho) \tag{3.8}$$

The difficulty arises with this method, because $T(\rho)$ and $E_{ee}(\rho)$ cannot be calculated exactly. One electron Kohn-Sham equations [28] were introduced to utilize the HF orbital method with the modified Slater determinant. In that case, non-interacting particles can be described with:

$$f_{KS}\phi_i = \varepsilon_i \phi_i\,, \tag{3.9}$$

$$\text{where, } f_{KS} = -\frac{1}{2}\Delta + V_S(\vec{r}) \tag{3.10}$$

is the one-electron operator, ϕ_i are one-electron (atomic) orbitals and ε_i is the energy of the state defined by the orbital ϕ_i. Since the orbitals define the state, the electron density can be calculated from $\rho = \sum_{i=1}^{N} \phi_i^* \phi_i$. The kinetic energy of non-interacting electrons is:

$$T_S[\rho] = -\frac{1}{2}\sum_{i=1}^{N} \langle \phi_i | \Delta | \phi_i \rangle \tag{3.11}$$

Therefore, total electron energy functional in Kohn-Scham interpretation can be separated to a non-interacting kinetic energy T_S, an electron Coulomb repulsion term J, electron-nucleus interaction E_{Ne} and the remaining electron-electron exchange term E_{XC}:

$$E_{elec}[\rho] = T_S[\rho] + J[\rho] + E_{Ne}[\rho] + E_{XC}[\rho] \tag{3.12}$$

The correlation exchange term E_{XC} contains corrections for the anti-symmetry which were not included in modified Slater determinant (electrons with antiparallel spins), as

---

[1] A functional is a function of a function. The energy functional outputs the energy from an electron density function $\rho(\vec{r})$.

well as corrections coming from the fact that electrons indeed are interacting. Therefore, the DFT problem lies in finding the exact form of the exchange functional:

$$E_{XC}[\rho] \equiv (T - T_S) + (E_{ee} - J) \tag{3.13}$$

The potential energy can then be calculated by:

$$V_S = \int \frac{\rho_{r_2}}{|\vec{r}_1 - \vec{r}_2|} d\vec{r}_2 - \sum_{A=1}^{M} \frac{Z_i}{|\vec{r}_1 - \vec{R}_2|} + V_{XC} \tag{3.14}$$

$$\text{where } V_{XC} = \frac{\delta E_{XC}}{\delta \rho} \tag{3.15}$$

A large variety of functionals has been developed in order to approximate the correlation exchange term E_{XC}. The most simple one which treats electron density as the homogenous electrons gas is called the local density approximation (LDA). The more advanced one is the generalized gradient approximation (GDA).

4 Experimental methods

4.1 Electrospray ionization

Electrospray ionization (ESI) is a soft ionization technique that allows one to introduce large bio-molecular targets, intact into the gas phase. The first production of the gas-phase ions from liquid solutions was demonstrated by M. Dole in 1968 [29]. Later on, with further developments of the technique by M. Yamashita and J. B. Fenn in 1980's [4, 30] ESI was widely accepted. In the year of 2002, J. Fenn received the Nobel prize in chemistry, for the development of the technique that allowed new insights into the structural analysis of the macromolecules.

The ESI technique is soft in a sense, that a very low amount of energy is deposited in the analyte after the ionization process. When working under normal operating conditions, the residual energy is not enough to induce fragmentation of the analyte [31]. The process of ionization of the analyte by ESI is essentially different in comparison with conventional ionization techniques. For example, in the process of the electron (or photon) impact ionization of atoms or molecules, an electron is removed, creating a positively charged radical ion. In the ESI technique, multiple charging of the analyte is achieved through attachment or detachment, of one or more Hydrogen nuclei - protons. Protonated species are obtained if a proton is attached to the analyte, forming a positive ion - cation. Removal of the proton from the analyte is called deprotonation, yielding a negative ion - anion. ESI allows multiple (de)protonation, as opposite to Matrix assisted laser desorption ionization (MALDI) [32]). Therefore, using the ESI to produce highly charged states of the analytes with large molar weight (> 100 kDa), provides a very important possibility to reduce the mass-to-charge ratio of the target molecule. Mass spectrometers with a modest m/z range, are then able to manipulate with such species. For example, precursor ion of a 7+ charge state of the Ubiquitin protein studied in this Thesis, with a molar weight of 8.5 kDa, has a mass-to-charge ratio of 1225. The general principle of the ESI source is presented in Figure 4.1. An ESI source is usually coupled to the mass spectrometer within one instrument, abbreviated as an ESI-MS device.

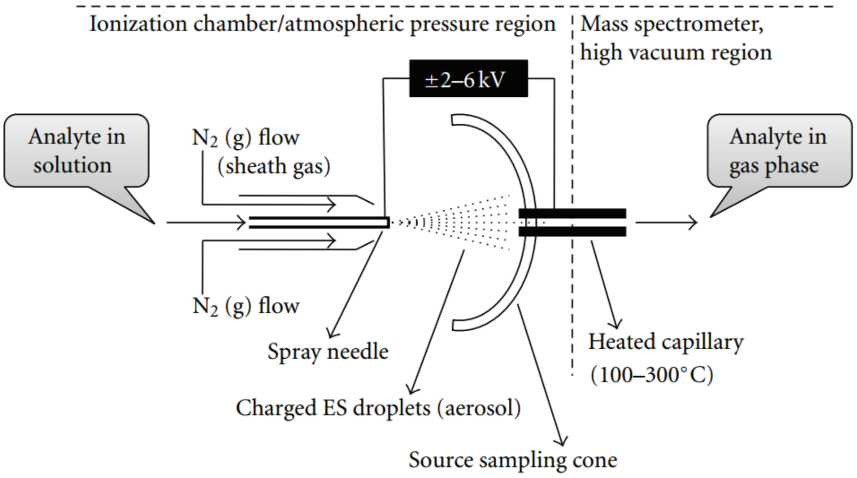

Figure 4.1 - Schematic representation of an electrospray ion source. Adopted from [33].

A mechanical syringe pump forces the solution with the analyte through a stainless steel capillary (spray needle), with an inner diameter of typically 0.1 mm, at a low flow rate in the range of (1-100) µL/min. The capillary tip is polarized to a high voltage of up to ±6 kV, relative to the surrounding counter electrode, positioned 1 to 3 cm from the tip. In order to help the formation of a fine mist and define the direction of the spray, Nitrogen sheath gas is pumped around the capillary to assist the formation of a spray. The counter electrode can either be an ion sweep cone extended into another heated capillary, or just a capillary heated up to the temperatures of 300 °C. Another end of the heated capillary is held at a high vacuum, obtained with a turbo molecular pumps of the mass spectrometer. A very important aspect of the electrospray ion source is that the solution is pumped at an atmospheric pressure into the mass spectrometer, without the need of additional differential pumping. This is because the heated capillary inner diameter (usually 0.2 mm), is small enough to impose a high flow resistance. The length of the capillary which is typically somewhere between 5-10 cm, also contributes to a small flow resistance.

The electrospray ionization process is presented in Figure 4.2. Influenced by the strong gradient of the electric field, the charges in the solution are electrophoretically separated inside the spray capillary. In the positive ion mode, a positive potential is applied, causing the positively charged ions to accumulate at the surface of the solution, near the tip of the spraying capillary. Taylor cone [34] is formed at a critical value of the electric field and a solution is dispersed into aerosol droplets. Droplets are surrounded by positive charges and contain well-preserved analyte molecules. Reversing the polarity of the voltage supply yields a negative ion mode, where negatively charged droplets are obtained. The charges on the surface of the droplet are uniformly distributed since it is a configuration with a minimal potential energy. Two opposing forces act on the droplet. One is Coulomb force, trying to repel the charges and the other one is the surface tension, acting between molecules of the liquid. As the droplets travel towards the counter electrode, the solvent is evaporating with the assistance of a sheath gas, resulting in a droplet size decrease. A Rayleigh limit [35] is reached when the size of the droplet is small enough, that the Coulomb repulsion overcomes the surface tension of the droplet. So-called Coulomb explosion (fission) occurs, breaking the droplet into smaller ones, which contain fewer analyte molecules. At the end, multiply charged molecules are obtained.

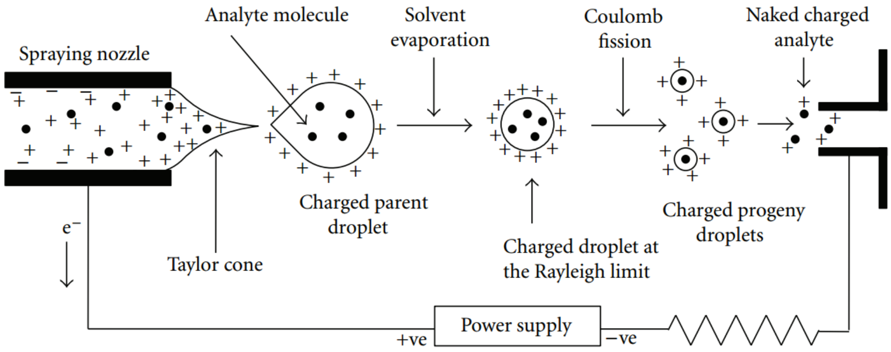

Figure 4.2 - Schematic representation of the electrospray ionization process. Adopted from [33].

Currently, there are two strongly debated theoretical models, which describe the final formation of charged analytes [36]: 1) Ion evaporation model (IEM) and 2) Charge residue model (CRM).

IEM [37] suggests that at a critical radius of the droplet above the Rayleigh limit, at ≥10 nm, the electric field is strong enough to directly evaporate the droplets and form the charged analyte ions. This approach is experimentally well supported for the formation of small organic and inorganic ions like salts.

CRM [29, 38, 39] assumes cascade series of the Coulomb fission events, which leads to a formation of a droplet containing a single analyte molecule. Then by evaporating or complete desolvation, the charged analyte ion is obtained. For larger analytes like proteins, CRM seems more suitable.

Among many variations of the ESI, a nano-electrospray ion source (nano-ESI), developed by Wilm and Mann [40, 41] is widely used. As the name suggests, the main difference between the standard ESI and nano-ESI is in the much smaller size of the capillary allowing lower flow rate. Nano-ESI typically operates with flow rates in the range of (20-50) nL/min. This imposes a big advantage over the standard ESI, where the most of the solution volume is wasted. Moreover, the required amount of the solution in the experiment using nano-ESI is in the order of a few μL, compared to around 1 mL, typically used for standard ESI. The small flow rate is achieved with the use of borosilicate glass spray capillary, with the tip inner diameter of (1-4) μm. Glass capillary is sputtered on the outside with a gold film, in order to enable electrical conductivity. The applied potential is typically in the range of (0.7-1.5) kV. The distance from the tip of the capillary to the ion sweep cone can be much shorter, compared with standard ESI. The presence of the strong electric field initiates the solution flow, which is further propelled by the capillary forces only, as the droplets leave the tip. The Size of the produced droplets by nano-ESI are in the order of 200 nm, whereas 1.5 μm droplets are usually produced by standard ESI. The most attractive feature of the nano-ESI is the favoring of the highly aqueous species. This opens the important possibility to produce a hydrated and charged adducts of the analytes, which were studied in this Thesis.

4.1.1 Sample preparation

The biomolecule samples used in this Thesis, are provided from Sigma Aldrich. They are received in a powder form and require to be prepared in the form of a liquid solution. The obtained solution without further purification was then directly injected into ESI or nano-ESI.

Table 4.1 - Concentrations and solvents of the daughter solutions of the analytes studied in this Thesis.

Analyte	Concentration [μM]	Solvent [vol/vol %]
Leucin Enkephalin	10	water/ACN - 75/25
Adenosine monophospate	100	pure water only
Ubiquitin	10	water/ACN - 70/30
Substance P	10	water/ACN/acetic acid - 49.5/49.5/1
Melittin	100	water/methanol/ - 50/50

In this section, a brief description of the procedure for obtaining such solutions is presented. First, the mother solution is prepared, at a higher concentration of the given analyte, using an appropriate solvent. The mother solution is then diluted to a desired final concentration, obtaining a daughter solution. Solvents used for the daughter solutions were mainly deionized water (max. resistance of 18.6 MΩ) and acetonitrile (ACN) or methanol. Depending on requirements of a particular study a small percentage of the acid could be added to the solvent for the daughter solution. For example, if highly charged positive precursor ions are to be obtained, the acetic acid is added (typically 1%). Basic properties of the daughter solutions of the analyte molecules studied in this Thesis are presented in Table 4.1.

4.2 Mass spectrometry (MS)

Mass spectrometry (MS) has become a very powerful tool for the analysis of the charged particles (ions) [5]. Once the ions are produced in the gas phase by means of the ionization techniques (for example ESI), they need to be separated in some way. The instruments which perform the actual ion separation are called mass analyzers. Rather than separating the ions according to their masses, mass analyzers are designed to select the ions based on their mass-to-charge (m/z) ratios.

In order to achieve the ion selection according to the m/z ratio, mass analyzers are designed to utilize the static or dynamic electric or magnetic fields, either individually or a combination of both. Specific differences between various types of mass analyzers are expressed through the actual applications of magnetic and electric fields. With this respect, different types of mass analyzer used in mass spectrometry are summarized in Table 4.2.

Table 4.2 - Types of mass analyzers. Adopted from [5].

Analyzer type	**Symbol**	**Principle of separation**
Electric sector	E or ESA	kinetic energy
Magnetic sector	B	momentum
Quadrupole	Q	m/z (trajectory stability)
Ion trap	IT	m/z (resonance frequency)
Time-of-flight	TOF	velocity (time of flight)
Fourier transform ion cyclotron resonance	FTICR	m/z (resonance frequency)
Fourier transform orbitrap	FT-OT	m/z (resonance frequency)

Each of the presented types of mass analyzers has its own advantages and disadvantages, which makes it suitable for a certain application. In this Thesis, linear quadrupole ion trap as a part of a commercial mass spectrometer (Thermo Scientific LTQ XL) was used to select and isolate target ions. For this reason, the principle of operation of a quadrupole mass analyzer (filter) is presented in the following section.

4.2.1 Quadrupole analyzer (Mathieu equations)

The principles of guiding and trapping ions are based on generating electric field which imposes a binding force that increases linearly with the particle distance from the axis [42]:

$$\vec{F} = -c\vec{r} \tag{4.1}$$

This force generates the parabolic potential Φ, given by relation:

$$\Phi \sim (\alpha x^2 + \beta y^2 + \gamma z^2) \tag{4.2}$$

Appropriate tools which can generate such potentials and restrict the motion of ions are electric or magnetic multipole fields. If the number of "poles" is labeled with m, then in general case multipole potential is given with the relation:

$$\Phi \sim r^{\frac{m}{2}} \cos(\frac{m}{2}\varphi) \tag{4.3}$$

If a number of multipoles m=4 then quadrupole potential is obtained, where the quadratic potential is $\Phi \sim r^2 \cos 2\varphi$. For electric quadrupole field, the potential in the Cartesian coordinates has the form:

$$\Phi = \frac{\Phi_0}{2r_0^2}(\alpha x^2 + \beta y^2 + \gamma z^2) \tag{4.4}$$

In order to satisfy the Laplace equation $\Delta\phi = 0$, the condition $\alpha + \beta + \gamma = 0$ has to be valid. The imposed condition is valid for two simple cases:

(i) $\alpha = -\gamma = 1,\ \beta = 0$ (2D field) → $$\Phi = \frac{\Phi_0}{2r_0^2}(x^2 - z^2) \tag{4.5}$$

(ii) $\alpha = \beta = 1,\ \gamma = -2$ (3D field) → $$\Phi = \frac{\Phi_0(r^2 - 2z^2)}{r_0^2 + 2z_0^2},\ 2z_0^2 = r_0^2 \tag{4.6}$$

Quadrupole mass filter

Potential obtained in case (i) can be generated by four parallel hyperbolic electrodes extended in Y-axis direction, as depicted in Figure 4.3b.

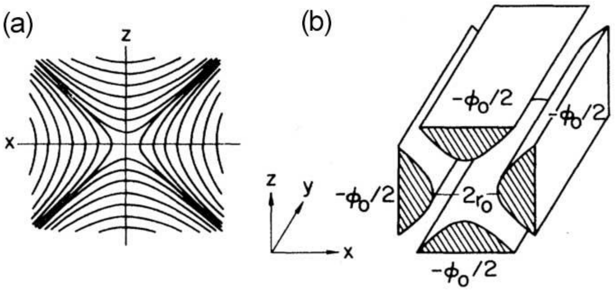

Figure 4.3 - (a) Equipotential lines for a quadrupole field in a plane and (b) Electrode configuration of quadrupole mass filter. Adopted from [42].

Time-dependent potential difference (voltage) applied to electrode pairs of the quadruple mass filter, that results in a restricted ion motion in XZ plane, is given by the following relation:

$$\Phi_0(t) = U + V\cos\omega t\,, \tag{4.7}$$

where U is direct current (DC) voltage and V is the amplitude of the RF voltage with a circular frequency ω. Equations of motion are given by the second Newton law:

$$m\frac{d^2\vec{r}}{dt^2} = -e\nabla\Phi \tag{4.8}$$

$$\ddot{x} + \frac{e}{mr_0^2}(U + V\cos\omega t)x = 0 \tag{4.9}$$

$$\ddot{z} - \frac{e}{mr_0^2}(U + V\cos\omega t)z = 0 \tag{4.10}$$

Equations (4.9) and (4.10) can be simplified by introducing the following parameters:

$$a = \frac{4eU}{mr_0^2\omega^2}\,,\ q = \frac{2eV}{mr_0^2\omega^2}\,,\ \tau = \frac{\omega t}{2} \tag{4.11}$$

$$\begin{aligned} &\frac{d^2x}{d\tau^2} + (a + 2q\cos 2\tau)x = 0 \\ &\frac{d^2z}{d\tau^2} - (a + 2q\cos 2\tau)z = 0 \end{aligned} \tag{4.12}$$

Equations (4.12) are the canonical form of the second-order differential Mathieu equations. There are two types of solution for Mathieu equations: (1) stable motion, where ions oscillate in the XZ plane and are free to move along the Y-axis direction passing through the quadrupole filter; (2) unstable motion, in which their coordinates grow exponentially along X- or Z-axis, or both. For any given ion with mass m and charge e, the stability of its trajectory depends only on parameters a and q, defined by the voltages U and V applied on the quadrupole electrodes. If the relation between parameters a and q is plotted on a graph (see Figure 4.4), the stability diagram is obtained. The stability diagram shows the areas, for which the ion motion is stable in Z- and in the X-axis direction. In a small region near the origin of the diagram, ion motion is stable in both X- and Z-axis directions. A zoom of this region is presented in Figure 4.5.

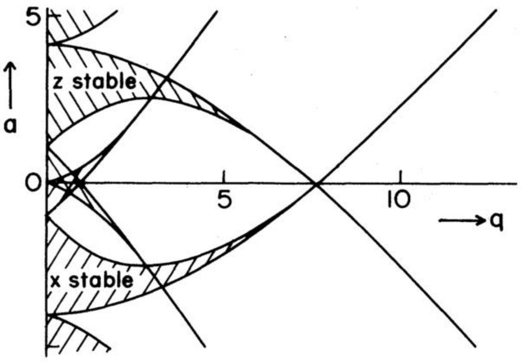

Figure 4.4 - Stability diagram for 2D quadrupole field. Adopted from [42].

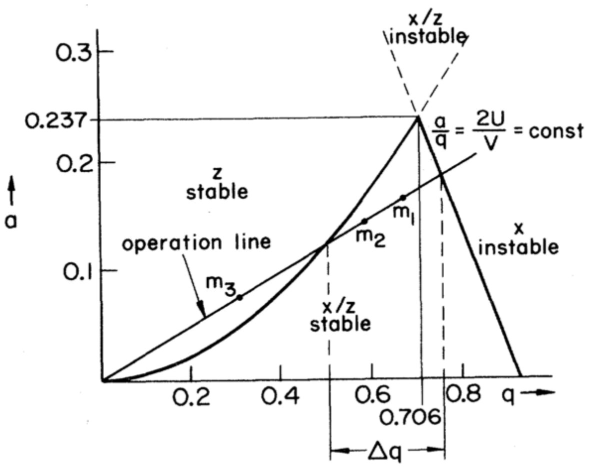

Figure 4.5 - The lowest region of simultaneous stability of ion motion in X- and Z-axis directions. Operation line is defined with the ratio $a/q = \mathrm{const}$, all ion masses are located on this line ($m_3>m_2>m_1$). Adopted from [42].

If the values r_0, ω, U and V are fixed, all ions with the same mass will have the same operating line in the stability diagram. Because the ratio a/q=2U/V does not depend on ion masses, all ion masses lie on the operating line a/q =const. For the stability line on the q axis (a=0, RF only filter), the possible values of parameter q are in the range [0, q_{max}], where q_{max}=0.92. If we put q_{max} in the equation (4.11) for q parameter, we can see that all ions with masses in the range from m_{min} to infinity have stabile trajectories. For such quadrupole field conditions, the quadrupole works as a high-pass mass filter. By increasing the DC voltage U operating line is rising, which decreases the range Δm. At some point, it touches the tip of the stability region, where Δm=0, meaning that in theory ions with only one exact mass will have the stable trajectories. In practice, this is never the case and the mass bandwidth is defined by voltage fluctuations. If voltages U and V are simultaneously changed in a way that their ratio keeps constant, then ions with successive masses will have the stabile trajectories and all other ions will be splatted on electrodes. This operation gives the possibility to scan the mass spectrum, therefore, the quadrupole will work as a mass spectrometer. By adding two more sections (with the same electrode profile) axially before and after the quadrupole mass filter, axial ion trapping can be achieved and thus the linear quadrupole ion trap is obtained.

4.2.2 Tandem mass spectrometry (MS^n)

The principle of tandem mass spectrometry is depicted in Figure 4.6. Once ions are produced in the gas phase, a certain small m/z range is defined by setting the operating line close the tip of the stability diagram, which results in an isolation of precursors with a defined m/z ratio. The selected precursor ions are then activated, which means that their internal energy is increased, and eventually it will lead to the fragmentation. If the activation process is carried out through inelastic collisions with neutral gas atoms (Helium or Nitrogen), the process is called the collision induced dissociation (CID) [43]. Product ions are then analyzed according to their m/z ratio which yields a tandem mass spectrum (MS^2). It should be noted that the process of ion isolation and activation can be repeated further up to the n-th level in ion traps, yielding MS^n. Other activation methods may be also applied, in order to increase the intensity and selectivity of the fragmentation. For example, photons from synchrotron radiation [9, 44], or low energy electrons [45].

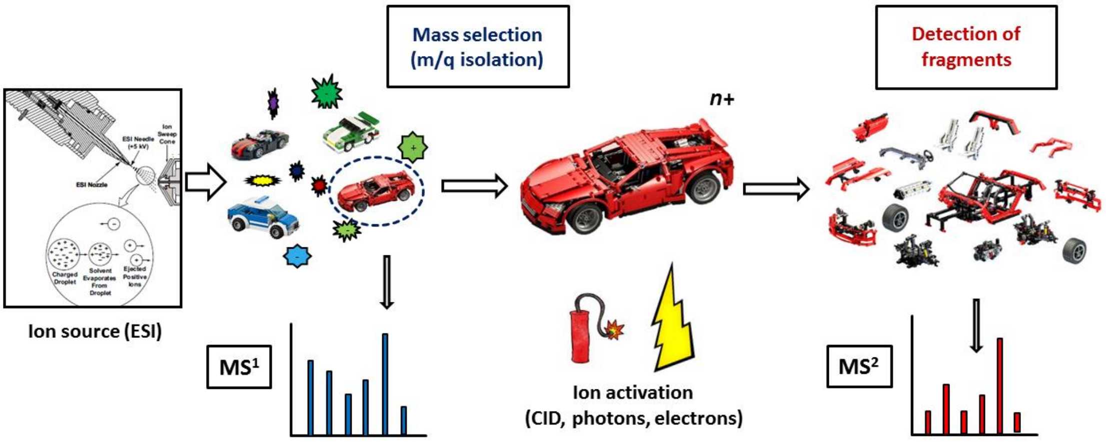

Figure 4.6 - Schematic representation of tandem mass spectrometry (MS^2).

The primary goal of mass spectrometry is to provide the information about the structure of the target precursor ion by analysis of the fragmentation patterns. MS^2 has demonstrated a huge potential to investigate the primary structure of large biopolymers [46].

By repeating photons or electrons activation tandem MS for many activation energies in small energy steps, one obtains the experimental technique called action spectroscopy. Experimental setups presented in this Thesis are based on this technique and were used for investigating the electronic structure of peptides, proteins and nucleotides.

4.3 LTQ XL - details and operation

In this section, details of operation of a commercial mass spectrometer Thermo Scientific LTQ XL (LTQ) are given. LTQ is the main instrument of the experimental setups, presented in this Thesis. Figure 4.7 depicts a functional block diagram of the spectrometer. LTQ comprises three major hardware systems: 1) ion source, 2) MS detector system and 3) data system.

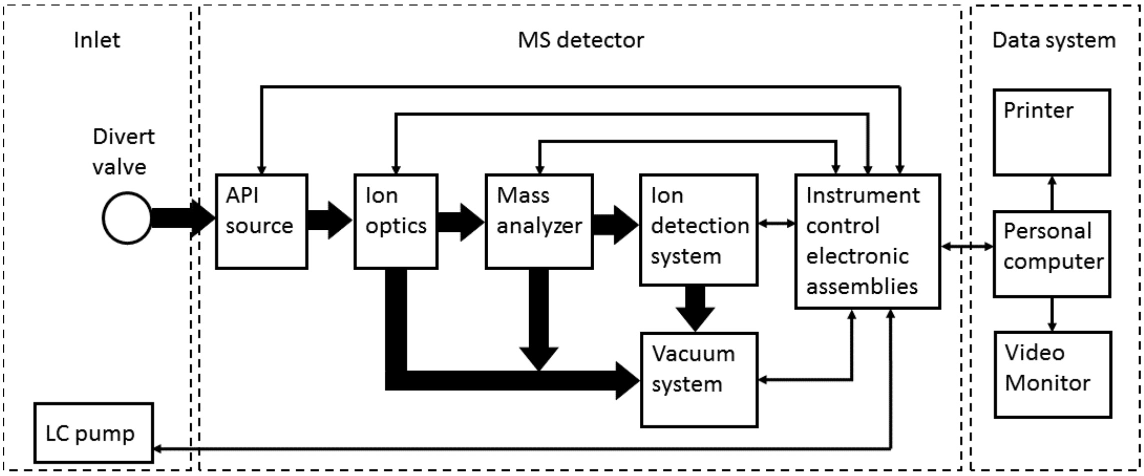

Figure 4.7 - Functional block diagram of LTQ XL mass spectrometer. Adapted from [47].

(1) The atmospheric pressure ionization (API) source is composed of two components. The first component is permanently mounted on the front side of the spectrometer chassis. It consists of an ion sweep cone, a transfer tube (heated capillary), a tube lens and a skimmer (see Figure 4.8). The second component is completely removable and is essentially a spraying needle of an ESI source, in enclosed assembly. Depending on requirements of the experiment, assembly with the standard ESI or a nano-ESI needle is mounted. Analyte solution is automatically injected into a spray needle through flexible capillaries (at a user defined flow rate), with the assistance of a mechanical syringe pump located on the front side of the mass spectrometer.

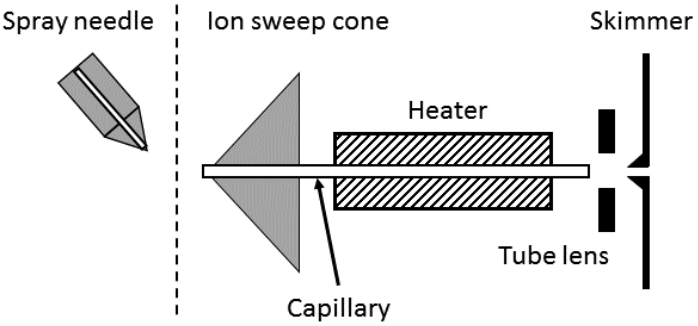

Figure 4.8 - Schematic representation of an API source of the LTQ XL mass spectrometer. Spray needle is a part of an independently detachable assembly - of the standard ESI or a nano-ESI source.

A Standard ESI source is used in this Thesis for producing non-hydrated (bare) charged precursor ions. In general, when using the standard ESI source in the positive mode, precursor ion $[M+nH]^{n+}$ can be produced, where n indicates the ion charge state. Letter M indicates the molar weight of the target molecule, while H denotes the Hydrogen nucleus - proton. Typically, a wide range of precursor charge states are produced simultaneously, with a certain intensity distribution, which depends on solution and ESI parameters. Mass-to-charge ratio (m/z) of such precursor in arbitrary mass units (amu) is given by Equation (4.13).

$$\frac{m}{z}=\frac{M+n}{n} \tag{4.13}$$

Both ESI and Nano ESI are able to produce bare and hydrated precursor ions. In the case of nanosolvated molecules, the general formula for the obtained precursor ions is $[M+kH_2O+nH]^{n+}$, where k is the number of the attached water molecules. In general, Equation (4.14) gives the m/z ratio for the obtained hydrated precursor.

$$\frac{m}{z}=\frac{M+n+18k}{n} \tag{4.14}$$

Since LTQ is designed to efficiently remove remaining water molecules, non-standard ESI parameters had to be used in order to produce hydrated precursors. In the present study, we favorably used nano-ESI in order to produce nanosolvated molecules. Since automatic tuning of nano-ESI parameters was not possible, in order to produce hydrated precursors we reduced capillary temperature well below optimal values, to around 40 °C. The capillary voltage, the sheath gas flow rate and the tube lens voltage also had to be manually retuned accordingly.

(2) The mass spectrum (MS) detector system comprises the ion optics (quadrupole and octupole ion filters), the mass analyzer (a linear quadrupole ion trap), the ion detection

system (electron multiplier detectors) and an electronic control system, as depicted in Figure 4.9.

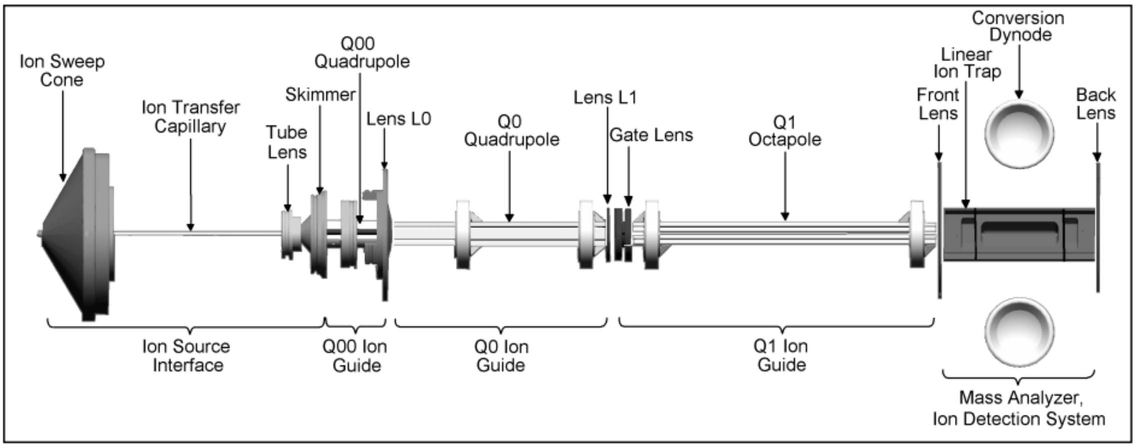

Figure 4.9 - Schematic representation of the LTQ XL mass spectrometer. Adopted from [47].

LTQ allows for sending TTL[2] signals at specific sequence events. These trigger signals can be initiated at the start or at the end of particular processes, during the operation of the device. One such process is the ion activation. In the Xcalibur™ software [47] which runs the LTQ, the option to enable triggers on the activation has to be selected. IF it is enabled, during the activation time TTL signal state is always high (5 V), whereas during all other times TTL signal is kept in the low state (0 V). The activation process in the LTQ is initiated each time when enough ions are stored in the ion trap. In the LTQ software there are two ways to define the ion storage procedure, which then triggers the TTL signal. The first one is by defining the ion storage time limit. This was often used when desired precursor ion abundance was very low, in order to avoid excessively long data acquisition. This means that we prevent LTQ from waiting for optimal ion density in the trap, which lowers the signal to noise ratio. Typically the ion storage time was set to 100 ms. In the case when high ion abundance is obtained, the ion trap capacity can be quickly reached in around (10-30) ms. Therefore, the second way of defining ion storage process is based on measuring the ion density in the ion trap. This process is automatically controlled by internal LTQ electronics and as soon as the optimal capacity is reached TTL signal is triggered to a high 5 V state, signaling the start of activation time (ion irradiation time). The use of mentioned TTL signals is explained in Sections 4.5.2 and 4.5.3.

The ion detection in LTQ is performed by electron multipliers. Schematic representation of the LTQ detection system is presented in Figure 4.10. It comprises a conversion dynode, a series of cathodes and the anode.

---

[2] TTL stands for transistor-transistor logic, representing the binary logic states 0 and 1, with the voltages 0 V and 5 V respectively. TTL signals are used in the digital electronic circuits.

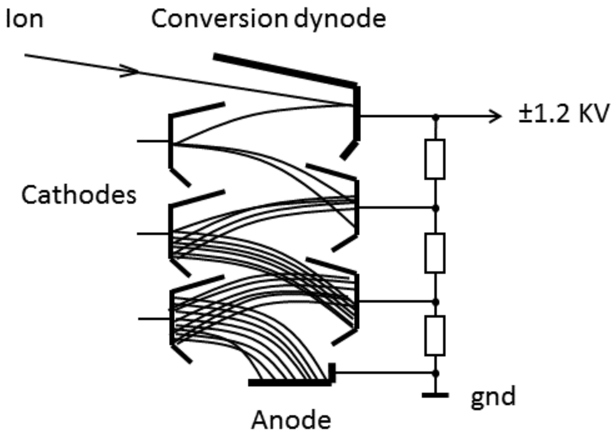

Figure 4.10 - Schematic representation of the electron multiplier detector with conversion dynodes in the LTQ XL mass spectrometer. Two such detectors are located at each side of the ion trap.

Conversion diode is a concave metal surface with a high secondary particle emission coefficient and is positioned at an almost right angle in relation to the incident ion trajectory. If positive ions are to be detected negative voltage is applied, whereas for detection of negative ions a positive voltage is applied to the conversion dynode in relation to the anode potential (ground). The cathodes in between the conversion dynode and the anode are connected to progressively higher voltages through the resistor network. When an ion strikes the conversion dynode one or more secondary electrons are produced. Due to the concave shape and a voltage gradient, secondary electrons are focused and accelerated on the next cathode. Electron striking the inner surface of the cathode ejects more secondary electrons and the process creates the electron avalanche that finally strikes the anode where electrons are collected. Current on the anode is proportional to the number of the ions striking the conversion dynode. This current is additionally amplified in the electronic system of LTQ, converted and stored in a digital form by the data system. Since the electron multipliers are positioned slightly off-axis, background noise from neutral particles is significantly reduced. The electron multipliers are electrostatically shielded which decreases the noise even further.

Linear quadrupole ion trap in the LTQ comprises three axial sections (the same electrode profiles) with three different DC potentials in order to obtain axial ion trapping (see Figure 4.11). In order to create an electric potential well for the trapped ions in the axial direction, the center section DC2 has a different potential in relation to the sections DC1 and DC3. For trapping the positive ions, potential on DC2 is lower, while in order to trap the negative ions the potential on DC2 has to be higher in relation to potentials applied two other sections. The voltage difference is usually not more than 10 V.

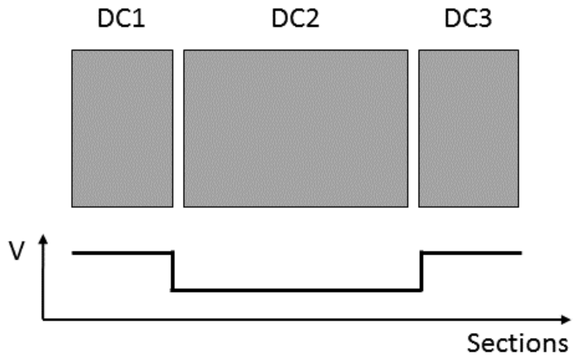

Figure 4.11 - DC voltages on the LTQ ion trap required for axial ion trapping.

Maximal DC voltages are ±100 V, the maximal RF voltage amplitude is 400 V with the frequency of 1 MHz. The ion trap is 68 mm long, with the minimal radial distance between the hyperbolic electrodes of 4 mm.

For the process of ion selection (trapping of desired precursor ions) specific high-frequency pulse is generated by the LTQ electronics. This pulse ejects all ions except the ones corresponding to a small m/z range (isolation width) defined by the user. Typically, we used isolation widths of up to $\Delta m/z = 10$ (±5 from the precursor ion m/z).

After the activation (irradiation) of trapped ions, the ion products are successively ejected by applying different high-frequency detection pulse which ejects all ions with the same m/z. This pulse is quickly ramped so that ions of all m/z are ejected, but in a sorted way from the lowest the highest m/z ratios. After calibration, this procedure yields the action MS^2.

4.4 Synchrotron radiation

Synchrotron radiation (SR) refers to an electromagnetic radiation generated by charged particles when accelerated to the relativistic velocities. SR is first observed in the particle accelerators, used in high energy physics in middle 1940’s. At the time, SR was considered as a byproduct, imposing not yet explained energy loss to the accelerated charged particles. Shortly after, it was realized that the missing energy is due to photon emission. The theory describing SR in circular accelerators is reported by Ivanenko and Pommeranchuck in 1944 [48] and also by Schwinger in 1946 [49, 50] independently. Only later in the 1960’s, the possibility to use the SR in spectroscopic studies was demonstrated [51–54]. A good overview of the development of the SR is reported by Kuntz et al [55].

A storage ring is the most commonly used type of the particle accelerator, designed specifically for the production of the SR and represent the first generation of synchrotron radiation sources. It is constructed of many straight sections arranged in a polygon, with a dipole bending magnets residing in between. In modern synchrotrons, electrons are first accelerated in a smaller ring to the relativistic energies of up to a few GeV and then injected in the storage ring. In a storage ring electrons follow a straight path until reaching the dipole magnets, where their trajectory is bent, experiencing an angular acceleration. At these points, photons are emitted in the tangent direction in the form of SR. Due to the photon emission, electrons in a storage ring lose energy. This energy is recovered by radiofrequency cavities, hence the term synchrotrons. The radiation from a bending magnet is characterized by the linear polarization in the plane of the electron orbit. Synchrotrons that produce SR with bending magnets belong to the second generation of synchrotrons, dedicated to study specifically the SR. Third generation synchrotrons utilize insertion devices installed on the straight sections of the storage ring. Also, in this type of synchrotrons, electrons are repeatedly injected in the storage ring in order to maintain the electron current. In the year of 1986, Klaus Halbach invented insertion devices called undulator, which comprises periodic series of dipole magnets arranged linearly (see Figure 4.12). The electron beam passes longitudinally through the alternating dipole array resulting in a radial acceleration many times, which leads to an electron oscillatory trajectory in the horizontal plane. Due to the relatively weak magnetic field, the radiation cones emitted at each bend overlap with each other which results in a constructive interference and formation of spectrally very narrow peaks. Therefore, SR obtained from an undulator is composed of harmonics and its Brilliance [equation (4.15)] is many orders of magnitude higher compared to the SR generated by the bending magnet. Furthermore, radiation obtained from an undulator is in general elliptically polarized. For this reason, in modern synchrotrons, the polarization can be tuned to linear, horizontal or circular (or any other). Tuning the wavelength of SR produced by an undulator is performed by means of mechanical adjusting of the vertical distance (gap) between the pole tips.

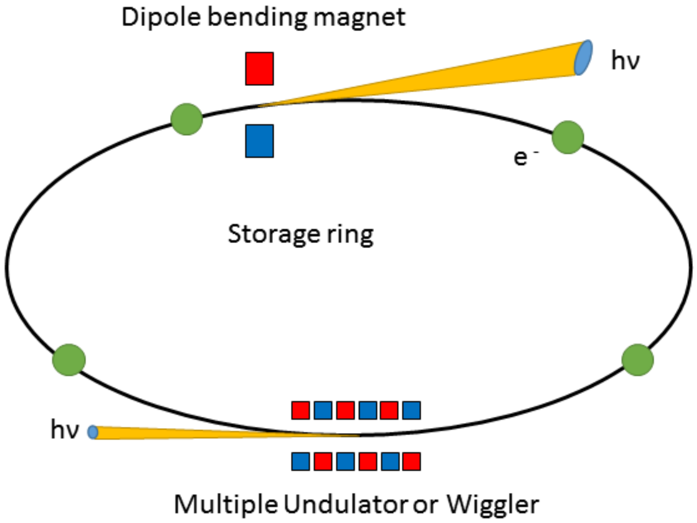

Figure 4.12 - Schematic representation of the synchrotron radiation source. The electron storage ring is composed of many straight sections, connected by the dipole bending magnets. An undulator or wiggler is installed along the straight portions of the storage ring.

In order to compare SR sources of different kinds, a measure of the quality of the source called Brilliance is introduced. It is defined by the following relation:

$$\text{Brilliance} = \frac{\mathrm{N}}{\mathrm{t} \cdot \mathrm{d}\theta \cdot \mathrm{A} \cdot 0.1\%\mathrm{BW}} \, (=) \left[\frac{\text{photons}}{\mathrm{s} \cdot \mathrm{mrad}^2 \cdot \mathrm{mm}^2 \cdot 0.1\%\mathrm{BW}} \right] \qquad (4.15)$$

where N - the number of photons, t - time, dθ - angle divergence, A - cross section of the photon beam and 0.1%BW - denotes a bandwidth $10^{-3}\omega$ centered around frequency ω.

The key features of the SR are:

- Wide energy range covering THz to hard X-rays
- High brilliance
- High collimation (small dθ)
- Time-resolved pulsed light (in nanoseconds)
- High level of polarization (linear, circular or elliptical)

Synchrotron SOLEIL

Experimental results presented in this Thesis are obtained at the synchrotron SOLEIL radiation facility near Paris, France. Specifically, the experiments were performed at the beamlines DESIRS [8] and PLEIADES. In the following paragraphs, a brief description of the most important aspects of the synchrotron SOLEIL and the mentioned beamlines are presented. Figure 4.13 presents the simplified schematic of the SOLEIL synchrotron. It is a third generation synchrotron, with a total of 29 beamlines, covering a very wide range of photon energies in the range (10^{-4}-10^{5}) eV.

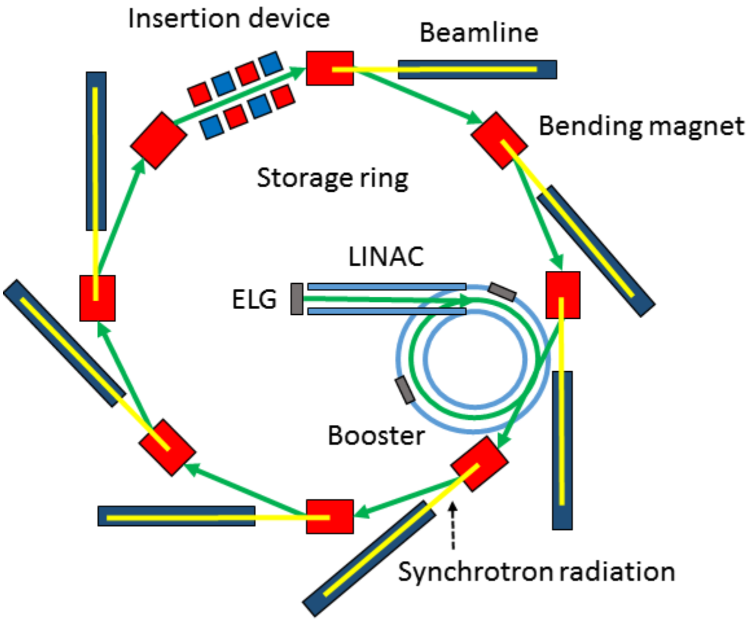

Figure 4.13 - Simplified schematic representation of the SOLEIL synchrotron.

Briefly, the electron gun produces bunches of electrons accelerated in a linear accelerator (LINAC) to 100 MeV. Electrons are then additionally accelerated in a smaller ring (booster), up to the nominal relativistic energy of 2.75 GeV and injected into a storage ring. The bending magnets, undulators and wigglers are positioned around the 345 m circumference of the storage ring, where SR is generated. At these points the photon energy range is from far IR (~1 mm) to hard X-rays (0.012 nm).

4.4.1 DESIRS beamline

The DESIRS [8] beamline is a vacuum ultra-violet (VUV) beamline, with a photon energy range of (5-40) eV. It uses an undulator to produce VUV light, with fully adjustable polarization. Equipped with a gas filter, which effectively cuts off the higher orders of the radiation, this beamline opens up the possibility to perform experiments with a high spectral purity in the low VUV region. The beamline (see Figure 4.14) has three different branches (A, B and C), with the one end station (on branches B) available for user particular experimental setups. Branch C is a permanent experimental setup for Furrier transform absorption spectroscopy (FTS), with an ultra-high resolving power of 10^6 at 10 eV. After passing through the gas filter the light produced by undulator can be split in two directions: to the branch C or to the normal incidence monochromator (NIM). After the NIM, the monochromatized beam can be split and directed to the brunches A or B. The branch A comprises multipurpose molecular beam chamber, SAPHIRS, consisting of a source chamber and an ionization chamber separated by a skimmer. With maximum resolving power of $2x10^5$, the B brunch is open for user's setups. At this branch we have coupled our experimental setup, consisting of a dedicated vacuum stage and a mass spectrometer, equipped with an ESI source.

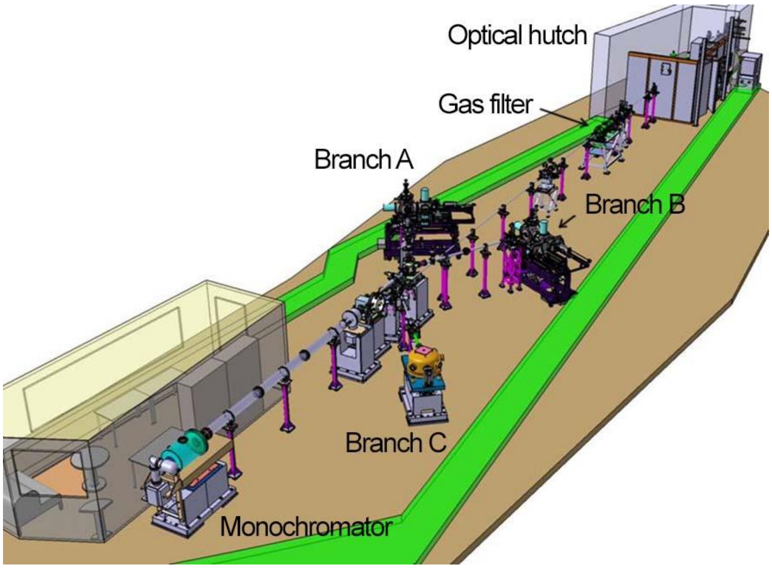

Figure 4.14 - Schematic representation of DESIRS beamline. Adopted from [8].

4.4.2 PLEIADES beamline

PLEIADES beamline is a soft X-ray beamline, capable of producing photons with an energy range of (10-1000) eV, with very high resolving power (10^5 is obtained at the energy of 50 eV). The beamline comprises two undulators with either permanent magnets or electromagnets. It can produce horizontal and vertical linearly polarized light down to energies of 10 eV. Above energies of 55 eV, fully adjustable polarized light is available. This beamline is characterized by a very high energy resolution and brilliance in a wide energy range of the soft X-ray photon beam due to the quasi-periodic design of undulators and varied groove depth of the plane grating. It is also equipped with a high resolution electron spectrometer, Auger electron-ion coincidence setup and a dedicated station for positive and negative ion photoionization studies. It consists of three optical branches with different beam focusing properties.

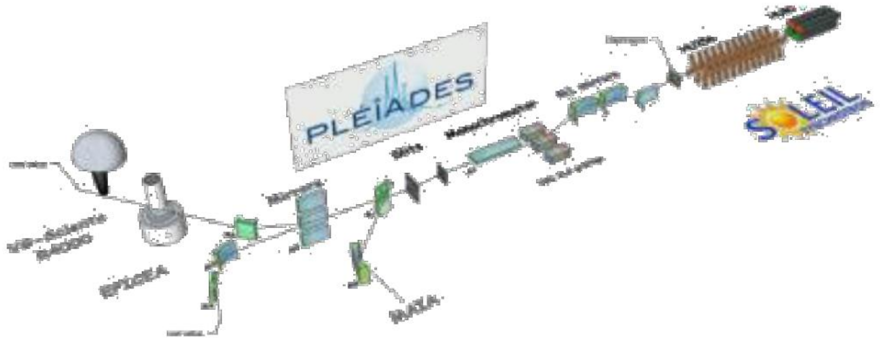

Figure 4.15 - Schematic representation of the PLEIADES beamline. Adopted from [56].

4.5 Photon experimental setup - SRMS2

4.5.1 Vacuum stage, coupling and alignment test

Vacuum stage

For the activation of the trapped ions with the photons from synchrotron radiation, a commercial mass spectrometer Thermo Scientific LTQ XL is coupled to one of the beamlines of the SOLEIL synchrotron facility. In order to couple the LTQ mass spectrometer with the appropriate beamlines a turbo pumping differential vacuum stage was designed by A. Milosavljević et al [9]. 3D model of the vacuum stage assembly is presented in Figure 4.16.

The vacuum stage is based on a six-way cross, with two CF100 and four CF40 flange connections (see Figure 4.16). The main function of the vacuum stage is to maintain the pressure difference between the surroundings of the operating ion trap, which can go down to 10^{-5} mbar and ultrahigh vacuum of the beamline, in the order of 10^{-8} mbar. The actual pressure inside the ion trap is 10^{-3} mbar, because of the Helium buffer gas. For this reason, the vacuum stage is equipped with a 300 L/s turbo pump, installed on the CF100 flange. The beamline is attached to the left side of the vacuum assembly from Figure 4.16, via a short flexible CF40 bellows and a high vacuum valve with a MgF_2 window.

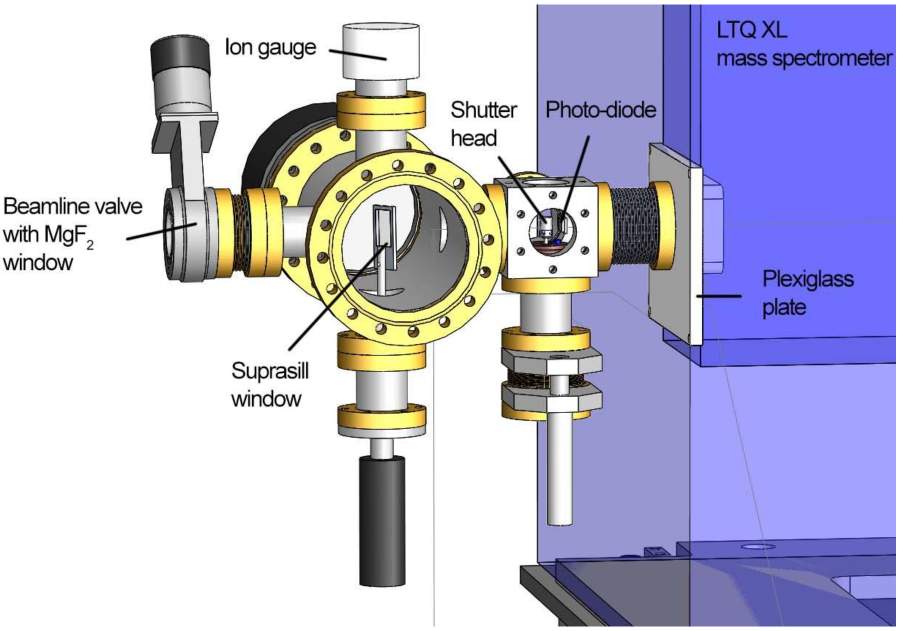

Figure 4.16 - 3D model of the differential turbo pumping assembly fitted with a mechanical shutter, ion gauge, a photodiode and a turbo pump. Designed by A. Milosavljević et al [9].

An ion gauge and Z-axis mechanical manipulator are installed vertically on CF40 flanges. The manipulator is used to optionally insert the Suprasill glass window, in order to cutoff the higher order harmonics of the VUV photon beam above 10 eV (for the lowest incident photon energies used) for improved spectral purity. A photodiode (AXUV100, International Radiation Detectors) and the shutter assembly[3] are coupled to the vacuum stage via a custom made stainless steel box with CF40 coupling. Both the mechanical shutter and the photodiode are installed on the one axis precision manipulators. This enables the fine tuning of the position of the shutter head[4] with respect to photon beam. Moreover, the photodiode can be inserted optionally, in order to measure the photon flux just before the ion trap. The vacuum assembly is rested on a rigid support and positioned behind the LTQ mass spectrometer (at the ion trap side).

In order to precisely align the axis of the ion trap with respect to the photon beam, an adjustable supporting frame was constructed by A. Milosavljević et al [9]. The adjustable

---

[3] Details and operation of the mechanical shutter are presented in Section 4.5.2.

[4] For reference, see Figure 4.22.

frame is positioned on a rigid table and LTQ mass spectrometer is mounted on top of it. Figure 4.17 presents the 3D model of the adjustable supporting frame.

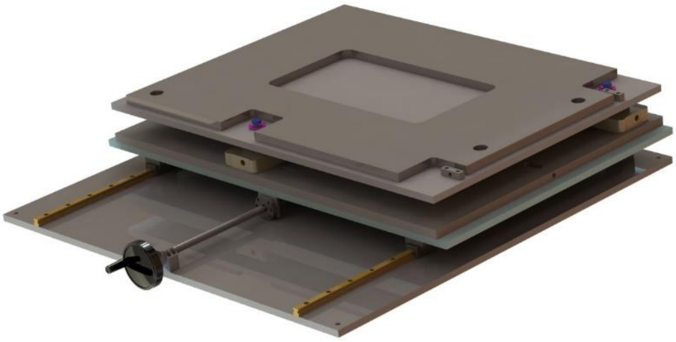

Figure 4.17 - 3D model of the adjustable supporting frame for LTQ mass spectrometer used to precisely align the ion trap axis with respect to the photon beam. Designed by A. Milosavljević et al [9].

The supporting frame is designed to enable fine tuning of the position in 3 translational axes, and 3 rotational axes, covering all degrees of freedom. Adjustments for each axis are realized with the hex key screws. The alignment process is rather tedious and crucially important for obtaining the best overlap of the trapping volume with the photon beam, ensuring the high signal to noise ratio. Figure 4.18 presents a 3D model of final assembly with the vacuum stage, LTQ mass spectrometer, the supporting frame and the carrier table.

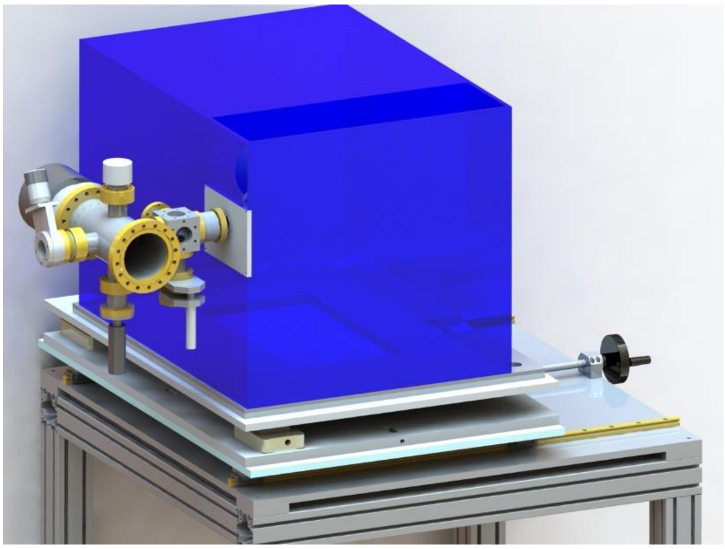

Figure 4.18 - 3D model of the vacuum stage coupled to the LTQ mass spectrometer, installed on an adjustable supporting frame, which is rested on a rigid table. The entire system is mobile. Designed by A. Milosavljević et al [9].

Coupling

The vacuum stage is coupled to the back side of the LTQ mass spectrometer via CF40 flexible bellows. In order to obtain a coupling of the vacuum stage through CF40 bellows to the chassis of the LTQ mass spectrometer, a custom Plexiglas window plate is designed. The back side of the LTQ mass spectrometer was originally sealed with a metal plate. 3D model of the Plexiglass window is presented in Figure 4.19.

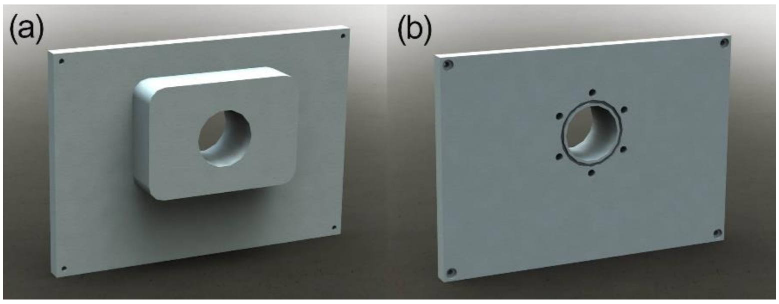

Figure 4.19 - 3D model of the Plexiglass back plate window, designed to couple the vacuum stage to the LTQ XL mass spectrometer: a) back side, positioned towards LTQ and b) front side, with CF40 rubber seal groove and threaded holes. Designed by A. Milosavljević et al [9].

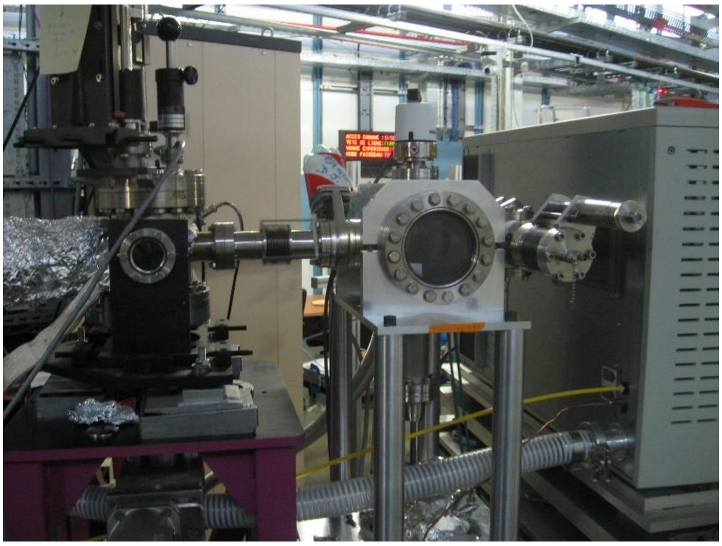

Figure 4.20 - Picture of the experiment with LTQ mass spectrometer coupled to the DESIRS beamline of the SOLEIL synchrotron.

Entire assembly with the LTQ mass spectrometer presented in Figure 4.18, is portable. The carrier table is equipped with small subtractable wheels. This allows for a quick transport of the whole system to another beamline of the synchrotron SOLEIL. With this system, trapped target molecules can be subjected to a wide range of the photon energies, covered by the several beamlines. The system has been so far effectively coupled to the

DESIRS, PLEIADES and DISCO beamlines of the SOLEIL facility, as well as to the keV ion beamline GANIL. The results presented in this Thesis were obtained from the experiments involving the first two mentioned beamlines. A photograph of the coupling the system to the DESIRS beamline is presented in Figure 4.20.

Alignment process

The alignment of the ion trap axis with respect to the photon beam is done in 3 steps. In the first step, before the beamtime and the pumping, the table with the supporting frame and LTQ is positioned roughly into place with respect to the beamline theoretical optical line. If coupled to the DESIRS beamline, the advantage is a still visible part of the zero-th order of the VUV photon beam, which can be detected by eye when reflected from a sheet of white paper. In that case the second step is performed. ESI source is removed from the LTQ mass spectrometer, enabling the clear path of the VUV photon beam, after passing through the ion trap and ion optics. In order for this step of the alignment process to work, both LTQ and vacuum stage have to be brought back to the atmospheric pressure. The beamline coupling valve is closed. Since the moving part of the valve is constructed out of MgF_2 glass window, it is still transparent UV light. The beamline is then set to the lowest possible energy of 4 eV. The UV photon beam can then pass all the way through the ion trap and the ion optics system. Small adjustments are made on the supporting frame, until the bright violet spot is seen on the UV reflective paper positioned just after the ion optics, at the front side of the LTQ mass spectrometer.

In the final third step of the alignment process vacuum stage and LTQ mass spectrometer are pumped to the ultimate pressures of 10^{-6} mbar and 10^{-5} mbar, respectively. Cytochrome C or Insulin precursor ions are electrosprayed and selected in the ion trap[5]. The trapped ions are subjected to the beam of VUV photons, with an energy of 15.4 eV. Figure 4.21 presents the obtained action MS^2 after optimal alignment, obtained for Cytochrome C, 8+ precursor ions.

The MS^2 was normalized to the precursor ion $[M+8H]^{8+}$, designated at m/z 1542. Relaxation channels corresponding to the ionization of the precursor ions with VUV photons appear in the spectrum. Peaks at mass-to-charge ratios of 1370, 1233 and 1121 correspond to radical cations $[M+8H]^{\bullet 9+}$, $[M+8H]^{\bullet 10+}$ and $[M+8H]^{\bullet 11+}$ originating from single, double and triple ionization of the precursor ion, respectively. Optimal alignment was obtained by maximizing the relative intensities of these ion fragments by fine tuning the position of LTQ with the supporting frame.

---

[5] More details about the experimental procedure are presented in Section 4.5.4.

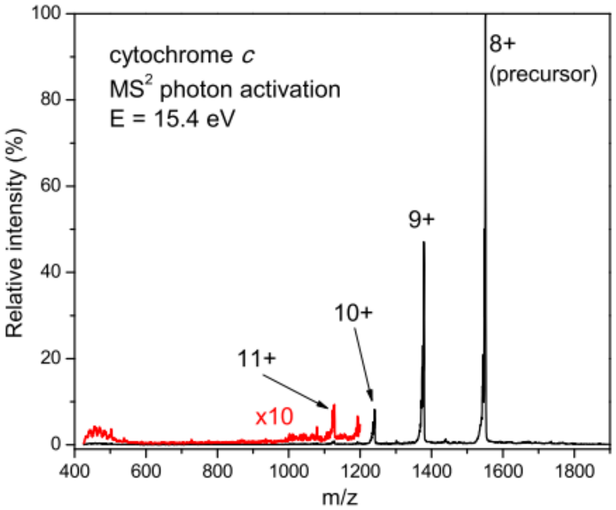

Figure 4.21 - Tandem mass spectrum, recorded for Cytochrome C precursor ions of 8+ charge state, after activation with VUV photons at 15.4 eV energy. Adopted from [57].

4.5.2 Mechanical shutter - design and operation

Photon beam chopping was achieved by positioning the rotating mechanical shutter at its path, just before the entrance to the ion trap. The shutter is designed by A. Milosavljević et al [57] and installed in the turbo vacuum stage. The assembly with the mechanical shutter is presented in Figure 4.22. The mechanical part called shutter head is attached to the shaft of the rotational electric motor *Khunke*, in order to physically block the photon beam. The shutter head is made from Aluminum, with a cylindrical shape and a hole perpendicular to the cylinder axis. The motor is powered by the shutter circuit[6] consisting of a solid state relay connected to the power supply. The motor actuation is initiated by the TTL signal from the LTQ mass spectrometer, whose length is defined by the activation (irradiation) time of the selected ions.

TTL signal line was traced in the electronic board of the LTQ and taken out of the casing. The line of the signal is connected to the input of the shutter circuit and acts as a trigger. Activated by the high state (5 V) of the TTL signal, the shutter circuit drives the electric motor which rotates the shutter head. Optionally, a delay generator is inserted in front of the shutter circuit in order to close the shutter typically 50 ms before the end of the actual activation time. If so, the activation time then has to be set to 50 ms longer. The delay generator is set to activate at the rising edge of the TTL signal sent by the LTQ and to generate a new TTL signal in the phase with the original one (see Figure 4.23). In this way, the interaction of photons with ions is stopped before the detection of the ion fragments. When the activation time runs out and TTL signal goes to 0 V, the mass

---

[6] In the following text term "shutter circuit", will be used to refer to the electrical part of the mechanical shutter in the experiment with photons. In the second part of the Thesis, the same term will be used for different circuit, required in the experiment with electrons.

spectrum is recorded. As a result, the recorded mass spectra showed fairly reduced background signal noise peaks.

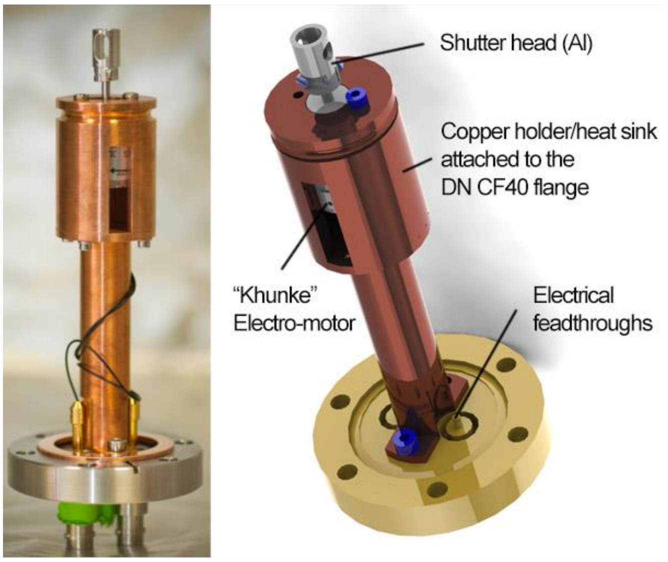

Figure 4.22 - Mechanical shutter for the chopping of the photon beam. Picture of the shutter assembly mounted on a CF40 flange is on the left. 3D model of the shutter assembly is on the right. Adapted from [57].

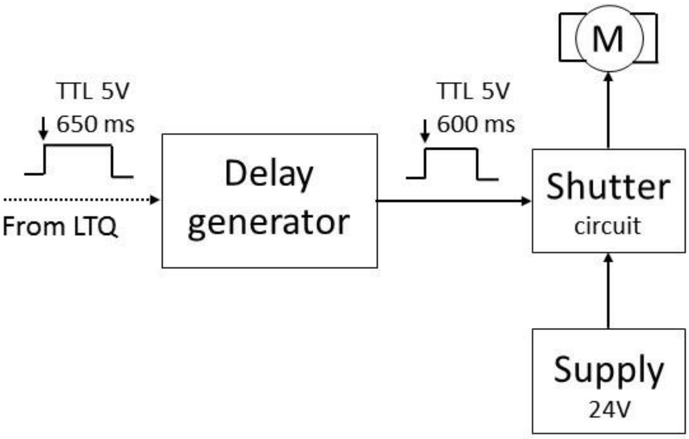

Figure 4.23 - Block diagram with delay generator in front of the shutter circuit, for better signal to noise ratio. TTL signal length of 600 ms is used as an example.

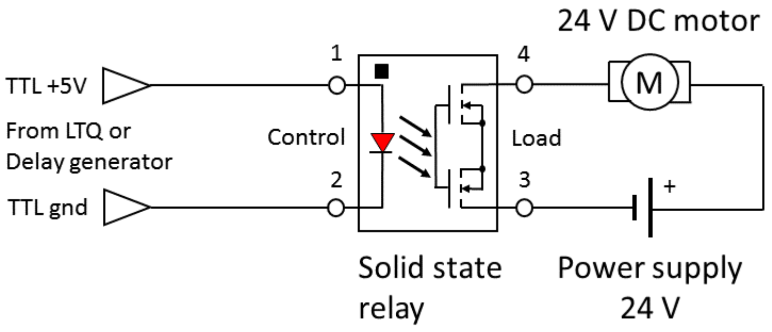

Figure 4.24 - Electrical circuit for the mechanical shutter. Solid state relay (SSR) switch consist of an IR photo-diode and two field effect transistors (FETs) with a photosensitive gate. The high state of TTL signal turns on the photo-diode which results in a closing of the two transistors, closes the circuit on the right side by applying 24 V to the electric motor. The absence of TTL signal (or low state - 0 V) leads to the open circuit and electric motor is not powered.

The electronic circuit for the mechanical shutter is represented by “Shutter circuit” box in Figure 4.23. Actual schematic of the circuit is presented in Figure 4.24. It consists of a solid state relay switch, which connects a power supply of 24 V directly to the electric motor, as long as 5 V TTL signal is present at its input. Applying the 24 V on the motor quickly rotates the shutter head. Mechanical constraints allow the shutter head to rotate only for 90°, locking it in a position such that the hole is parallel with the direction of the photon beam. The shutter head is spring loaded, thus as soon as the motor power is cut, the shutter head is rotated back for 90°, to the position such that the photon beam is blocked.

In order to estimate the shutting speed of the entire shutter system, test measurements are conducted under high vacuum, at the pressure of 10^{-7} mbar. The performance of the mechanical shutter is evaluated by measuring the current from the photodiode (AXUV100, International Radiation Detectors), positioned just after the shutter head in the vacuum assembly. The photodiode current measured with the digital oscilloscope (DG645, Stanford 150 Research Systems, Sunnyvale, CA, USA), was generated by the zero-th order of the VUV light from DESIRS [8] beamline. The signal obtained from the photodiode after applying the power to the shutter motor is presented in Figure 4.25.

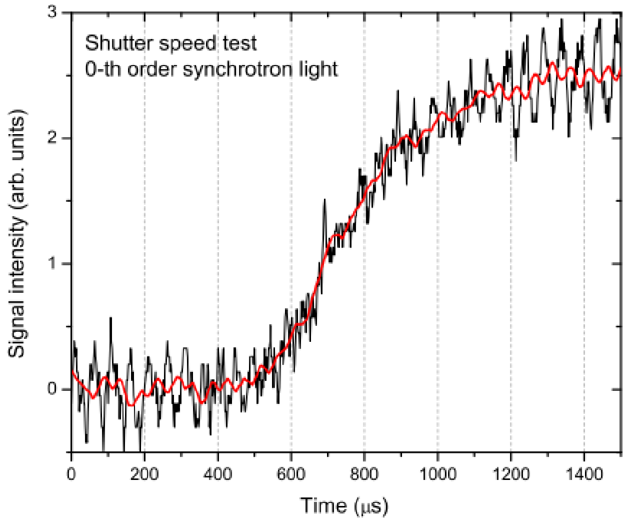

Figure 4.25 - Photodiode current generated by the zero-th order of synchrotron radiation light, measured after opening the mechanical shutter under high vacuum. The red line is generated by 50 point Savitzky Golay smoothing of the obtained signal, in order to reduce the noise. Adopted from [57].

The results of the performance test [57], reveal that the shutter has a systematical delay of about 20 ms, because of the mechanical inertia of the moving parts, although this does not influence the irradiation of trapped ions. The shutting speed was estimated from Figure 4.25, to be around 1 ms.

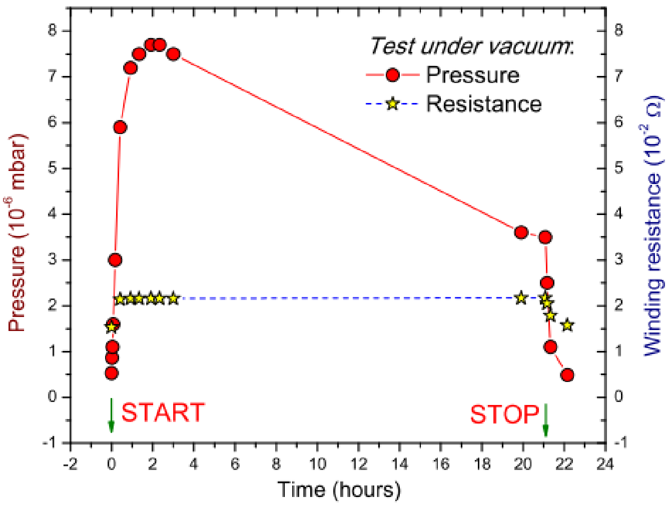

Figure 4.26 - Durability test of the shutter, during 24 hours in vacuum conditions. Shutter motor winding resistance is represented with stars, while circles show the pressure in the vacuum assembly. Adopted from [57].

The resistance of the motor windings was checked under high vacuum conditions, through 24 hour period with a 70 % of the duty cycle. The results of the test [57] are presented in

Figure 4.26. Durability test showed only slightly elevated resistance of the motor windings, proving that large copper holder/heat sink is absorbing most of the generated heat, even under vacuum. The heat from the copper holder is conducted to the vacuum parts of the vacuum stage assembly. The latter is then quickly cooled by the surrounding air at room temperature of 21 °C. The pressure in the vacuum assembly is increased during the first hours of the test due to the degassing of the motor windings. The pressure decrease was observed after 3 hours from starting the test. The resistance of the windings only slightly increased and remained practically constant during the entire test, meaning that the temperature of windings was well below the alarming limits. Both the vacuum stage pressure and motor winding resistance drop to starting values, within an hour after the motor was turned off.

4.5.3 Synchronization with the beamlines

The action spectroscopy of the macromolecular targets presented in this Thesis is achieved through automated acquisition system made by A. Milosavljević and A. Giuliani. The acquisition system is based on the home-made software, which couples two independent hardware components - the LTQ XL mass spectrometer and a synchrotron beamline into one instrument. TTL electric signals are utilized in order to synchronize the operation of these two devices. The control logic for the electric signals is governed by a home-made computer program, written in Igor Pro. The basic principle of the instrument lies in repeating three processes: 1) the ion production and selection, 2) the ion activation at defined energy and 3) the detection of fragments. Each cycle is performed at different activation energy, obtaining activation tandem mass spectra (MS^2) for the desired molecular target. The procedure for the acquisition of many MS^2, for a range of different energies, is defined as an "*energy scan*".

One energy scan consists of a number of energy points, ranging from 10 to 100. A custom temporal sequence is defined and ran for every energy point. One temporal sequence comprises sequential isolation of one or multiple precursors. Individual acquisition (ion irradiation) time length for each precursor is set, which defines the total time length of the sequence. All precursors in the sequence are first subjected to one photon energy and recorded in a "raw file"[7], which contains one mass spectrum for every precursor. The sequence is then repeated until all energy points are scanned. At the end of an energy scan, depending on the number of energy points, the same number of raw files containing all precursor mass spectra is generated. The total time required for one energy scan is determined by the number of energy points multiplied by the time length of the sequence. Typically, for practical reasons, the energy scans were created to last not more than 10 hours.

---

[7] Raw file is the digital computer file format (example scan1.raw) generated by the mass spectrometer software, which contains all data stored during one sequence. This data contains tandem mass spectra and a range of instrumental parameters.

The energy scan process is practically realized by the usage of peripheral controls - *start in* and *ready out*, as an inbuilt hardware option of the LTQ XL mass spectrometer. As their names suggest, *start in* is an input type of connection, while *ready out* serves as an output. Operating principle of these controls is the two state digital logic - TTL. Each control has two contacts, which can be either open (not connected, 5 V) or closed (shorted to the ground, 0 V). LTQ peripheral controls are connected to the PC computer via external USB National Instruments (NI USB-6501) analog-to-digital (AD) card. The computer program was written in Igor Pro software in order to control and automate the entire energy scan process. For the purpose of synchronization, one input and two output connections are utilized from the AD card. A schematic diagram for the digital communication of LTQ mass spectrometer with the DESIRS beamline is presented in the Figure 4.27.

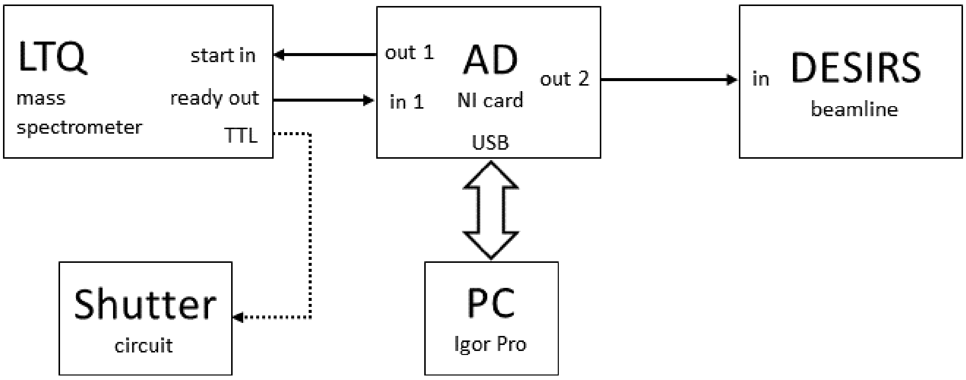

Figure 4.27 - Block diagram for connection of LTQ mass spectrometer with DESIRS beamline.

The LTQ mass spectrometer is set to send 5 V TTL signals in the duration of ion activation time (600 ms in the present case). These signals were traced on the internal board of LTQ, hard wired and taken out of its case, for the synchronization of the shutter circuit. In Figure 4.27 dashed line symbolizes the wire that carries the TTL signal out of the LTQ to the shutter circuit[8].

At the end of each sequence (scan for one energy point has finished) a long contact closure signal (1000 ms) is sent by the LTQ at *ready out*. The long signal is detected by the computer program in Igor Pro, which then sends a TTL signal of 5 V through AD card to the beamline in order to change the photon energy to the next one. Regarding the communication there are two types of beamlines utilized to conduct experiments, whose results are presented in this Thesis. For them, the communication can be one-way (DESIRS beamline), or two ways (PLEIADES beamline).

---

[8] TTL signal can either be connected to the inputs of the circuit for the mechanical shutter Figure 4.24, or the electrical shutter circuit presented in Figure 4.42 in Section 4.6.4.

The one way communication beamline like DESIRS, has the option to only receive signals. It is the reason why the intermediate stage with an AD card and a computer program have to be used. When a sequence is finished, the contact closure at *ready out* is detected by the program. This initiates a TTL signal through the AD card, which is sent to the control input of the DESIRS beamline. The program then waits for a custom defined 5 seconds for the beamline to change the photon energy (wavelength). Waiting period of 5 seconds is determined experimentally as the optimal time window length, during which the DESIRS beamline will certainly finish the wavelength changing process. After this time passes, the program generates a TTL signal and sends it through the out 1 of the AD card to the LTQ *start in* input, as a signal to start the new sequence. The program algorithm is depicted in the Figure 4.28, while the control window of the program is presented in Figure 4.29.

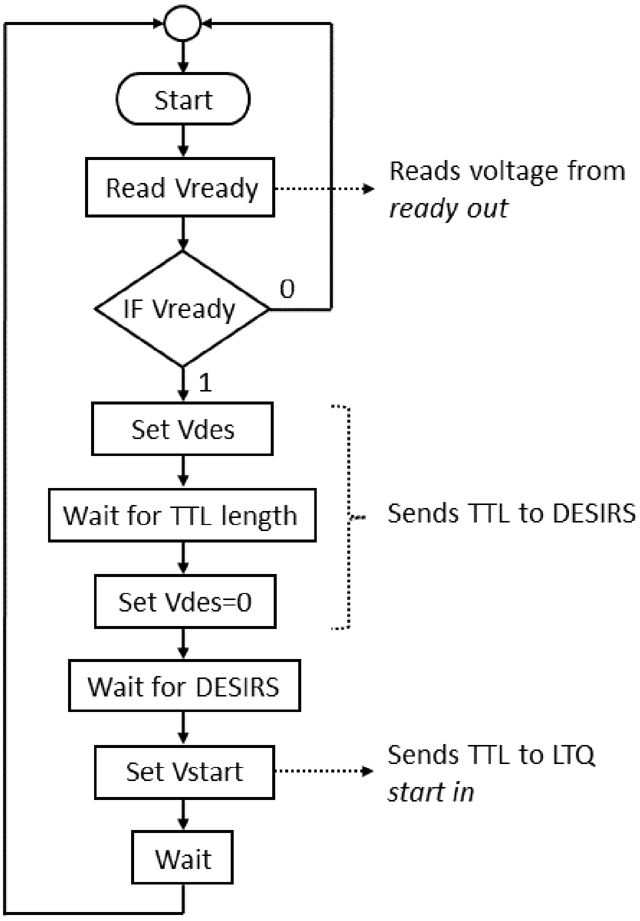

Figure 4.28 - Algorithm for Igor Pro program, used for energy scan process automation. Designed by A. Milosavljević and A. Giuliani.

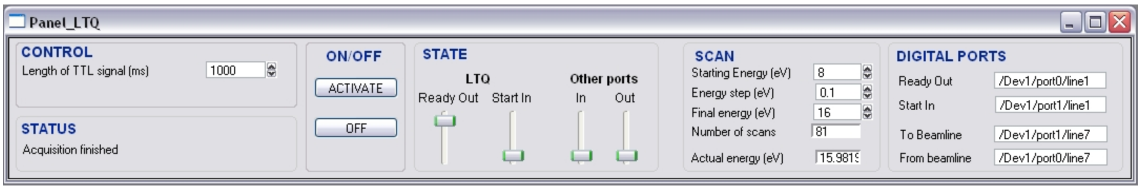

Panel_LTQ

CONTROL
Length of TTL signal (ms): 1000

STATUS
Acquisition finished

SCAN
Starting Energy (eV): 8
Energy step (eV): 0.1
Final energy (eV): 16
Number of scans: 81
Actual energy (eV): 15.981

DIGITAL PORTS
Ready Out: /Dev1/port0/line1
Start In: /Dev1/port1/line1
To Beamline: /Dev1/port1/line7
From beamline: /Dev1/port0/line7

Figure 4.29 - Custom made Igor Pro control window running on mass spectrometer's PC, used for energy scan process automation. Designed by A. Milosavljević and A. Giuliani.

On the other hand, the beamline PLEIADES is capable of changing the photon energy initiated by the external signal. Upon receiving a signal from LTQ, indicating that one energy point is finished, the beamline automatically prepares the necessary readjustments for the next photon energy. After the change to a new photon energy is done, the beamline sends the signal to its control output. The block diagram for the connection with PLEIADES beamline is depicted in Figure 4.30.

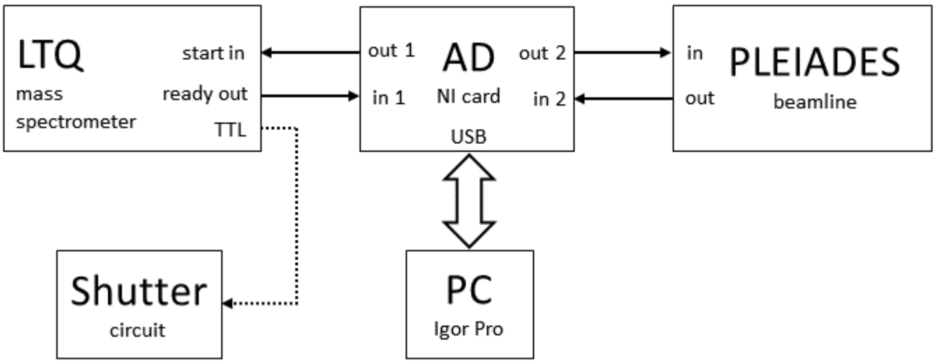

Figure 4.30 - Block diagram for connection of LTQ mass spectrometer with PLEIADES beamline.

4.5.4 Experimental procedure

This section is dedicated to the experimental procedure used in order to activate the trapped ions with photons from synchrotron radiation. As previously mentioned, the system is mobile and can be coupled to one of the three appropriate beamlines of the synchrotron SOLEIL. Figure 4.31 presents the part of the experimental setup involving the VUV photons from DESIRS beamline at the brunch B. The schematic representation of our experimental setup coupled the end station of brunch B at DESIRS beamline, is presented in Figure 4.32. The experimental procedure for coupling and synchronizing the system with the PLEIADES beamline is similar in principle, thus it is not presented in the Thesis. The timeline of the experiment is presented in Figure 4.33.

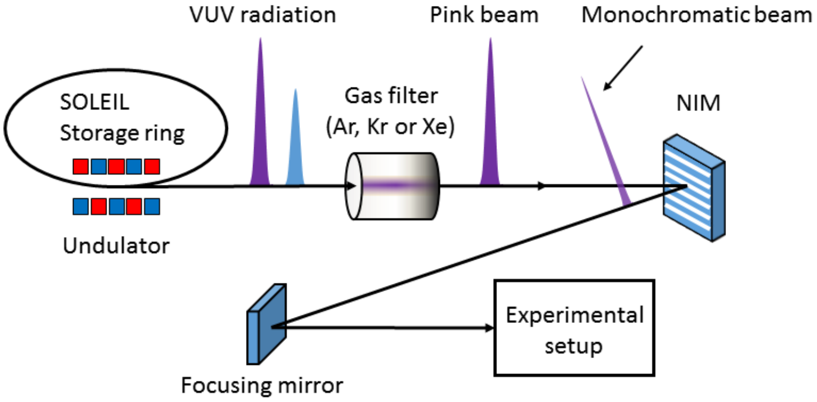

Figure 4.31 - Schematic representation of the VUV photon path in brunch B at the DESIRS beamline, starting from an undulator to the point where the experimental setup is coupled. Adapted with permission from [9].

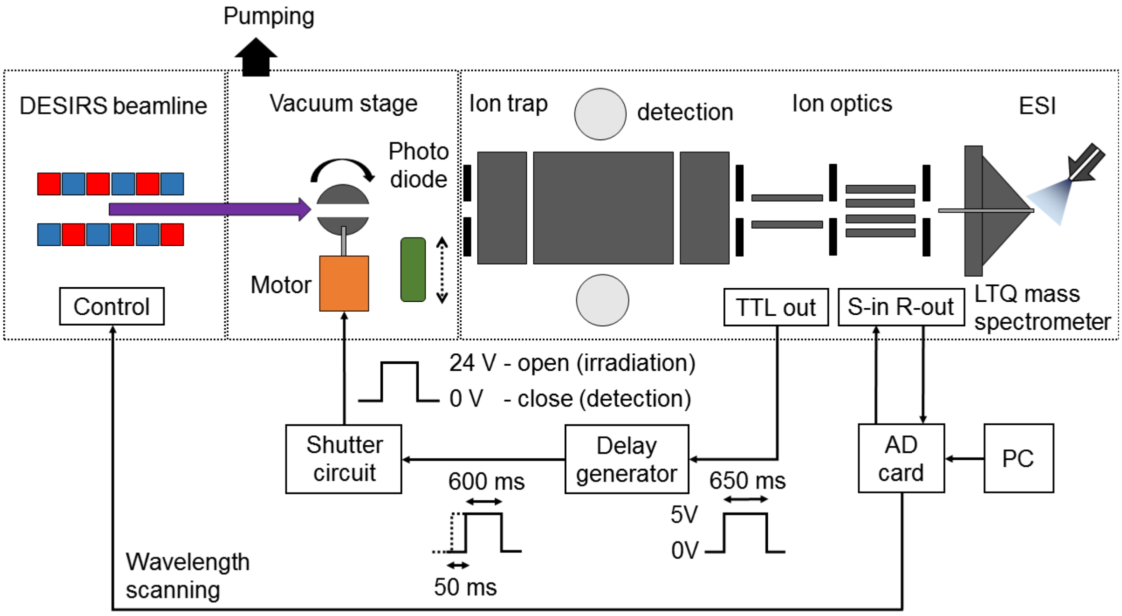

Figure 4.32 - Experimental method and schematic for synchronization of the LTQ mass spectrometer with the DESIRS beamline.

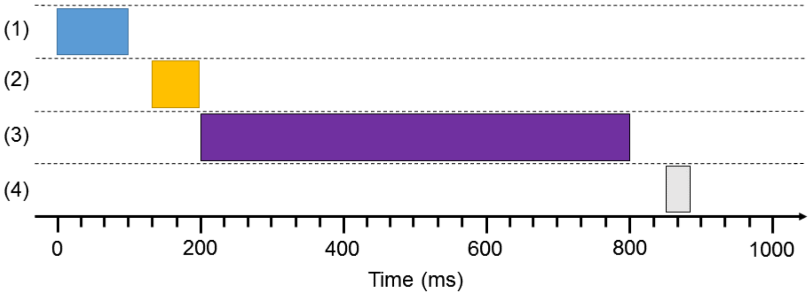

Figure 4.33 - Timeline of the experiment for the activation of trapped ions with VUV photons from DESIRS beamline: 1) ion injection, 2) ion selection, 3) ion irradiation and 4) fragment ion detection.

The experimental procedure is performed through four sequences: 1) ion production, 2) ion selection, 3) ion activation and 4) detection. More details are given below:

(1) Analyte solution was injected into a syringe and forced with the assistance of the mechanical pump through small capillaries into the ESI at the desired flow rate. Depending on a desired state of the target molecules, LTQ mass spectrometer can be equipped with two types of the ESI sources - standard ESI or nano-ESI. In this Thesis both hydrated and bare peptide precursor ions were probed with VUV photons. The production of hydrated precursor ions is more difficult and requires adjustments of the spray parameters. In both cases, all electrosprayed ions are guided by the ion optics and stored into the ion trap.

(2) A vast number of different charge state precursors can be produced simultaneously by a standard ESI (or nano-ESI) source. Only one precursor of the interest is selected, by defining the mass-to-charge ratio in the LTQ mass spectrometer software. The selected precursor was isolated in the ion trap by ejecting all other ions.

(3) After reaching the storing capacity of the ion trap, a 5 V TTL pulse is initiated by the LTQ electronics. The presence of the 5 V TTL signal on the shutter circuit closes the relay contacts and applies a 24 V on the electric motor inside the vacuum stage. The shutter head is rotated, allowing the VUV photon beam to irradiate the trapped ions. TTL 5 V signal is present during the activation time, defined previously (for example to 650 ms) in the LTQ software. In addition, a delay generator was installed on the path of the TTL signal, in order to introduce an acquisition delay (of usually 50 ms). As a result, the trapped ions are irradiated during a shorter time. After the activation time passes, LTQ sets TTL signal to the low state (0 V), the motor power is cut and the spring quickly rotates back the shutter head closing the photon beam.

(4) The detection takes place as soon as the TTL signal goes back to the low state (0 V). All ion fragments are ejected from the ion trap and an action tandem mass spectrum is recorded at the given photon energy and for the currently trapped precursor ion.

The LTQ software gives the possibility to program the selection method, containing a procedure with multiple precursors, with user defined duration for each precursor. In that case, each precursor is successively isolated in the ion trap during a specified time, ranging from (1-30) minutes. Steps (3) and (4) are then repeated for one photon energy until all precursors contained in the selection method are irradiated.

Each time the selection method is completed, or after the irradiation of all defined precursors at one photon energy, the LTQ initiates a long contact closure at *ready out*. This signal is detected by the program in Igor Pro and the TTL signal is sent to the DESIRS beamline in order to change the photon energy. The entire process is repeated until all predefined energy points are scanned. At the end of the energy scan, an action MS^2 for every precursor of the analyte macromolecule is acquired, at each photon energy defined in that particular energy scan.

4.6 Electron experimental setup

4.6.1 Electron gun

Double focusing electron gun was used as a source of electrons, for the purpose of activating trapped ions. It was developed at the Institute of Physics in Belgrade by S. Madžunkov and it is a constituent part of the experimental setup UGRA [58]. It is capable of producing relatively high primary electron current in the order of few μA in the electron energy range of (40-350) eV. A cross section view of the electron gun is depicted in Figure 4.34.

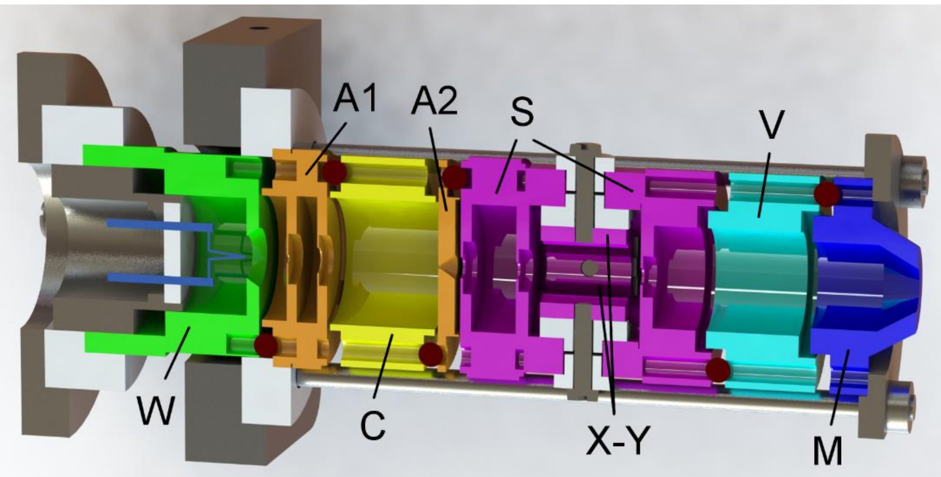

Figure 4.34 - 3D model of the electron gun, electrode cross section view.

The electron gun consists of seven concentric cylindrical electrodes. The electrodes are separated using the rubidium balls of 3 mm in diameter. The last electrode (M) is grounded, as well as the interaction region. The electrons are produced in the thermo-electron emission from the tip of the hairpin cathode, directly heated with currents of 2 A to 2.5 A. The cathode is made of thoriated tungsten wire 0.2 mm in diameter and spot welded to suitable pins cast in a ceramic disc. The electrodes of the electron gun can be divided into two parts: 1) the extraction and the focusing part. The extraction part of the electron gun comprises a hairpin cathode, electrodes W (Wehnelt), A1 (Anode) and C, whereas the focusing part is composed of electrodes A2, S, V and M. Two axis deflector unit have been installed inside the electrode S in order to enable the fine adjustment of the electron beam in the plane normal to the axis of the electron gun. In order to produce electrons with a defined energy, the cathode is supplied with a negative voltage in relation to electrode M, which is grounded along with the rest of the vacuum chamber. All other electrode voltages are floating on the negative cathode potential, such that focusing properties of the electron gun can be preserved with the change of the electron energy (cathode voltage). Since the electrodes W and C have a negative voltage applied in relation to the cathode, while A is positive, the extraction part of the gun formed from these three electrodes, has double focusing properties. First focusing of the electron beam happens by the lens formed with electrodes W and electrode A1. Second focusing happens between electrodes C and A2, which has a 0.5 mm diameter hole extending into a cone. After the extraction part, an image of the cathode with a defined circular shape is formed. The electrodes S, V and M, form a three-electrode lens with the purpose of defining the final geometry of the electron beam and focusing it on a given distance from the gun. Tuning the voltage on the electrode V is used to regulate the focusing properties of the electron beam for a given distance and electron energy. Present electron gun has been designed to generate a continuous electron current. This means that the cathode is constantly heated and that a steady stream of electrons with a defined energy and a beam geometry is produced continuously.[9]

4.6.2 Electron beam cut off principle and current measurements

For the purpose of activating trapped ions in the collisions with electrons, a continuous mode of the electron gun current cannot be used. Because of the temporal nature of tandem mass spectrometry experiments, the ion activation has to be engaged only during the short period of times - typically several hundreds of milliseconds. Therefore, in order to perform the action spectroscopy experiment with electrons as projectiles, a pulsed electron beam is required.

To cut off the photon UV (or X-ray) beam, a simple mechanical blocking was enough, as described in the previous chapters. For electrons this type of beam cut off is not desirable. The electrons are charged particles and can be easily splatted or reflected from conductive surfaces. On the other hand, they can charge nonconductive materials. As a consequence, the presence of an additional charging perturbs the optimal electric field generated by the electron optics. The final outcome is either a significant distortion or scattering of the electron beam.

In the present experiment, we chose to block the electron beam by means of preventing the emission of electrons from its source – the cathode. This can also be achieved by lowering the cathode temperature (for example, by decreasing the cathode current), but it is a very inefficient, unstable and slow process. An efficient electron beam cut-off can be achieved through a controlled change in the geometry of the electric field. For example, by applying the convenient pulsed voltage on one of the electron gun's electrodes. In the process of thermo-electron emission, a direct heating of the metal cathode increases the energy of the free electron gas inside it. At an appropriate cathode temperature, electrons have enough energy to escape the surface of the metal. The amount of this energy is defined by the metal work function, specific to every material. Therefore, by applying convenient voltages on the W electrode, placed just between the cathode and the anode, the metal work function of the cathode can be additionally altered in a controlled way -

---

[9] In the following text, this way of operation will be referred as a continuous mode of the electron gun.

to enable or prevent the electron emission from the tip of the hot hairpin cathode. The voltage applied to the W electrode required to fully suppress the electron emission was determined experimentally. It was done by measuring the electron current at a fixed distance from the electron gun, as a function of W electrode voltage.

Schematic for measuring the electron current in a Faraday cup is presented in Figure 4.35. The Faraday cup assembly is made from stainless steel. The electron collector is made from stainless steel bar, cut at 45° relative to its axis. It is installed in an isolated shielding tube, with 2 mm diameter hole at the front end. The entire Faraday cup assembly is positioned at a distance of 72 mm from the last electrode (M) of the electron gun. The electrode voltages are optimally adjusted to focus the electron beam on the Faraday cup, indicated by the maximal current readout, for a given cathode heating current and the electron energy.

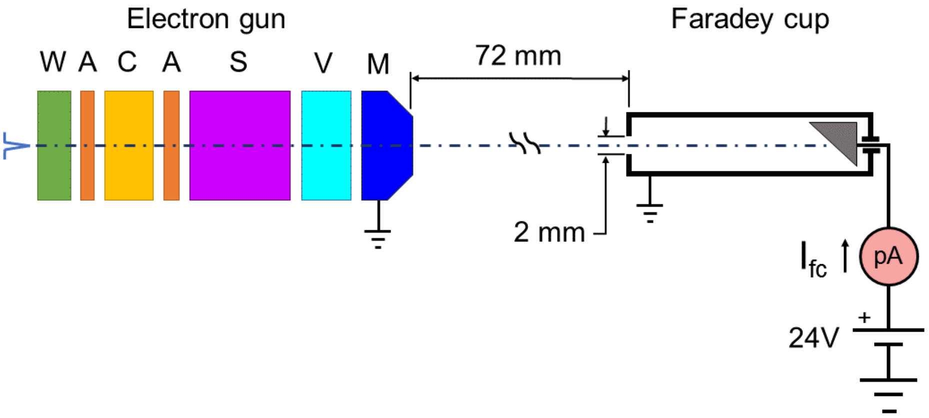

Figure 4.35 - Schematic diagram for electron current measurement using a Faraday cup.

Schematic for the electron emission current measurement is presented in Figure 4.36. An external power supply provides the relatively high current of 2.3 A for direct heating of the cathode. Another external supply provides a tunable negative voltage of up to 350 V which defines the electron energy since the interaction region is grounded. It is connected to the cathode through two equal high power resistors of 220 Ω, labeled with letter R in the Figure 4.36. This connection creates such voltage drop across the cathode, that potential on its tip is exactly -150 V. The cathode tip is a rather small surface and the energy distribution of all ejected electrons is dictated by the cathode tip temperature only. For this configuration, the influence of the geometry of the ejecting surface on the energy spread of ejected electrons is minimal. Thermo-electron emission process yields a typical energy bandwidth of 0.5 eV, for the tungsten hairpin cathode. Another important advantage of applying the voltage to the cathode through resistors, as depicted in Figure 4.36, is that the electron emission current from the cathode can be directly measured[10].

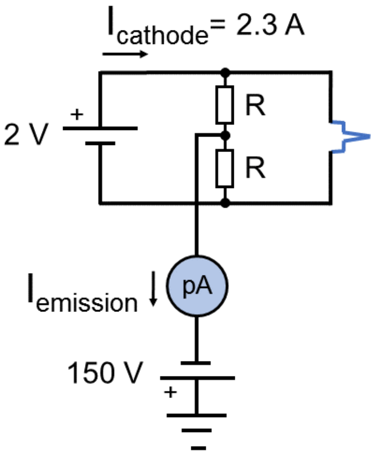

Figure 4.36 - Schematic diagram for electron emission current measurement.

Figure 4.37 presents the measured electron emission current from the cathode for different W voltages, as well as the Faraday cup current. For W voltages up to -20 V, we can see that both the emission current and the Faraday cup current are zero. Therefore for this given configuration of all other electrode voltages, both currents start increasing from about W=-20 V until they reach saturation at around W=-14 V.

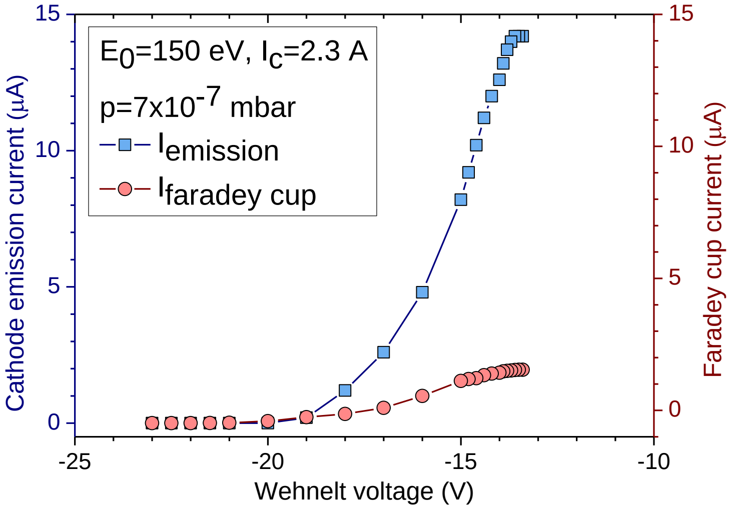

Figure 4.37 - Electron emission current from electron gun cathode and current measured in the faraday cup, as a function of W (Wehnelt) electrode voltage, for 2.3 A cathode current and 150 eV electron energy, for the pressure of 7×10^{-7} mbar.

---

[10] In this method of electron emission current measurement, only approximate value can be obtained. Measured current is linearly proportional to the real emission current, in the limited range only.

In order to make sure that there are no electrons emitted from the cathode, we used -50 V for the *beam cut off* W voltage. On the other hand, the working W voltage which enables a good focusing, called *beam on* voltage, is set to -14 V. It should be noted that only a small part from 15 µA current emitted from the cathode, actually exits the electron gun because the majority of electrons are lost inside the electron gun, as seen in Figure 4.37. For this particular electrode voltage preset current measured in the Faraday cup was around 2 µA.

Figure 4.38 compares the electric field distribution and the electron beam trace simulation from program SIMION [59] for different W voltages. The angular distribution of electrons emitted from the hairpin cathode is wide, thus a negative voltage has to be applied to the W electrode relative to the cathode potential, in order to narrow the beam. The influence of a negative W voltage can be seen by comparing Figure 4.38 (a) and (b). The electrons are scattered over the small aperture of electrode A if the W potential is kept at the cathode potential (W voltage of 0 V) Figure 4.38a. Optimal W voltage provides a good focusing and minimizes the loss of electrons that would otherwise scatter on the anode (Figure 4.38b). However, further lowering of the W voltage relative to the cathode to a critical value, creates a potential barrier which prevents the electron emission (Figure 4.38c). In this case, the metal work function of the cathode is effectively increased and the energy of the electrons is lower than the depth of the potential barrier, for the same temperature (the current) of the cathode.

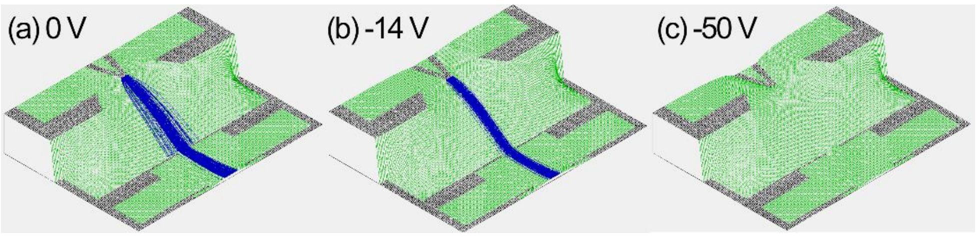

Figure 4.38 - Electric field and electron beam trace simulation from program SIMION. Voltages applied on Wehnelt electrode are relative to the cathode voltage: a) 0 V, b) -14 V and c) -50 V. High enough negative voltage completely blocks the electron emission.

4.6.3 Pulsing the electron gun

An electrical schematic of the electron gun with electronic shutter circuit[11] is presented in the Figure 4.39. The cathode and all electrodes are connected to the external power supplies. Each electrode has its own dedicated voltage divider constructed of variable resistors (helipots[12]) and a few fixed precision resistors. Two power supplies (one positive

---

[11] In the following text, term “shutter circuit” will be used to refer to the electronic shutter circuit, which supplies pulsed voltages on electrode W, in order to pulse the electron beam.

[12] Helipot is a multi-turn (up to 20 turns) variable resistor and is commonly used in electric circuits which require precise resistance adjustment along with high stability of voltages.

150 V and one negative -50 V) supply electrode voltages required for the operation of the electron gun. The electrode W is connected to its power supply through the shutter circuit. It was specially designed for the purpose of this experiment, in order to chop the electron beam. Details about the shutter circuit and its operation are given in the following paragraphs. In Figure 4.39, the shutter circuit is represented by a box, as the rest of the power supplies. The voltage input of the shutter circuit is the same negative power supply (of -50 V) as the one used for the electrode C. The output of the shutter circuit is triggered by the external TTL signal, generated by the LTQ mass spectrometer. The shutter circuit output has two states, depending on the state of the TTL signal. Each state is defined by one voltage, tuned to either enable or prevent the electron emission, thus allowing for the pulsed mode of operation.

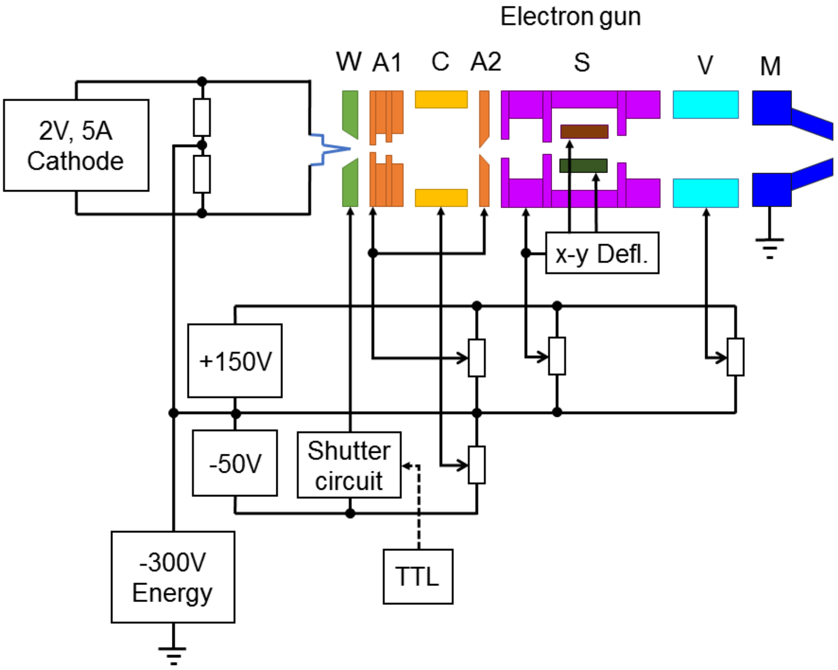

Figure 4.39 - Electron gun schematic with shutter circuit driven by TTL signal. All electrode voltages are floating on the potential of the cathode, which defines the electron energy.

4.6.4 Electron gun shutter circuit

A custom electric circuit was designed in order to supply two different voltages on the W electrode, triggered by the TTL signal sent from LTQ mass spectrometer. The circuit operates as a simple switch, connecting either the fixed -50 V to cut off the beam, or the tunable -14 V voltage, which allows optimal focusing of the electron beam. The basic principle of operation of the electron shutter circuit is presented in Figure 4.40.

In order to obtain fast and stabile voltage changes, we decided not to use mechanical relays. The reason is because of their multiple contact closures before the final contact closure, which would create noise in the highly stable voltages required for electron gun electrodes. On the other hand, the solid state relay used in the photon shutter circuit to drive the DC motor was the barely sufficient speed and stability for this purpose. Moreover, its power handling is well above nano-ampere currents that are typically required for electrodes of the electron gun. Also, it would require two of these relays to assemble the switch from the Figure 4.40. Instead, we designed a switching circuit that works on a similar principle as the solid state relay – using two optocouplers.

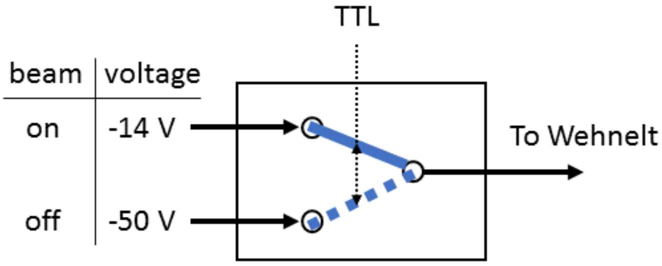

Figure 4.40 - The basic principle of operation of the electronic shutter circuit. In the upper position a switch connects -14 V to the W electrode, enabling the electron emission. Electron emission is completely blocked if the switch is in the lower position, where -50 V is applied to the W electrode.

An optocoupler is a passive electronic component, used to transfer the electric signal from one stage to another, using an infrared photodiode and a phototransistor. When the photodiode is turned on, infrared light opens the bipolar phototransistor. Because the resistance between the emitter and collector is very small when the transistor is open and vice versa, it is suitable for switching. If there is no infrared light, the transistor stays closed and the collector to emitter resistance is in the order of giga ohms. The basic principle of operation of an optocoupler is presented in Figure 4.41. The advantage is that the two optocoupler stages are galvanically isolated from each other and the reaction speed of the output phototransistor in relation to the input of the photodiode is in the order of microseconds. The shutting speed used for photons was in the order of 500 ms, but in the present case with electrons, the shutter circuit was designed to achieve the activation time of at least 1 ms.

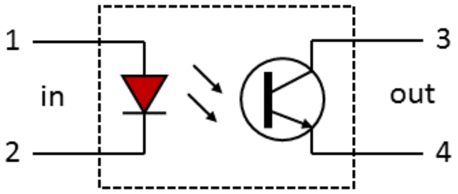

Figure 4.41 - Optocoupler – semiconductor electronic element. Infrared (IR) photodiode and an IR phototransistor are enclosed in a sealed package. Input terminals of the photodiode are (1) – anode, (2) – cathode, while output terminals of the phototransistor are (3) - collector and (4) – emitter.

Schematic of the shutter circuit for W electrode is presented in the Figure 4.42. A detailed description of the circuit follows. The circuit is designed in two stages, the driver (optocoupler) and the switching (transistor) stage. The function of the driver stage is to galvanically insulate the input - the LTQ mass spectrometer, from the high voltage output – required for the electron gun electrodes. Driven by the first stage, switching stage is composed of the voltage divider along with two transistors, which applies the high voltages to the W electrode.

The driver stage consists of two optocouplers O1, O2, the voltage supply for the optocouplers V1, the current limiter resistors R1, R2 for protection and two digital logic inverters enclosed in an SN7404 integrated chip. It should be noted that a signal generator (labeled TTL) in Figure 4.42 is not a part of the shutter circuit and is used for the simulation purpose only. The anodes of the photodiodes (their left sides in Figure 4.42) in both optocouplers are connected to the 5 V supply, through the resistors R1 and R2. The photodiode lights up only if there is enough voltage applied across its terminals[13]. In order for optocouplers to be in the conducting state, the cathode (right sides of the photodiodes in Figure 4.42) has to be polarized at 0 V (grounded). In order to design a switch which connects only one of the two input voltages to the output (W electrode), two optocouplers must always work in the opposite states – the first one on, the second one off and vice versa. The alternating operation is achieved with two digital inverters labeled N1 and N2 in the Figure 4.42. TTL signal from the LTQ mass spectrometer is simulated by the signal generator, setup to output a square wave pulse signal, with an amplitude of 5 V and 500 Hz frequency. This signal corresponds to the TTL output of the LTQ mass spectrometer for the activation time of 1 ms. The signal from the function generator is connected to the inverter N1, whose output is in series with the second inverter N2. The outputs of the first N1 and the second N2 inverters are connected to the cathodes of the photodiodes in the first O1 and second O2 optocoupler respectively. Since both anodes of the optocouplers are fixed at 5 V, this connection will ensure that the cathodes of the photodiodes are always connected to different voltages (0 V or 5 V). As a result, only one optocoupler can be in the conducting state while the other one is turned off. For example, if the input signal (from the signal generator) is at 5 V, the optocoupler O1 will be turned on, since its cathode will be at 0 V. Inverting the 5 V twice, after passing through both inverters, the cathode of the photodiode in the optocoupler O2 will, in that case, be at the same 5 V as its anode - meaning that it is turned off.

---

[13] For silicon PN junctions (diodes) this usually means at least 0.6 V, since it is the value of voltage drop generated across its terminals in the forward (conducting) direction.

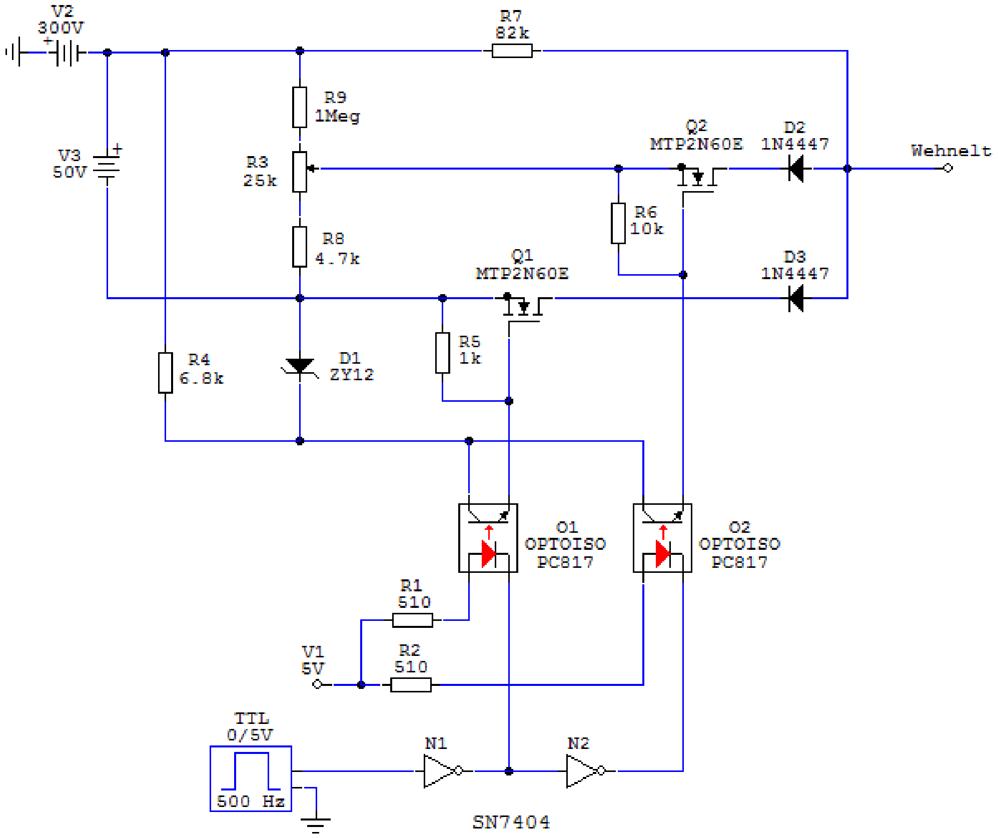

Figure 4.42 - Electric schematic for shutter circuit used to simulate and record the circuit response.

The driver stage of the shutter circuit has the function to drive the FETs (field effect transistors) that work as switches. An optocoupler driver stage alone cannot handle the high voltages floating voltages, therefore, the transistor switch stage had to be added. Both stages combined have a microsecond switching speed, determined by the slower driver stage, even though the transistor (FET) stage may work in the sub-microsecond regime. The collectors of the optocoupler output transistors are polarized to 12 V, through the Zener diode D1. This is not entirely true for the Q2 because it is floating on a variable part of the voltage divider created by R3 and R8 in addition to 12 V from the D1. For the transistor Q2, the resistor R6 value had to be increased enough so that it does not always stay closed. The increasing of the R6 has a downside of lowering the response time of the rising edge, which is clearly visible in Figure 4.44. The resistor R4 has the protection function, by limiting the maximal current passing through the bipolar output transistors of the optocouplers. The transistors Q1 and Q2 are N-channel enhancement mode field effect transistors and their gates are connected to the emitters of the optocoupler output transistors. The resistors R5 and R6 are connected in parallel with the drain and the gate of the FETs, to turn them off when optocouplers are in the off state. FETs have small capacitance between gate and drain, which can charge up and leave them open for a while. Resistors R5 and R6 are placed in order to dissipate this charge and close the FETs as soon as optocouplers are in the off state. Values of these resistors are critical for the performance of the circuit and they have been carefully chosen and tested to obtain the fastest reaction possible. When open, the transistor Q1 shorts its drain and source, thus -50 V from the external voltage supply V3 goes directly to the W electrode. If the transistor Q2 is open, then the adjustable voltage from voltage divider formed by helipot R3, resistors R8 and R9 is connected to the W electrode. In this case, only part of the negative voltage from V3 is taken, equal to -14 V, required for good focusing in the electron beam on state. The diodes D2 and D3 ensure that current flow is always in the appropriate direction, during the transition period between two states. Since all voltages are negative, the technical direction of the current flow is from W electrode to the voltage supplies V2 and V3. The resistor R7 has the function to polarize the drains of the FETs. The resistance of R7 also have a significant influence on the shutter circuit performance, thus its optimal value is experimentally determined.

The performance of the shutter circuit was evaluated in the PC program Circuit Maker, as well as by measuring the response on a digital oscilloscope. The results of the simulation are presented in Figure 4.43, while a real performance test is presented in Figure 4.44. Tests with the electron gun connected to the circuit showed minimal difference opposed to the unloaded circuit, although there is a visible difference between the simulation and the real circuit operation. The explanation of such difference lies in the simple resistive load used for the simulation, compared to a dynamic capacitive load of the operating electron gun in the real test. The rise time of the circuit was estimated from Figure 4.44 to around 100 μs, an input delay is in the order of 40 μs, while a fall time is ≈0.5 μs. A big difference between the rise and the fall time of the circuit is a consequence of discharging the parasitic capacitance of the FETs in the switching (FET) stage. Future developments of the circuit should be addressed at minimizing this delay by improving the circuit design with higher performance switching transistors, or even an optocoupler and a FET integrated into one package. Nonetheless, the results were more than enough for what was expected from the design and as required for the present experiment, given that optimal electron activation time was in the order of 500 ms. Figure 4.45 presents the home-made power supply box used in the electron experiments.

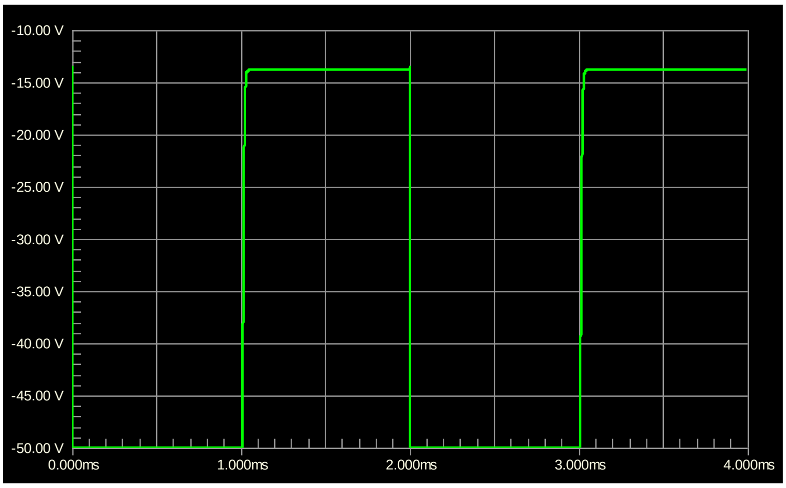

Figure 4.43 - Simulation of the shutter circuit in the program Circuit Maker, for 500 Hz square wave input signal, corresponding to 1 ms activation time.

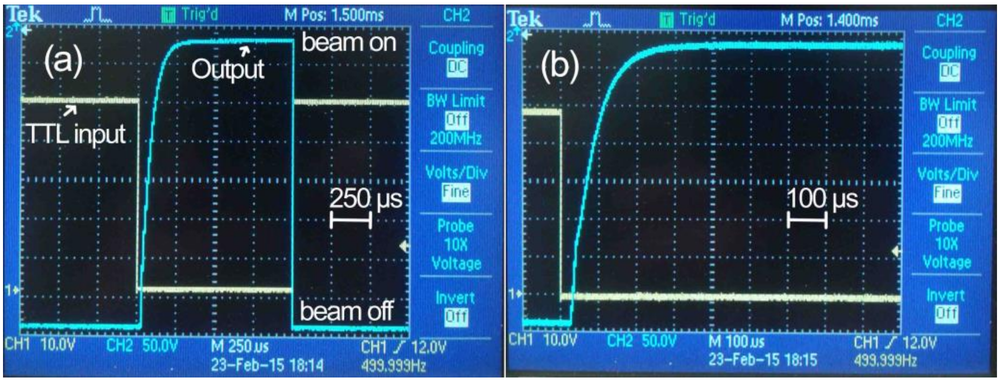

Figure 4.44 - Digital oscilloscope measurement of the shutter circuit response (Output) for 500 Hz square wave input signal (TTL input), corresponding to 1 ms activation time: (a) 250 μs per (horizontal) grid unit and (b) zoom in, at 100 μs per grid unit.

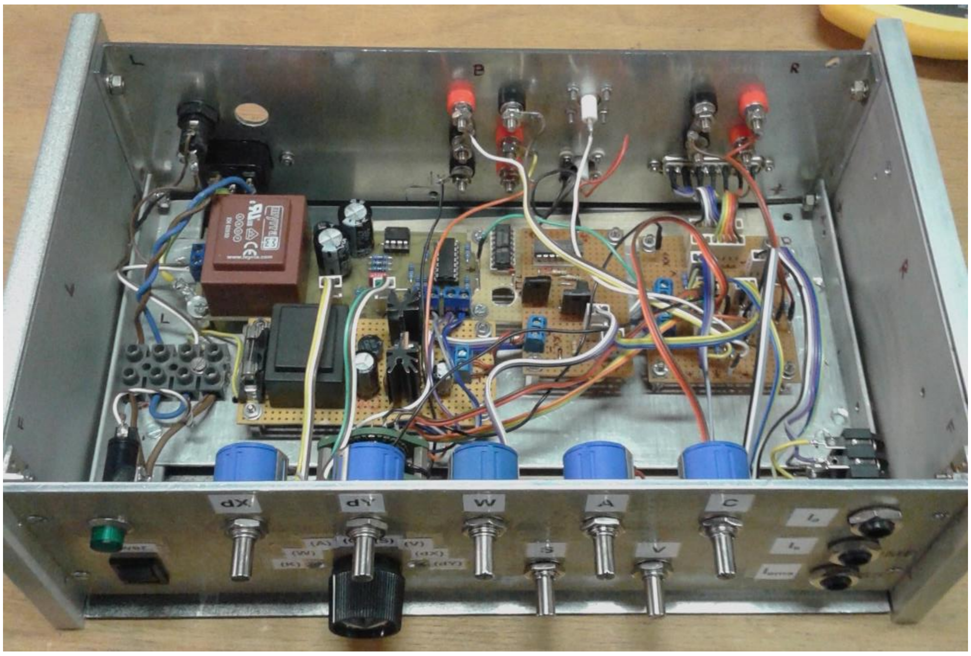

Figure 4.45 - Photograph of the electron gun power supply assembled for the present experiment. Electronic shutter circuit is integrated into the box. External high power supply for the cathode and high voltage supply which defines the electron energy are connected at the back side.

4.6.5 Coupling the electron gun with LTQ XL mass spectrometer

The differential turbo pumping vacuum stage was designed to couple the electron gun (described in Section 4.6.1) with the LTQ mass spectrometer. A 3D model of the vacuum stage with the electron gun is presented in Figure 4.46. It is based on a standard six-way CF100 cross, with a length of 220 mm. The electron gun is firmly fixed on an L-shaped Aluminum frame, mounted on a custom CF100 flange. The flange was modified to accommodate two CF16 electrical feedthrough flanges mounted on its back side, for the electron gun connections. A reducer flange CF100-40 and CF40 flexible bellows, provide the final coupling and allow for a precise alignment of the electron gun with respect to the ion trap axis.

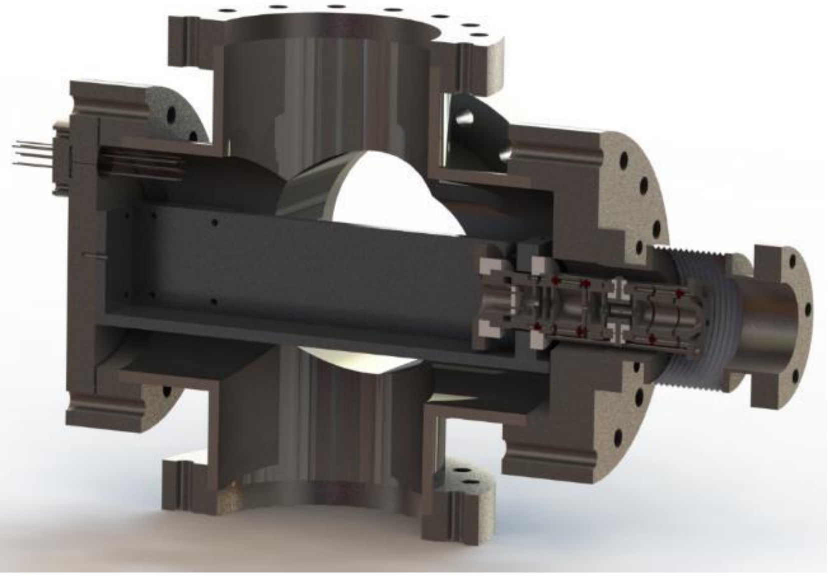

Figure 4.46 - Cross section view of 3D model of differential turbo pumping vacuum stage assembly with the electron gun, based on a six-way CF100 cross.

The remaining connections from the CF100 cross are used to fit a turbo pump, an ion pressure gauge and a glass window. The vacuum gauge is attached to the long flexible bellows and positioned approximately 1 m away from the vacuum assembly, in order to reduce the magnetic stray fields as much as possible. The present experimental setup is only equipped with the electrostatic shielding, while the magnetic shielding was not installed[14]. The vacuum stage design was focused on the alignment precision, as experience from the experiment with photons showed that it was important. Optimal alignment is crucial in order to obtain an efficient activation of trapped ions, which results in a high signal to noise ratio of the instrument. The practical realization of the vacuum assembly with the electron gun is presented in Figure 4.47.

The entire vacuum assembly is mounted on a rigid support frame and coupled to the back Plexiglass window of the LTQ mass spectrometer. Figure 4.48 presents the 3D model of the experimental setup. The initial rough alignment of the electron gun was done by moving the vacuum stage relative to a fixed position of the LTQ mass spectrometer. The verification of the rough alignment was done with the laser pointer directed through the ion trap from the front side (right side of the ion trap in Figure 4.48). The LTQ mass spectrometer is installed on an adjustable supporting frame [9], with translational and rotational degrees of freedom. The precise final alignment of the electron gun axis with

---

[14] Due to the space limitations and mechanical complexity, magnetic shielding with Mu-metal sheet foil was not possible to implement efficiently in the present flexible coupling design.

respect to the ion trap axis is achieved by fine tuning the position of the LTQ mass spectrometer frame, during ion activation measurements.

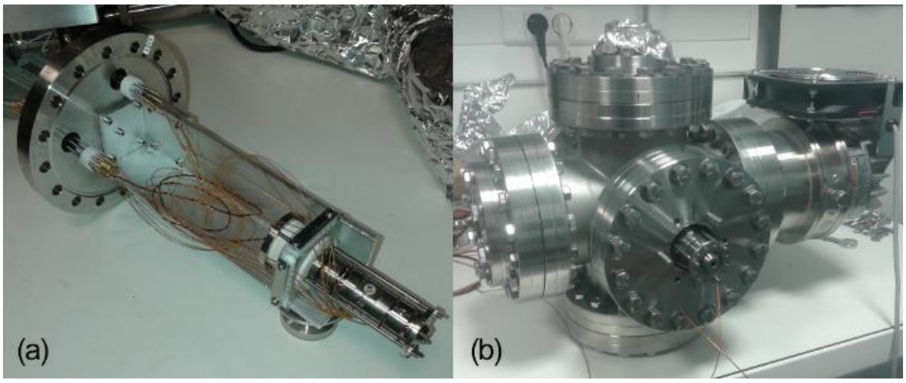

Figure 4.47 - Differential turbo pumping vacuum stage assembly with the electron gun: (a) electron gun is mounted on a CF100 flange via L-shaped frame and (b) CF100 cross, fitted with the electron gun, a turbo pump and a glass window (a pressure gauge is attached via a flexible extension to the upper flange - not shown here).

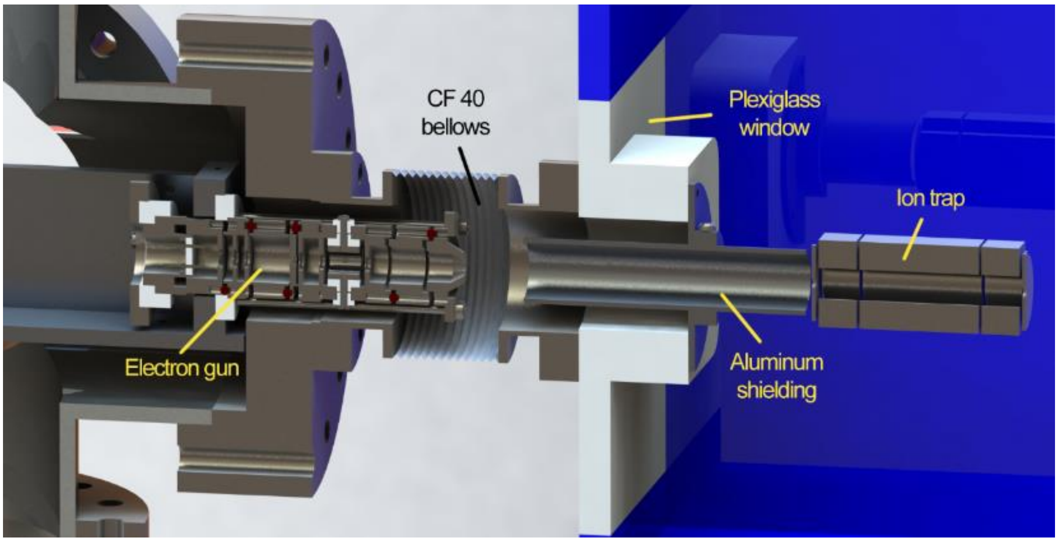

Figure 4.48 - 3D model of the coupling of the electron gun with LTQ XL mass spectrometer.

The electrostatic shielding of the electron gun is achieved with an Aluminum tube shield, installed along the axis between the electron gun and the ion trap. The Aluminum shield also prevents charging of Teflon insulated wires installed temporarily for the purpose of testing the electron gun, as well as all other insulated parts in the ion trap vacuum chamber inside the LTQ. Details of the electron gun test measurements are given in the Section 6.2.1.

4.6.6 Experimental procedure

In this section, a description of the experimental procedure for the activation of trapped ions in the collisions with electrons is presented. Figure 4.49 displays the schematic of the experiment. The main instrument of the experimental setup is the LTQ mass spectrometer, equipped with an ESI source on the front side. The vacuum stage with the electron gun is coupled to the back side, allowing a direct injection of electrons into to the ion trap.

The experiment is conducted in four steps: 1) ion production, 2) ion selection, 3) ion activation and 4) detection of fragments. The timeline of the experiment is presented in Figure 4.50.

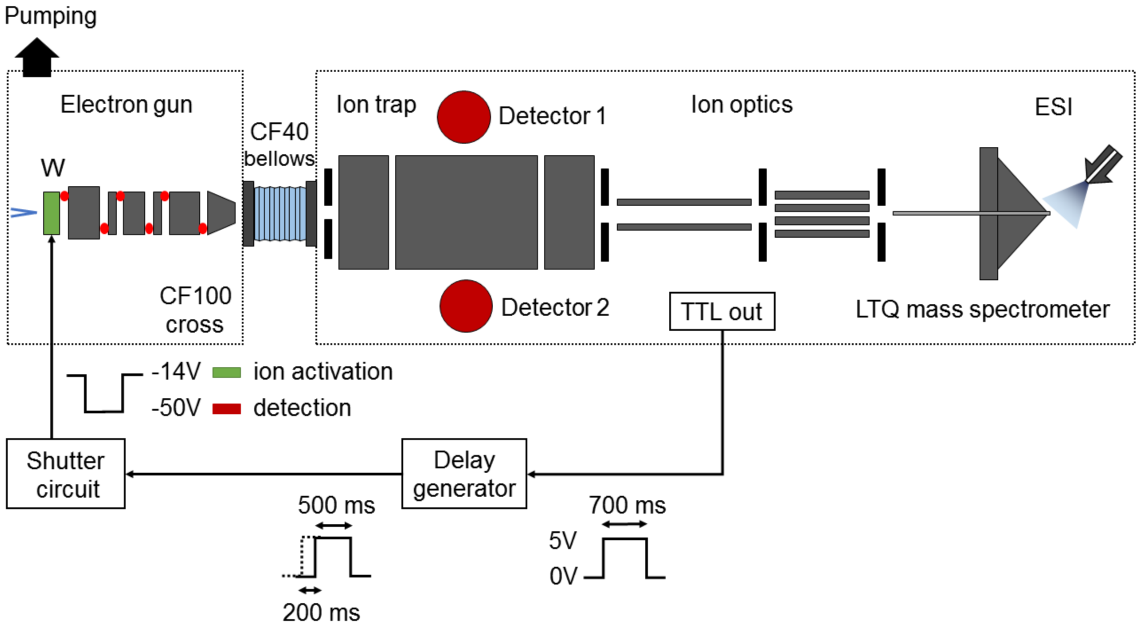

Figure 4.49 - Experimental method and schematic for synchronization of the LTQ mass spectrometer with the electron gun.

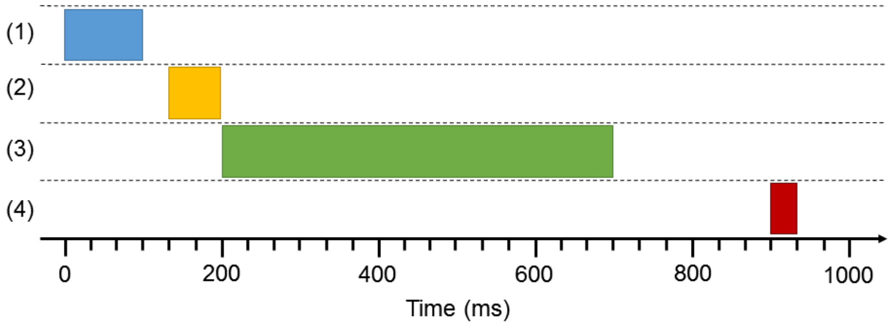

Figure 4.50 - Timeline of the experiment: 1) ion production, 2) ion selection, 3) activation and 4) detection.

(1) Solutions with biomolecular targets were prepared at desired concentration and injected into the ESI. By fine tuning of ESI parameters as well as solution properties, a wide range of precursor charge states of molecular ionic species can be produced. The generated ions pass through a long capillary that ensures pressure difference. The capillary is heated in order to remove excess water molecules. Guided by ion optics, comprised of octupole and quadrupole mass filters the electrosprayed ions are introduced into the ion trap from the front side (right side of the ion trap in Figure 4.49).

(2) Desired precursor ions, with user specified mass-to-charge ratios, are selected and isolated in the ion trap. In the LTQ, the efficiency of the trapping is further increased by the presence of the buffer gas. In order to stabilize the trajectories of ions selected in the trap, Helium buffer gas at the pressure of 10^{-3} mbar was used.

(3) Each time the number of trapped ions reach the storing capacity of the ion trap, a TTL pulse is triggered by the electronics of the LTQ mass spectrometer. In Figure 4.49, the output of this signal is symbolized with a “TTL out” box. The amplitude of the pulse is 5 V, while its duration is defined by the activation time, specified by the user. TTL signal is directed to the shutter circuit, which switches its output state to -14 V and enables the electron emission. Consequently, a focused electron beam of defined energy is formed, which activates the trapped ions. As soon as TTL signal goes back to low state (0 V), shutter circuit applies -50 V to W electrode, which in turn stops the electron beam.

A delay generator (DG645, Stanford 150 Research Systems, Sunnyvale, CA, USA) is inserted between the TTL out and the shutter circuit. Its function is to introduce an acquisition delay between the end of ion activation and the start of the fragment detection. In that case, the activation time as defined in LTQ software has to be increased by the amount of the desired acquisition delay. The delay generator is set to output a new TTL signal on the rising edge of the first one. As a result, a background noise can be fairly reduced.

(4) The low state of the TTL signal also initiates the start of the ion fragment detection. In the LTQ, a high-frequency pulse is applied to the ion trap ring electrodes, which ejects all ion fragments and action MS^2 is recorded. Optionally, several successively obtained action MS^2 for a single electron energy are averaged in order to increase statistics.

The entire process can be repeated for a number of different electron energies, in small energy steps (typically 0.2 eV), obtaining many MS^2 as a function of the electron energy.

5 Ion optic basics and simulations

In the electron optics, the electric fields can be generated by applying electric potentials on specially designed electrodes. The electric potentials are applied to two adjacent electrodes, in order to form the electrostatic lenses. Depending on an application, the electrodes are created in a wide range of shapes. The electrodes with planar, cylindrical or spherical symmetry are the most common. The cylindrical electrodes are typically used to generate two-dimensional radial electric fields. Other shapes can also be manufactured, if the requirements for the electric field geometry are more complex, for example, for a three-dimensional ion trap. The electron lenses work by creating the electric field gradient that changes the trace of the charged particles. The charged particles can be accelerated, decelerated, or collimated in a focused ion beam. In the present work, the commercial program for simulation of ion optics SIMION [59] was used.

5.1 SIMION

First step in the simulation is to define a desired electron optics geometry and its electric potentials via a special programming code by creating a geometry file. The potentials on each electrode are defined by the user. In a process called *"refining"*, the program then solves the Laplace equation for the electric potential and calculates the electric field defined by the gradient of that potential using a method of finite differences. This process gives the solution for the electric field in an empty space between electrodes. After obtaining the electric field, desired charged particle initial conditions can be set and the program solves differential equations of motion. In the final step, the program displays particle trajectories. Additionally, a special LUA programming code can be used for recording the particle statistics and the definition of time-dependent potentials on the electrodes.

5.2 Ion trap modeling

The linear quadrupole ion trap from LTQ mass spectrometer was modeled in order to investigate the influences of RF electric fields on the transmission of electrons. A total length of the ion trap is 68 mm and it is composed of three axial sections. In order to save the computer resources, each section (see Figure 5.1b) is modeled separately. The front (1) and the back (3) sections are created in 3D, without the use of symmetry. The center section (2) is defined by extending a two-dimensional profile in the axial direction. All sections are composed of four hyperbolic electrodes with a minimal radius of 4 mm (see Figure 5.1a). Two disk-shaped electrodes (the front and the back plate) with 2 mm apertures are also modeled in order to accurately simulate the ion trap. Figure 5.1c presents the isometric view of the modeled ion trap.

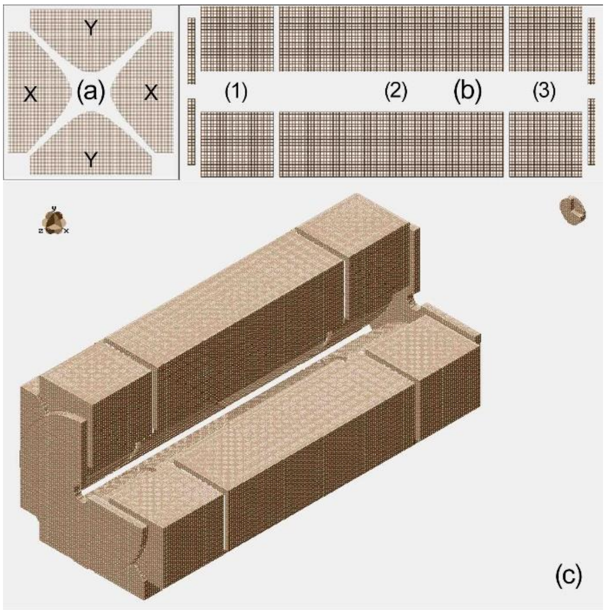

Figure 5.1 - 3D model of the ion trap from LTQ mass spectrometer from SIMION.

Regarding the applied potentials, the ion trap electrodes are arranged in two pairs, one located on the vertical (Y pair) and the other located on the horizontal axis (X pair), as depicted in Figure 5.1a. Amplitude of the RF potential is A=400 V, with the frequency of 1 MHz (ω/2π), while the amplitude of DC potential is B=100 V. The polarity of the applied potentials on the each pair of electrodes is given by the following relation:

$$\begin{aligned} &Y: A\sin\omega t + B \\ &X: A\sin(\omega+\pi)t - B \end{aligned} \tag{5.1}$$

Above described configuration of the applied potentials enables only radial trapping of the charged particles, meaning that they can move freely in the axial direction and eventually exit the ion trap. In order to restrict the motion of the charged particles in the axial direction as well, DC potentials in the center section are lowered by 10 V, in relation to the DC potentials applied to the front and back section. It should be noted that the amplitudes of the RF and DC voltages in the actual ion trap depend on the m/z ratio of the selected ions. The amplitudes used in the simulation are the maximal values of these voltages, which are selected in order to estimate the highest perturbation of the electron beam. The main program (LUA code) through which the RF and DC fields are applied as well as the definitions of the electrode geometries (GEM files) are given in Appendix 8.2.

5.3 Pulsed electron beam transmission

The influence of the RF and DC electric fields on the electron beam in the simulation are quantified by measuring the geometrical properties of the electron beam at the center of the ion trap (at 34 mm in the axial position). More specifically, for each electron crossing the plane perpendicular to the trap axis at the axial position of 34 mm, three variables were measured: x-coordinate, y-coordinate and the energy.

The initial electron beam has a radius of 0.5 mm with a uniform spatial distribution of a total of 1.21×10^5 electrons per pulse, with initial velocities parallel to the ion trap axis. All electrons have the same initial energy of 300 eV. The electrons are generated with a Gaussian time distribution, where a standard deviation defines the electron beam pulse width. In relation to the phase of the RF field, the center of the Gaussian distribution for each pulse width was always set to an optimal value, for which the highest transmission is obtained. Since the full period of the RF field is 1 μs, any pulse width above this value can practically be considered as the continuous beam.

The space charge effects were not included in this part of the simulation. The electron-He collision cross section decreases significantly above the energies of about 60 eV, as reported by J. Nickel et al [60]. Nevertheless, we investigated the influence of the He buffer gas to the propagation of 300 eV electron beam in the ion trap.

We present the simulation results obtained after including the interaction between the electrons and the He atoms. The inclusion of the He buffer gas was done using the collision model (HS1) within the SIMION8.1 example programs, made by D. Manura [61]. The temperature of the He buffer gas was set to 300 K, at the pressure of 5.3×10^{-3} mbar, whereas the total cross section for electron-He scattering was $\sigma = 5.56 \times 10^{-21}$ m^2 [60].

The obtained results were recorded for three electron beam pulse widths of: (i) 1μs, (ii) 100 ns and (iii) 10 ns, as well as the case (iv) 1μs where the He buffer gas was included. Table 5.1 presents the recorded electron beam properties at the center of the trap.

Table 5.1 - Electron transmission results in the ion trap. Tob is the time of the electron birth with respect to the phase of the RF field phase, while T_{end} is the transmission recorded at the end of the ion trap.

Pulse width [ns]	**Tob [ns]**	**T_{end} [%]**
1000	0.5	65
1000 (He buffer)	0.5	62
100	0.6	80
10	0.65(5)	100

The electron beam propagation through the ion trap at three different pulse widths is presented in Figure 5.3. The electron beam spatial and energy distributions recorded at the center of the ion trap are presented in Figure 5.3.

The case (i) with a pulse width of 1 μs practically represents the continuous electron beam. We can see that the electrons are highly scattered just at the entrance of the ion trap. However, a significant number of electrons of about 65% are able to pass through the entire length of the ion trap. The electron energy distribution presented in the right side of Figure 5.3(i) show that majority of electrons at the center of the ion trap still have the same initial energy of about 300 eV, although there is a visible broadening of the energy distribution of about ±2 eV. The spatial distribution of the electrons presented in the left side of Figure 5.3(i) show that majority of electrons are still within the initial radius of 0.5 mm, whereas the rest is scattered on the electrodes.

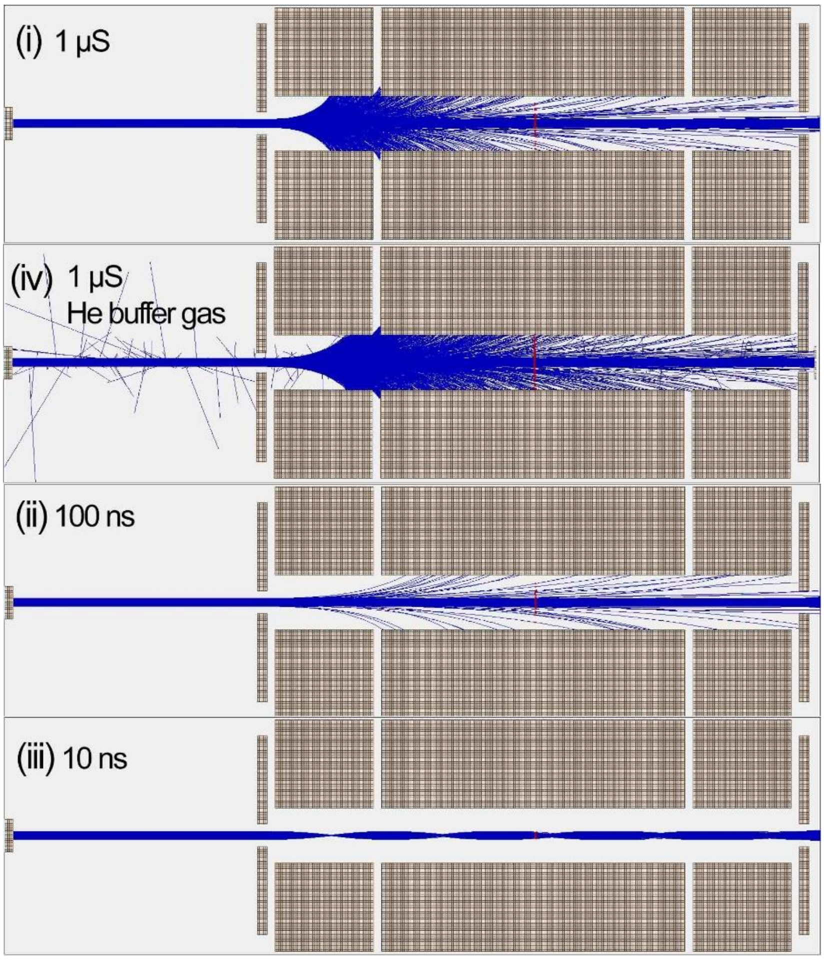

Figure 5.2 - Electron beam transmission in the ion trap: (i) 1 μs, (ii) 100 ns (iii) 10 ns and (iv) 1 μs with included He buffer gas at the pressure of 5x10^{-3} mbar and temperature 300 K. The total electron-He cross section used for simulation was σ=5.56x10^{-21} [60].

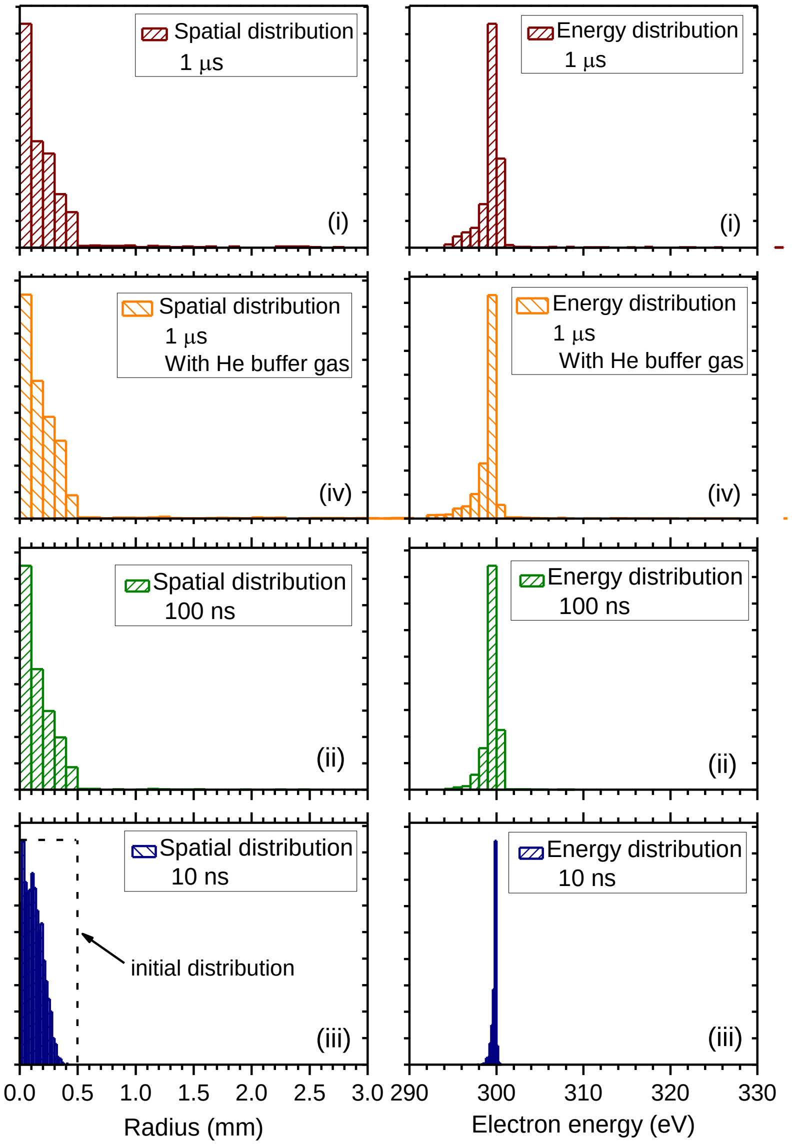

Figure 5.3 - Simulation of 300 eV pulsed electron beam in a linear quadrupole ion trap**,** for 400 V RF and 100 V DC, for three different pulse widths of: (i) 1 μs, (ii) 100 ns (iii) 10 ns and (iv) 1 μs with included He buffer gas at the pressure of 5x10^{-3} mbar and temperature 300 K. The total electron-He cross section used for simulation was σ=5.56x10^{-21} [60].

Decreasing the electron beam pulse widths to (ii) 100 ns and (iii) 10 ns leads to a significant transmission increase [see Figure 5.3(ii), (iii) and Table 5.1]. The electron transmission is increased to 80% and even up to 100% (for 10 ns). The influence of the RF electric fields on the spatial and energy distributions is almost negligible. The broadening of the electron energy distribution is about ±0.5 eV. In comparison with the real experiment, this broadening is practically in the order of initial energy distribution of the electrons produced in the thermo-electron emission from the heated cathode. However, it should be noted that for a very narrow pulse widths (10 ns) the synchronization with the RF fields is crucial. According to the simulation, deviation of about ±25 ns from the optimal synchronization point with respect to the RF field phase can cause a total suppression of the electron beam (a transmission of 0 %).

The electron beam transmission results obtained for the included He buffer gas at 1 μs pulse width (continuous beam) can be seen in Figure 5.2(iv) and Figure 5.3(iv). Spatial and energy distributions, as well as the transmission recorded at the end of the ion trap are very similar with the obtained simulation results without the He buffer gas. Although, we can see that a very small percentage of the electrons is randomly scattered. This is clearly visible in Figure 5.2(iv) in the region just in front of the ion trap, however, the scattering is also present in the space between the electrodes inside the ion trap. Qualitatively, we can say that 300 eV electron beam is not affected significantly by the presence of the buffer gas. The transmission at the end of the ion trap is slightly reduced - from 65 % to about 62 % due to the additional scattering on the He atoms.

Present simulation findings clearly show the benefits of the lower pulse widths, although in the case of a pulse width of 1 μs (continuous beam), satisfactory results were also obtained, even with the He buffer gas. It should be noted that in the present experimental setup for electron activation of trapped ions (Section 4.6), due to the limitations imposed by the response of the shutter circuit, the absolute minimum of the obtainable pulse width is around 250 μs (see Figure 4.44). This is still over 100 times more of what is required in order to effectively achieve the pulsed electron beam, with respect to the ion trap RF period. Therefore, according to the simulation, we were not able to experimentally obtain the optimal electron transmission through the ion trap, since we practically used the continuous electron beam. The obtained experimental results for the electron-impact dissociation of biopolymers are presented in Section 6.2.

6 Results and discussion

6.1 Photon experiments

6.1.1 VUV photo-dissociation of peptides and hydrated nucleotides

Leucine-Enkephalin (Leu-enk) monomer

Peptides are polymeric chains composed of amino acids. They are very important for living organisms since they play an important roles in performing biological functions [62]. Their function is linked with their primary structure - amino acid sequence [63]. Any modifications or degradations of the primary structure of biopolymers by energetic photons (UV, VUV or X-rays) could potentially lead to a cellular death. These processes are called radiation damage. The investigation of the photo-induced processes in peptides, mainly with UV and VUV light are important for the understanding of both the radiation damage at the molecular level and the electronic structure of these species. With developments of synchrotron radiation sources, the action spectroscopy of building blocks of biomolecules has become a powerful experimental method capable of giving more insights into fundamental physicochemical properties of these species. This could hopefully help understanding the biological functions of large macromolecules that they form.

In this section, our results of VUV action spectroscopy of protonated Leucine-Enkephalin (Leu-enk) peptide [64] are presented. Figure 6.1 shows a schematic structure of the Leu-enk peptide, with the nomenclature of the most prominent ionic fragments. Leu-enk is a small peptide, consisted of five amino acids with the sequence: YGGFL (tyrosine-glycine-glycine-phenylalanine-leucine).

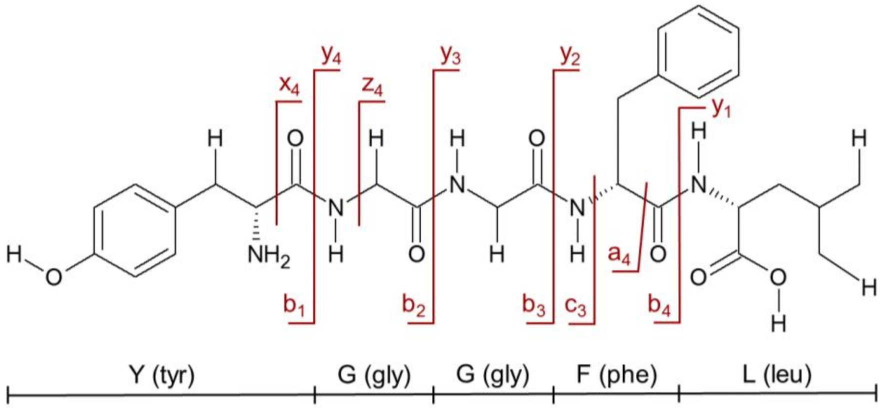

Figure 6.1 - The structure of the Leucine-Enkephaline peptide with its five amino acid constituents and imonium ions with mass-to-charge ratios of Y(136), F(120) and L(86).

Leu-Enk has been frequently investigated in the past using a vast number of mass spectrometry techniques. For example, by collision induced dissociation (CID) [65, 66], surface induced dissociation [67] (SID), black body infrared dissociation (BIRD) [68] and laser induced dissociation (LID) [69]. The experimental conditions and activation methods favor certain dissociation pathways dictated by particular fragmentation mechanisms. The fragmentation scheme of the protonated Leu-Enk was investigated by V. Rakov et al [66] in the experiment involving multiple resonance CID. The protonation site is usually located at Nitrogen in the tyrosine amino acid, although other protonation sites are reported due to the ion mobility ([70] and references therein). Recently, S. Bari et al [44] reported the VUV photo-induced dissociation of the protonated Leu-Enk by coupling SR photons with a 3D ion trap, where the ionization energy (IE) was estimated with DFT calculations to 8.87 eV. Their findings suggest that below IE the absorption of photons primarily lead to the cleavage of the peptide bonds, while above IE they could find a new dissociation pathways leading to a fast loss of a tyrosine side chain.

In the present work, protonated Leu-Enk cations $[M+H]^+$ (m/z 556) were isolated in the ion trap and subjected to VUV photons, with the energies in the range from 5.5 eV to 14 eV, with a small energy step of 0.2 eV. Figure 6.2 presents the obtained action MS^2 after photon impact at a few selected energies, below and above the IE.

The absorption of VUV photons leads to electronic excitation of the precursor ions, followed by the dissociation (below IE) or dissociative ionization (above IE), resulting in the formation of different fragment ions. In the case of backbone fragments (cleavage of C_α-C or C-N bonds), depending on where the remaining charge (proton) stays upon bond scission, a standard nomenclature was proposed by K. Biemann [71]. If the charge stays at N-terminal fragments a_n, b_n and c_n, are formed. The fragments x_n, y_n and z_n are formed if the charge stays at C-terminal. The number in the subscript indicates the remaining amino acid residues in the particular fragment ion. The absorption of photons can also lead to detachment of neutral groups (for example amino acid residues) or scission of several bonds.

Below the IE, in the action MS^2 obtained for 6.7 eV (Figure 6.2a), the most prominent fragments correspond to the cleavage of the peptide backbone. Namely, ion fragments b and y originate from scission of C-N bond, while the cleavage of C_α-C bond results in the formation of ion fragments a. The backbone fragments are designated at mass-to-charge ratios b_4 (m/z 425), a_4 (m/z 397), b_3 (m/z 278) and y_2 (m/z 279). This fragmentation pattern is in a good agreement with the CID experiments [65], where backbone fragments are also dominant. Moreover, we could observe peaks corresponding to precursor loss of water molecule $[M+H]^+$-H_2O (m/z 538), the tyrosine side chain [M+H]+-107 (m/z 449) as well as loss of phenylalanine side chain $[M+H]^+$-91 (m/z 465). Even though the fragments b_3 and y_2 have close m/z values, mass resolution in the present experiment was sufficient to resolve these peaks (see inset in Figure 6.2a). An internal fragmentation of the ion a_4 leads to the formation of fragments a4-NH_3 (m/z 380) and another loss of glycine a4-NH_3-57 (m/z 323). With a loss of the tyrosine side chain, fragment b_4 forms into b_4-107 (m/z 318). Less abundant peaks correspond to internal fragments GGF (m/z

262) and GF (m/z 205), while neutral (carbon monoxide) loss from this fragment is the origin of ion assigned to GF-CO (m/z 177).

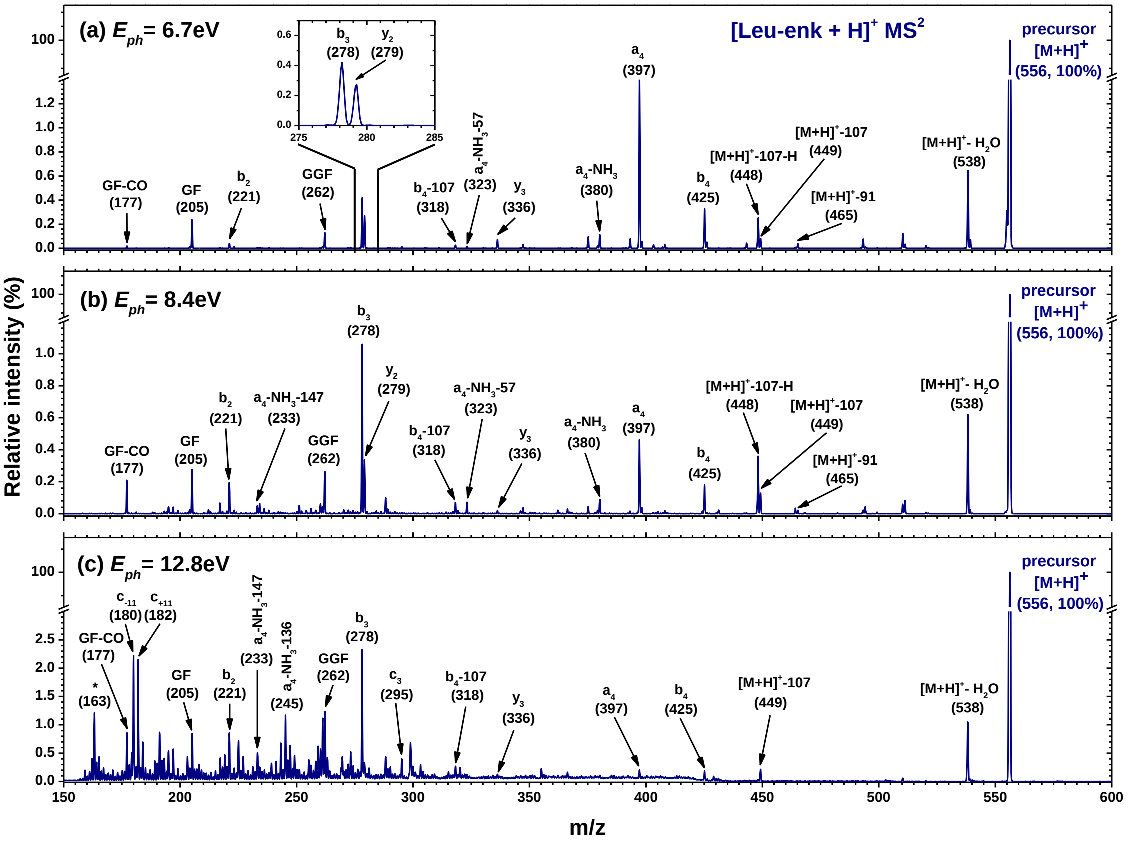

Figure 6.2 - Photo-activation tandem mass spectra of leucine-enkephalin, after 500 ms irradiation of [Leu-Enk+H]$^+$ precursor at: (a) 6.7 eV, (b) 8.4 eV and (c) 12.8 eV photon energies. The proposed assignments of the most important fragments are given in the figure while "M" denotes the pseudomolecular ion.

As the photon energy increases towards the IE, in the MS^2 obtained at 8.4 eV (Figure 6.2b), we can observe quantitative changes the fragmentation pattern. More specifically, fragment b_3 (m/z 278) becomes the most prominent, followed by b_2 (221) and GF-CO (m/z 177), whereas the ions a_4 (m/z 397) and b_4 (m/z 425) are fairly decreased.

Similar fragmentation patterns below the IE as in the CID experiments [65] suggests that the absorption of photon proceeds with the electronic excitations of protonated Leu-Enk precursor ions, followed by a fast internal conversion and/or intramolecular vibrational energy redistribution (IVR) to the vibrationally hot electronic ground state. The relaxation from these vibrationally excited states results in the dissociation of the Leu-enk precursor ions dominantly through backbone cleavage.

Above the IE, in MS^2 recorded for 12.8 eV (Figure 6.2c) we observe a rich fragmentation pattern in the low m/z region of 150-350. This is due to the opening of more relaxation channels which become available above IE. It should be noted that the photoionization of the residual contaminants in the ion trap is the origin of many unassigned fragments. The peak at m/z 538 corresponding to water loss is increased by two-fold, as well as the ion fragment b_3 (m/z 278). Mass-to-charge ratio of doubly ionized precursor ion $[M+H]^{2+}$ is also 278, but the question remains if these ions indeed contribute to the mentioned peak. Indeed, the doubly ionized precursor ion is probably unstable and thus, its contribution to the peak at m/z 278 is very low, although further studies are required for a definite answer.

Due to a high photon energy resolution, a high mass resolution, as well as a high signal to noise ratio, the present experimental setup gives the possibility to record the spectroscopic features and investigate the electronic structure of the protonated Leu-enk cations. The ion yields for several backbone and internal fragments are extracted from MS^2, by integrating the area under the particular peaks and plotting it against the photon energy. The ion yields were normalized to both the photon flux and the total ion current, in order to compensate for their changes throughout the energy scan.

Figure 6.3 presents the ion yields in the photon energy range of (5.7-13.8) eV, obtained for Leu-enk fragments corresponding to the backbone dissociation. The ion yields are characterized by a rich spectroscopic structure.

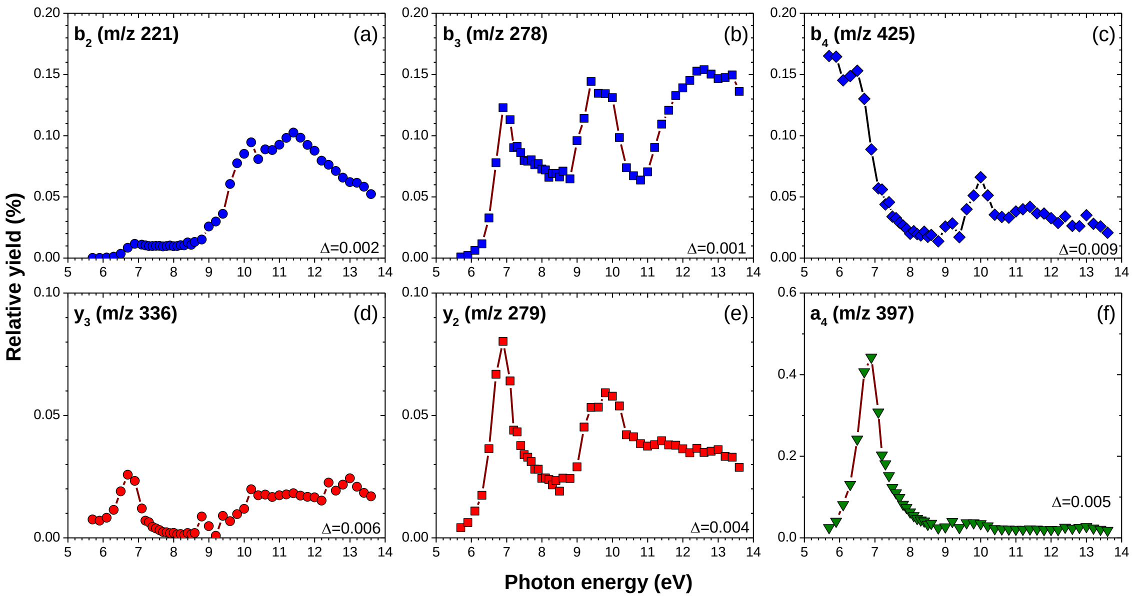

Figure 6.3 - Normalized relative ion yields from the photodissociation of precursor $[\text{Leu-Enk+H}]^+$ in the range from 5.7 to 14 eV. Integrated mass ranges are: (a) b_2 (m/z = 220.5-221.5), (b) b_3 (m/z = 277.5-278.5), (c) b_4 (m/z = 424.5-425.5), (d) y_3 (m/z = 335.5-336.5), (e) y_2 (m/z = 278.5-279.5) and (f) a_4 (m/z = 396.5-397.5). The absolute uncertainties of the experimental points are shown on the right bottom corner of each panel as Δ values.

According to the previous studies [15], [72–75], the electronic structure of the peptide bond in small peptides (di- and tripeptides) can be approximated by a four energy level system: two occupied π orbitals (π_1 and π_2), the oxygen lone pair n_o and the virtual π_3^*

orbital. Orbitals π_1, π_2 and π_3^* originate from the peptide bond and are bonding, non-bonding and anti-bonding respectively. A comprehensive fragmentation study of Substance P peptide with VUV photons was reported by F. Canon et al [15]. Figure 6.4 presents a schematic representation of the electronic structure of Substance P peptide [15].

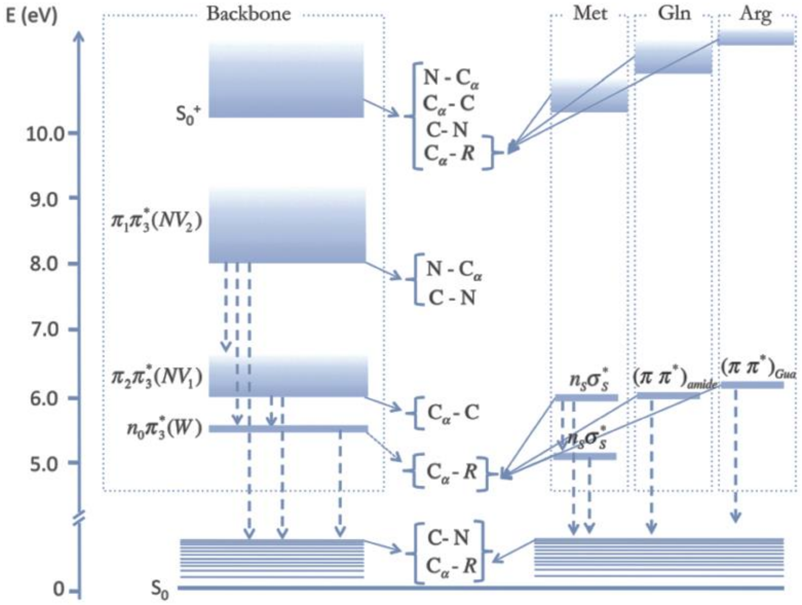

Figure 6.4 - Energy diagram for Substance P peptide. Adopted from [15].

The ion yields presented in Figure 6.3 (a) to (e), correspond to the fragments b_2, b_3, b_4, y_3 and y_2 respectively, which originate from the cleavage of the peptide C-N bond (peptide backbone fragments). All ion yields obtained for peptide backbone fragments show a distinctive spectroscopic band centered at about 6.9 eV. This spectroscopic band is associated with $\pi_2\pi_3^*$ (NV_1) transition, followed by a fast non-radiative deexcitation to the vibrationally hot electronic ground state. Most probably, C-N bond cleavage could then proceed from this hot ground state. A distinctive spectroscopic band centered at around 7 eV in the ion yield for fragment a_4 (Figure 6.3e) can be associated with the same transition, but with different fragmentation channel corresponding to the scission of C_α-C bond. The ion yields for fragments b_3 and y_2 show the second band centered at about 9.6 eV, which can be associated with transition $\pi_1\pi_3^*$ (NV_2). The scission C-N peptide bond can, in this case, proceed directly from the excited state π_3^* [15].

The photo-dissociation yields for b ions (N-terminal fragments), presented in the first row of Figure 6.3, originate from the scission of the same C-N bond, but at different locations along the peptide chain. Therefore by comparing their ion yields we can investigate the differences in the VUV absorption efficiency along the peptide chain. Going from ion b_2 towards b_4 (i.e. approaching to the C-terminus) the fragment mass increases. According to the present results, the low energy part of the photo-dissociation yields becomes more important. Particularly for ion b_4 (Figure 6.3c), we can see that with lowering of the photon energy, the ion yield increases, suggesting that the formation of b_4 ion can also be associated with $n_0\pi_3^*$ (*W*) transition, previously estimated at about 5.5 eV [15].

Since both b and y ion fragments are formed by the cleavage of the same C-N bond, ion pairs b_2/y_3 and b_3/y_2 should have similar photo-dissociation yields. This can be seen in Figure 6.3 by comparing the ion yields from the first and the second column. These pairs of fragments indeed have similar absorption efficiencies, although the lower energy part of the yield for y ions is actually more pronounced. The ion yield of the fragment b_3 shows a strong increase above 11 eV, whereas the ion yield of the fragment y_2 slowly decreases. It was already noted that b_3 ion has the same m/z 278 as the doubly ionized precursor ion $[M+H]^{2+}$, which should strongly increase above the IE. On the other hand, the doubly charged precursor is very unstable and might decay before the detection. Furthermore, the ion yield of b_2 and b_3 (N-terminal) fragments is higher in the whole photon energy range relative to the ion yields of y_3 and y_2 (C-terminal) fragments. This is in a good agreement with the finding that the preferential protonation site for the gas phase Leu-enk is at the N-terminus [76].

The both b_4 and a_4 ions shown in the last column of Figure 6.3, are formed by the cleavage of the neighboring bonds C-N and C_α-C, respectively, with the charge left at N-terminus. Therefore, we can compare their photo-dissociation yields. In the low energy region both ion yields show distinctive spectroscopic band, suggesting that they are dominantly formed in dissociation process involved with the $\pi_2\pi_3^*$ (*NV_1*) transition.

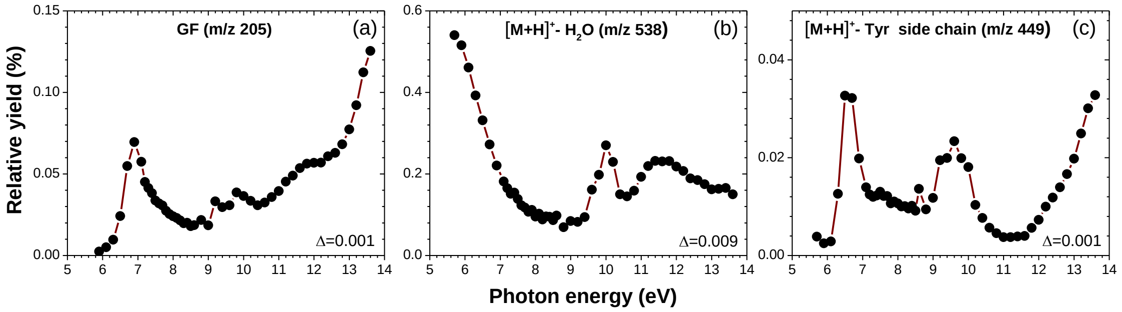

Figure 6.5 - Normalized relative ion yields from the photodissociation of precursor $[\text{Leu-Enk+H}]^+$ in the range from 5.9 to 14 eV. Integrated mass ranges are: (a) GF (m/z = 203.5-204.5), (b) $[M+H]^+$-H_2O (m/z = 537.5-538.5) and (c) $[M+H]^+$-tyrosine side chain (m/z = 448.5-449.5).

Figure 6.5 presents the photodissociation yields for fragments originating from cleavage of multiple bonds (GF m/z 205), as well as by a neutral loss (water and tyrosine side chain) from precursor ions. The fragment GF is formed mainly from y_3 and a_4 according to [67], suggesting that its photo-dissociation yield should be similar to yields of these fragments. It is indeed similar, although only in the lower energy region with the spectral band centered at around 7 eV (associated with transition *NV_1*). Unlike for fragments y_3 and a_4, which show a few spectroscopic features but mainly remain flat with the increase of energy, ion yield of the fragment GF shows a strong increase as the photon energy passes the IE. The peak at m/z 538, corresponding to the water loss shows a similar increase of the photo-dissociation yield as the fragment b_4 with the lowering of the photon energy, suggesting that its formation may also proceed from $n_0\pi_3^*$ (*W*) transition. Formed by the cleavage of the C-N bond, the C-terminal fragment b_4 is in close proximity to the carboxyl group. Therefore, based on the similarity in their photo-dissociation yields, it is possible that water molecule extraction site is also close to the carboxyl group [64]. In CID [65] and SID [67] experiments with protonated Leu-Enk, the peak corresponding to water loss was also observed as the strong relaxation channel. On the other hand fragment at m/z 449 corresponding to tyrosine side chain loss, show the spectroscopic bands centered at 6.9 eV and 9.8 eV. These two bands are in a good agreement with the observed spectroscopic bands obtained for the backbone fragments, associated with electronic transitions NV_1 and NV_2 respectively. The photo-dissociation yield of the fragment at m/z 449 is similar to the obtained ion yields for b and y fragments, suggesting that its origin might also be from the peptide backbone cleavage.

Leucine-Enkephalin (Leu-enk) dimer

Leu-enk dimmer is composed of two non-covalently bound monomer units of the Leu-enk peptide. In the present experiment, dimer precursor ions are produced by ESI from the same solution used to obtain Leu-enk monomer precursor ions. In this section, our results from the action spectroscopy of protonated Leucine-Enkephalin (Leu-enk) peptide dimer below the IE [77] are presented.

The same consideration for fragment nomenclature given in the previous section also applies here (for a reference see Figure 6.1). Singly charged precursor ions $[2\text{Leu-Enk} + \text{H}]^+$ are selected in the ion trap and subjected to VUV photons in the range of (5.7-8) eV with 0.2 eV steps. Figure 6.6 presents the action MS^2 obtained for 6.7 eV photon energy.

Besides the precursor ions $[2\text{M+H}]^+$ designated at m/z 1111, we can clearly see that the most prominent dissociation channel corresponds to the cleavage of the weak non-covalent bond between monomers, resulting in the formation of the protonated monomer unit $[\text{M+H}]^+$ at m/z 556. If we take a closer look in the m/z regions below the monomer precursor Figure 6.6b, as well as in the region between the dimer and monomer precursors Figure 6.6c, we can observe a rich fragmentation pattern.

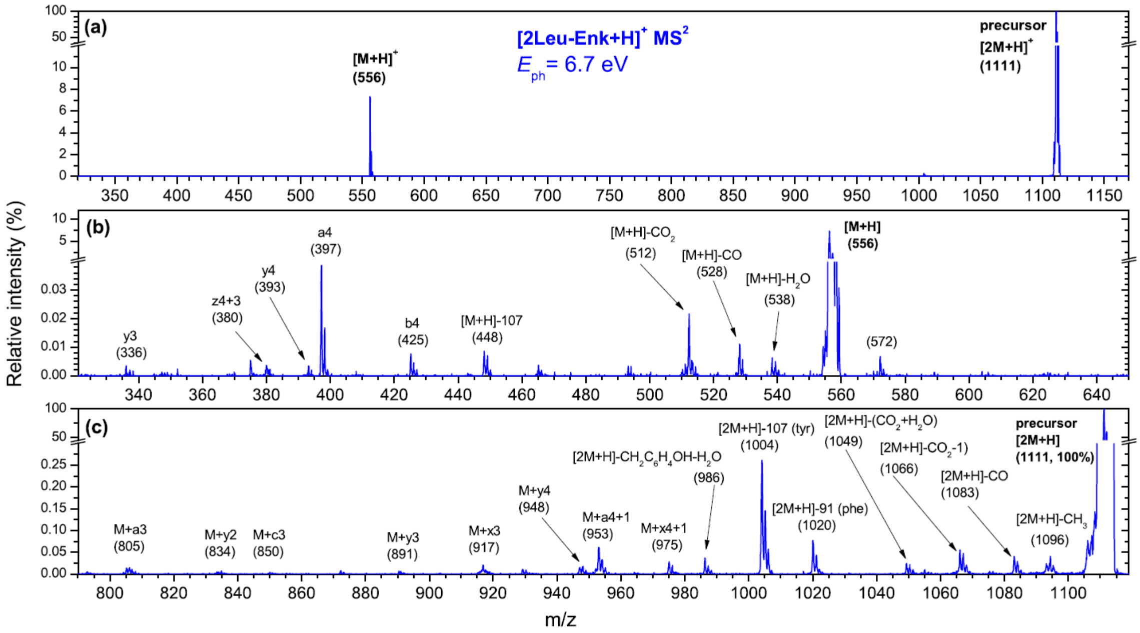

Figure 6.6 - Photo-activation tandem mass spectrum of leucine-enkephalin (Leu-Enk) peptide dimer recorded after irradiation of [2Leu-Enk+H]$^+$ precursors at 6.7 eV photon energy. The lower panels (b), (c) show close up of the mass regions up to (m/z 650) (b) and down to (m/z 800) (c), respectively. The proposed assignments of the fragments are given in the figure, where notation "M" corresponds to monomer unit "Leu-Enk".

The action MS^2 from Figure 6.6b show strong peaks corresponding to the backbone fragments a_4 (m/z 397), b_4 (m/z 425), y_4 (m/z 278) and y_3 (m/z 279). Their relative intensity distribution is in a good agreement with the action MS^2 obtained for the monomer molecule at the same energy (Figure 6.2a). It should be noted that m/z resolution of the action MS^2 for dimer molecule presented in Figure 6.6 is lower than in the case of MS^2 for monomer molecule presented in Figure 6.2a, due to requirements of extended mass range imposed by the dimer precursor mass. A broad peak at m/z 380 is probably associated with the formation of C-terminal peptide backbone ion z_4. Strong relaxation channels correspond to neutral losses from dimer precursor ions. Namely, water, carbon monoxide and carbon dioxide neutral losses are assigned to peaks at m/z 538, 528 and 512 respectively. Designated at m/z 448 we also observe the peak corresponding to the tyrosine side chain loss.

The photo-dissociation of dimer precursor below the IE leads to the formation of backbone fragments that are still bound to the monomer molecule (Figure 6.6c). More specifically, the fragmentation channels corresponding to the cleavage of the peptide backbone are assigned to peaks [M+a_3] (m/z 805), [M+y_2] (m/z 834), [M+c_3] (m/z 850), [M+y_3] (m/z 891), [M+x_3] (m/z 917), [M+y_4] (m/z 948) , [M+a_4+1] (m/z 953) and , [M+x_4] (m/z 975). We can also observe many other peaks associated with the extensive neutral losses from the dimer precursor ion. Particularly the most dominant peaks correspond to the tyrosine side chain loss [2M+H]$^+$-107 (m/z 1004) and phenylalanine side chain loss [2M+H]$^+$-91 (m/z 1020).

Like in the previous section, the investigation of the energy dependencies (photo-dissociation yields) of the selected fragment ions enables to reveal the electronic structure of the weakly bound dimer molecule, as well as its photostability towards VUV radiation. VUV photo-dissociation yields of the fragments originating from protonated Leu-enk dimmer precursor ion are presented in Figure 6.7 and Figure 6.8.

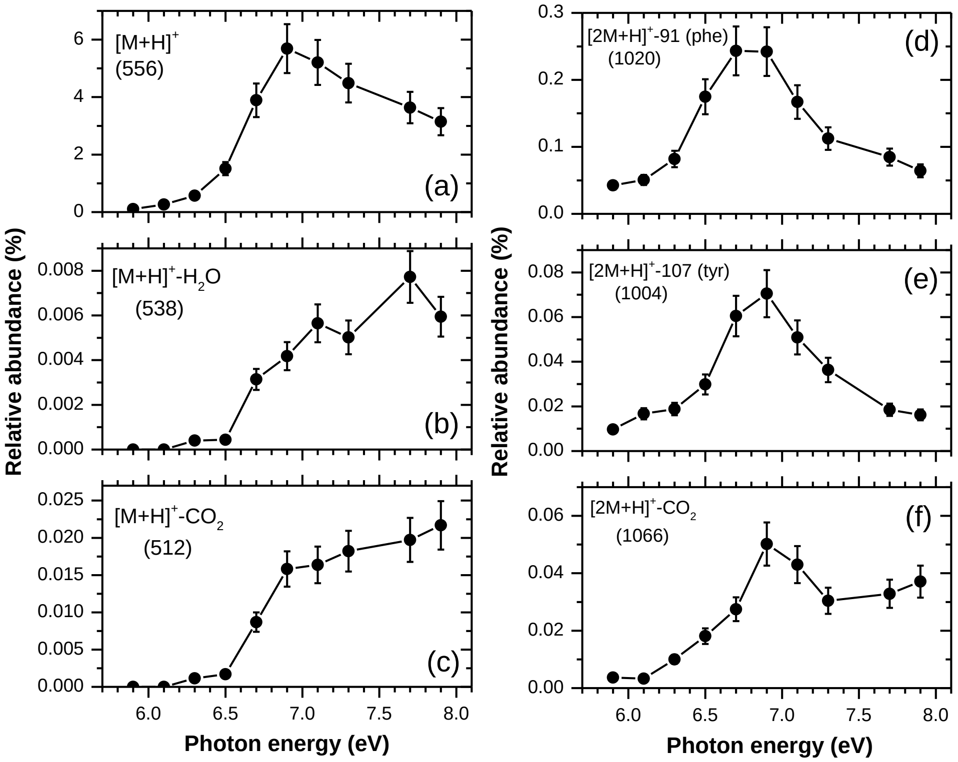

Figure 6.7 - Photo-dissociation yields of: (a) $[M+H]^+$ (m/z 556.1–556.4), (b) $[M+H]^+$-H_2O (m/z 538.08–538.38), (c) $[M+H]^+$-CO_2 (m/z 512.1–512.4), (d) $[2M+H]^+$-91 (phenyl) (m/z 1020.0–1020.3), (e) $[2M+H]^+$-107 (tyrosine) (m/z 1003.98–1004.28) and (f) $[2M+H]^+$-CO_2 (m/z 1066.0–1066.3) fragments.

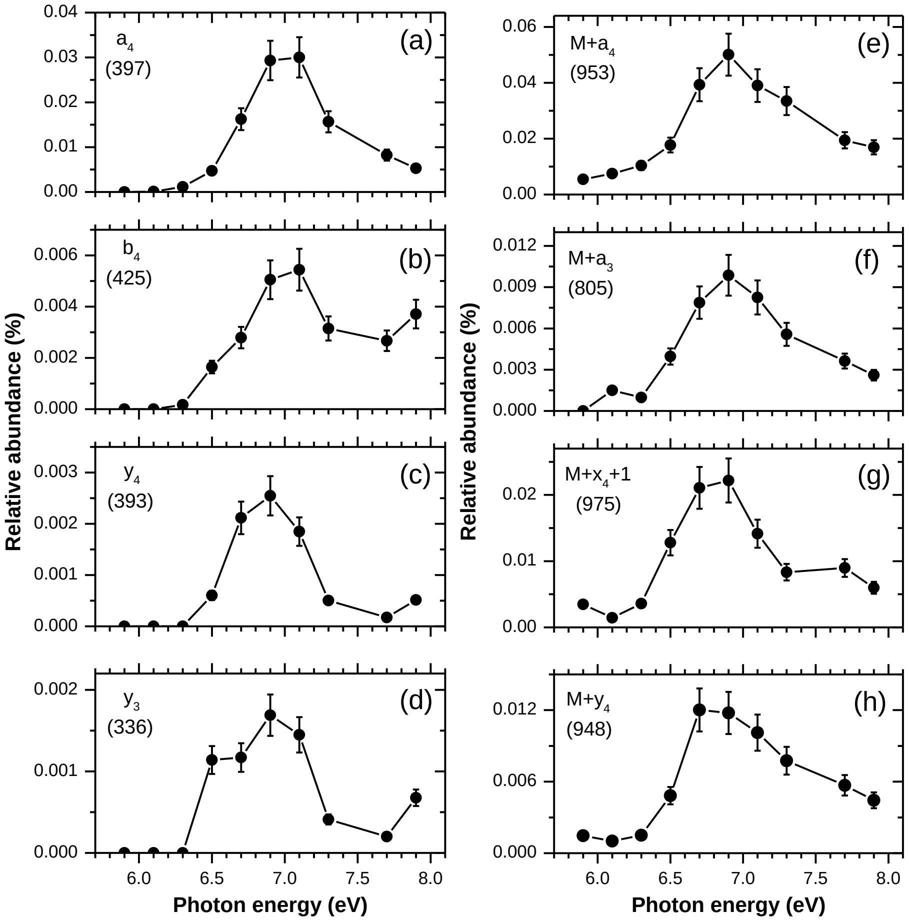

Figure 6.8 - Photo-dissociation yields of: (a) a_4 (m/z 397.05–397.35), (b) b_4 (m/z 425.08–425.38), (c) y_4 (m/z 393.0–393.3), (d) y_3 (m/z 336.0–336.3), (e) M+a_4 (m/z 952.92–953.22), (f) M+a_3 (m/z 805.05–805.35), (g) M+x_4+1 (m/z 975.0–975.3) and (h) M+y_4 (m/z 948.0–948.3) fragments.

The energy dependence of the fragment corresponding to the protonated monomer $[M+H]^+$ (Figure 6.7a) reaches a maximum at around 7 eV revealing a clear spectroscopic band. If we take the same consideration as in the previous section, suggesting that the peptide bond in small peptides can be approximated with the system containing four energy levels [15], [72–75], then the observed band can be associated with the transition $\pi_2\pi_3^*$ (NV_1). A fast internal conversion to the hot ground state results in a dissociation of weak non-covalently bound dimer complex. The yields for fragments corresponding to H_2O (Figure 6.7b) and CO_2 (Figure 6.7c) neutral loss from the protonated monomer fragment, show an increase towards higher energies, suggesting that dissociation may also proceed with transition $\pi_1\pi_3^*$ (NV_2). The spectroscopic band at 6.7 eV (NV_1 transition) seems to be more pronounced for fragments corresponding to the neutral amino acid losses, specifically tyrosine side chain loss (Figure 6.7e) and phenylalanine loss (Figure 6.7d). All fragment yields presented in Figure 6.8, show distinctive spectral band centered at 6.7 eV. Below the IE, the photo-dissociation of the protonated dimer precursor upon resonant VUV photon absorption proceeds with the electronic excitation, followed by a fast internal energy redistribution to the hot ground state and finally scission of the weak non-covalent bonds as well as the peptide backbone.

Theoretical description of the protonated Leu-enk dimer has been performed by V. Cerovski [77] in order to put the experimental results into perspective. First, the geometries of conformers with the lowest energy are found as in [12] and optimized as suggested by [76] using the B3LYP/6-31+G(d,p) level of DFT. Previously calculated vertical ionization energy for this conformer was 9.31eV [12]. Figure 6.9 presents the lowest energy conformer for protonated dimer.

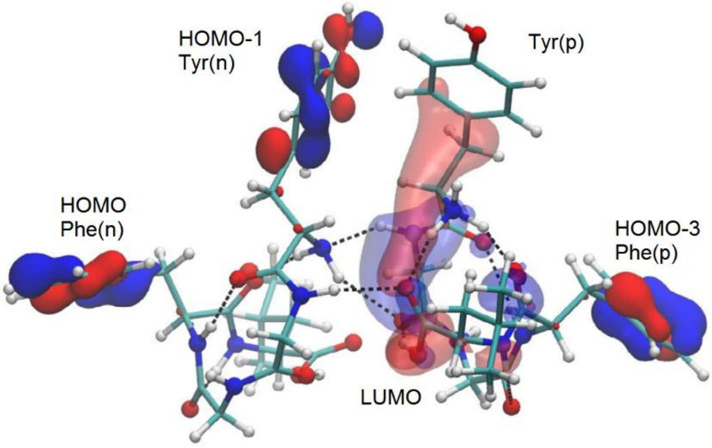

Figure 6.9 - Geometry of the lowest-energy CF found, shown together with several frontier orbitals, as indicated in the figure. HOMO-2 (not shown) is localized on Phe(n) just as HOMO. LUMO+1 and LUMO+2 (not shown) occupy the same part of the molecule as LUMO. (n) and (p) next to the group name indicate whether the group belongs to the neutral or protonated monomer, respectively.

The Leu-enk monomer units are bound by Hydrogen bonds indicated by dashed lines. The monomer molecule with the charge is labeled with (p), while the other neutral monomer molecule is labeled with (n). Four highest occupied molecular orbitals (HOMO) are localized around the aromatic groups (HOMO-2 is covered by the HOMO), while the lowest unoccupied molecular orbital (LUMO) is longitudinally spread across the peptide backbone. Two more orbitals LUMO+1 and LUMO+2 are also positioned across the peptide backbone, although with more density distributed towards tyrosine of the protonated precursor - Tyr(p) in Figure 6.9. Given the obtained electron densities the following transitions could be expected:

$$\mathrm{HOMO} - \mathrm{n} \rightarrow \mathrm{LUMO} + \mathrm{m}, \tag{6.1}$$

where n=0, 1, 2, 3 and m=0, 1, 2. These transitions involve the charge transfer from the aromatic ring to the peptide backbone of the protonated monomer unit. Given the electronic stability of the aromatic ring, the charge transfer is weakening the peptide backbone of the protonated monomer due to the Coulomb repulsion. For this reason, the protonated Leu-enk monomer in a dimer molecule is less stable in comparison with the neutral monomer.

Adenosine 5-monophospate (AMP)

DNA and RNA molecules strongly absorb UV light [78], making them sensitive to photo-induced alterations. Therefore, a large number of studies has been reported on the photo-physics of constituent molecules of DNA [79–82]. Particularly, in relevance to the present results S. Nielsen et al [83], investigated the fragmentation of protonated and deprotonated AMP molecule, induced by 266 nm photons.

Moreover, in nature biomolecules are surrounded by an aqueous environment, which affects their properties and biological functions. With modern experimental techniques, it has become possible to investigate an influence of the solvation on the stability of bio-molecules. Particularly, the effects of solvation at an extreme limit of only a few water molecules called micro- or nano-solvation can be investigated. Various studies have shown that nano-solvation with only one, two or three water molecules can strongly influence chemical reaction dynamics [84], the structure of peptides [85] or stability of a peptide dimer [12]. Dissociation of electrosprayed nanosolvated AMP nucleotides induced by high energy collisions with (Ne, Na) neutral atoms [86] and by electron capture [87], have also been studied.

In this section, our results of VUV action spectroscopy of protonated bare and hydrated AMP nucleotide [88] are presented. Figure 6.10 presents the chemical structural formula of the AMP nucleotide, were Hydrogen nucleus on the right side indicates the protonated singly charged ion $[AMP+H]^+$.

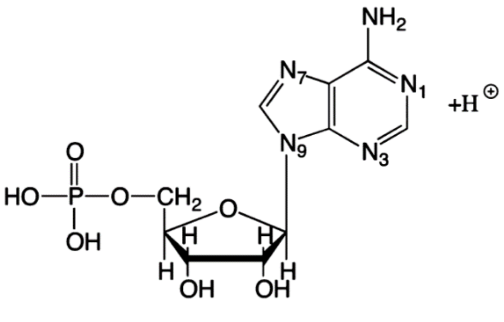

Figure 6.10 - Schematic representation of protonated Adenosine monophosphate molecule.

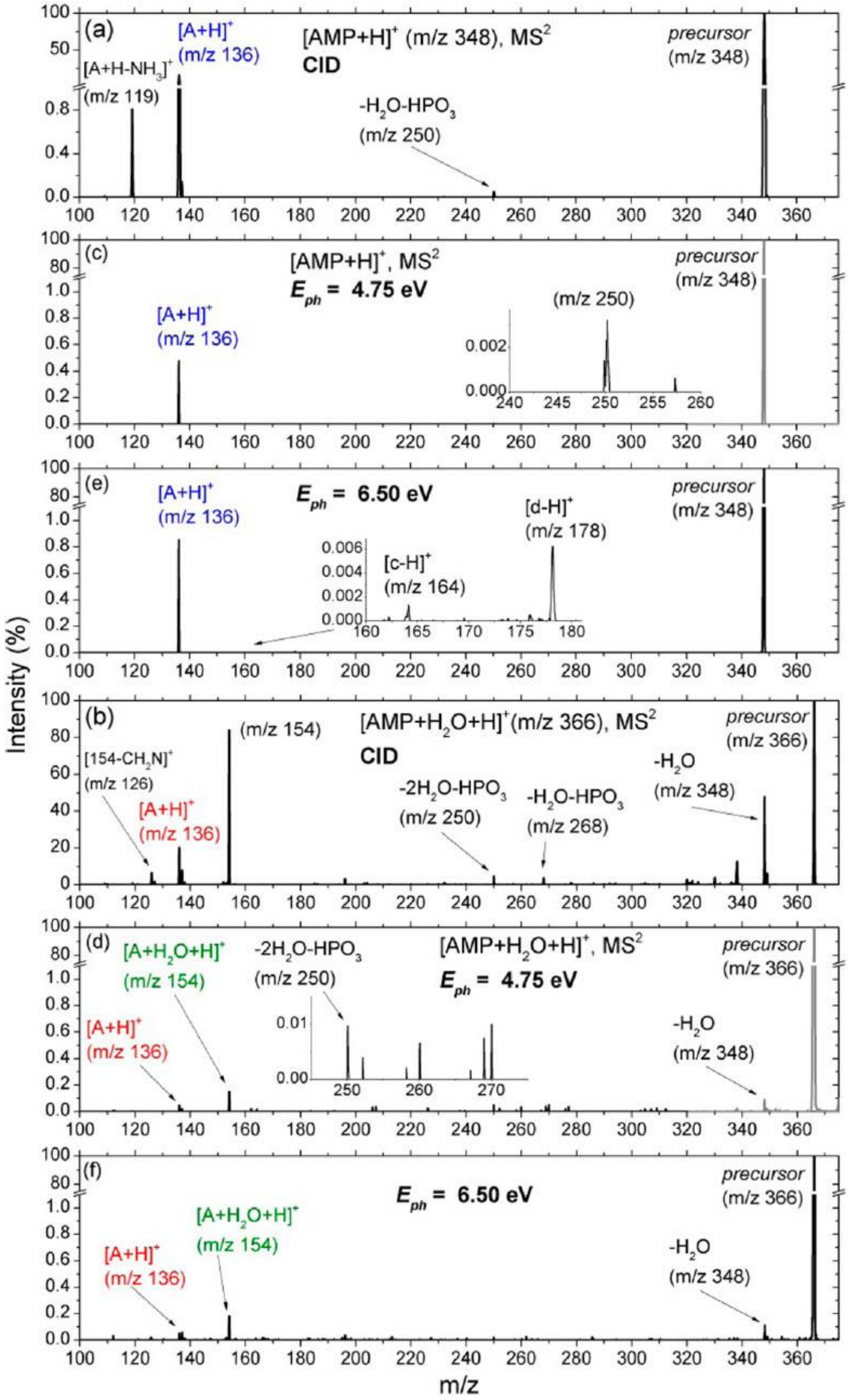

Figure 6.11 - Tandem mass spectrum of protonated [AMP+H]$^+$ and hydrated Adenosine monophosphate precursor ion [AMP+H$_2$O+H]$^+$, obtained for: (a,b) colission induced dissociation (CID); (c,d) VUV photo-induced dissociation at 4.75 eV and (e,f) VUV photo-induced dissociation at 6.5 eV.

Both bare $[AMP+H]^+$ (m/z 348) and hydrated $[AMP+H_2O+H]^+$ (m/z 366) AMP precursors were produced by nano-ESI and isolated in the ion trap. The selected precursors are subjected to UV photons from the DESIRS beamline. The action spectroscopy of the trapped precursors was performed by recording many action MS^2 for energies in the interval from 4 eV to 12.5 eV with 0.2 eV steps.

Figure 6.11a, b presents the action MS^2 of bare and hydrated precursor respectively, obtained with the collision induced dissociation (CID). The action MS^2 for bare and hydrated precursors irradiated at 4.75 eV, are presented in Figure 6.11c and d respectively. Action MS^2 obtained for both precursors at a photon energy of 6.5 eV are presented in Figure 6.11e and f.

In MS^2 from Figure 6.11b, we can see that dominant CID channel for the hydrated precursor is a water molecule loss, resulting in the formation of a fragment designated at m/z 348. It should be noted that a significant contribution to the intensity of the peak at m/z 348 comes from a thermal evaporation of the hydrated precursor, during the trapping time. Indeed, this peak can be observed in MS^2 with a relative intensity of around 0.15 %, even without any activation of the hydrated precursor.

The absorption of a photon below the IE leads to the cleavage of the glycosidic $C-N_9$ bond (see Figure 6.10). This bond scission results in a formation of a fragment at m/z 136, corresponding to protonated adenine base $[A+H]^+$, visible in both MS^2 in Figure 6.11c, e. Qualitatively good agreement is obtained with recent studies of protonated AMP, at 266 nm (≈4.7 eV) [89] and 260 nm (≈4.8 eV) [90]. Still, there are some differences compared with the fragmentation pattern reported by S. Pedersen et al [90]. More specifically, we observe lower abundances of the fragment at m/z 250 corresponding to the phosphate group loss. This difference can be attributed due to a longer fragmentation times of up to 500 ms in the present experiment, in relation to the sector based instruments. The increase of the activation energy to 6.5 eV leads to an increase of the protonated adenine peak at m/z 136.

The observed UV photo-induced fragmentation of the protonated precursor in the present experiment is fundamentally different from studies reported for a deprotonated anion $[AMP-H]^-$ [89, 91]. In those studies, a very rich fragmentation pattern was observed by S. Nielsen et al [91]. They have proposed the following fragmentation mechanism: the photon absorption leads to an electronic excitation into π^* state, accompanied by fast internal conversion to vibrationally excited electronic ground state, which finally decays through many fragmentation channels [80]. However, the lack of fragmentation channels in the present experiment indicates that the protonated cation $[AMP+H]^+$ probably undergoes a photo-dissociation through the cleavage of the glycosidic bond, via fast fragmentation channel directly from the excited π^* state.

In MS^2 from Figure 6.11d and f obtained for the hydrated precursor, we observe a significant (3-4 time fold) decrease in relative intensity of the peak at m/z 136, corresponding to protonated adenine base $[A+H]^+$. Also, one more additional fragment appears at m/z 154, which corresponds to the protonated adenine base bound to one water molecule $[A+H_2O+H]^+$. Furthermore, CID of hydrated precursor (Figure 6.11b) results in an intensive water molecule loss (peak at m/z 348), compared to UV photo-induced dissociation (Figure 6.11d and f). These observations demonstrate the effects of nanosolvation with only one water molecule.

Theoretical calculations were performed by V. Cerovski for bare and hydrated AMP precursors in order to give more insights into the present experimental results. The geometries of conformers (CFs) with lowest energies were found by using the genetic algorithm approach with classical force field geometry optimization. DFT optimizations were then performed at M06-2X/6-311G(d,p) level [92], [93], where 50 lowest energy CFs were considered. Figure 6.12 presents the geometries of lowest energy CFs, CF1 for bare protonated precursor and two conformers CF1', CF2' for protonated hydrated precursor. All these three CFs have their HOMO and LUMO located on the adenine base, with a very small part of the electronic density spread across the rest of the cation. Two CFs are presented for the hydrated precursor, in order to point out two qualitatively different water hydrogen bondings: (1) to the phosphate group away from the adenine base (CF1') and (2) by forming a bridge between the phosphate group and the adenine base (CF2'). Therefore, upon UV photon absorption and scission of glycosidic bond, two main fragments are expected: bare protonated adenine base from CF1' and hydrated protonated adenine base from CF2', as confirmed by the present experimental findings (see Figure 6.11d and f). The calculated vertical ionization energies (VIEs) for CF1, CF1' and CF2' are 12.53 eV, 12.48 eV and 12.12 eV respectively. Binding energies of water hydrogen bonds for CF1' and CF2' are 69 kJ/mol and 69.5 kJ/mol respectively (≈0.72 eV).

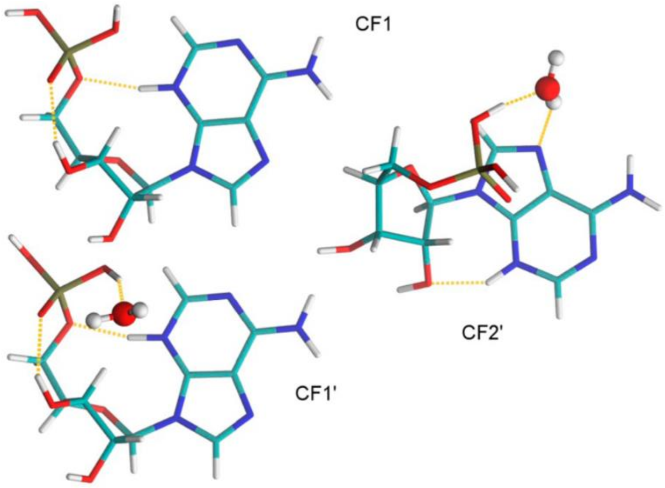

Figure 6.12 - Lowest energy conformers structure found for $[AMP+H]^+$ (CF1) and $[AMP + H2O+H]^+$ (CF1′, CF2′) at M06-2X/6- 311G(d,p) level of DFT. The protonated AMP (CF1) has the protonation site located at N_3 atom.

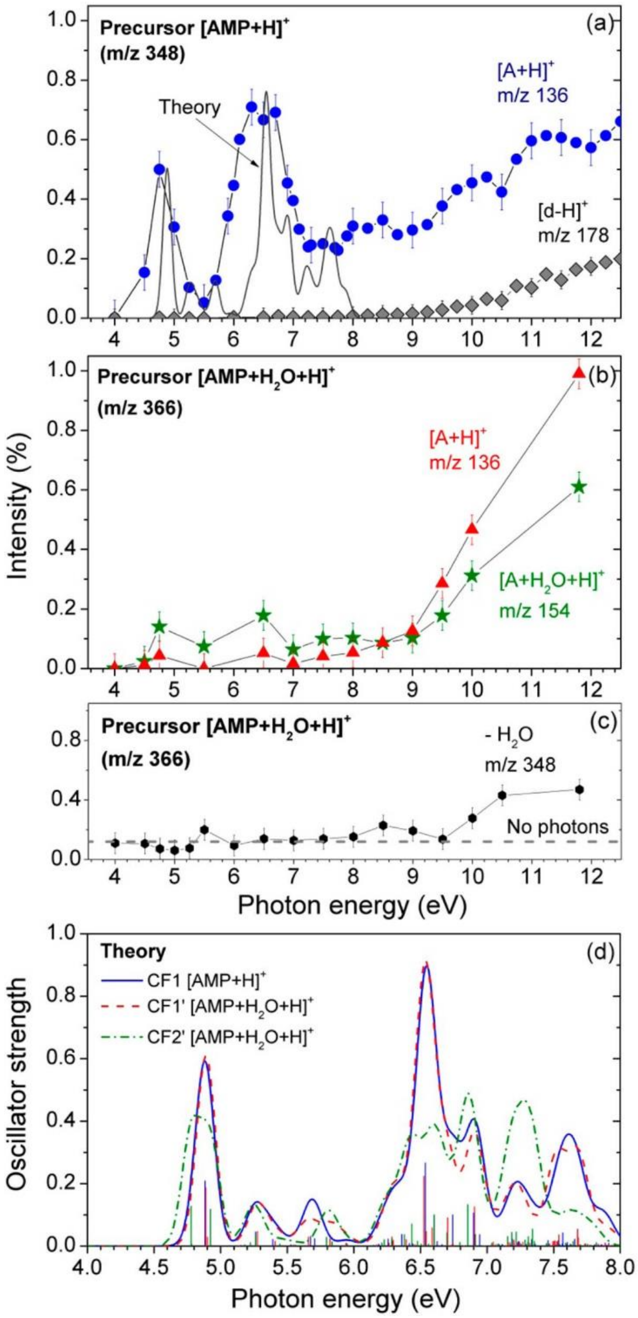

Figure 6.13 - Photodissociation yields of protonated adenine base $[A+H]^+$ (circles) and $[d{-}H]^+$ (diamonds) fragments from the bare protonated precursor $[AMP+H]^+$: (a) yield of $[A+H]^+$ (up triangles) from bare precursor; (b) yield of $[A+H_2O+H]^+$ (down triangles) from the hydrated precursor; (c) yield of $[AMP+H]^+$ fragment from hydrated precursor, corresponding to the loss of a single water. The dashed line marks the average water loss upon thermal evaporation from the ion precursor, without photon irradiation; (d) time-dependent B3LYP/6-31+G(d,p) calculated absorption spectra of conformers from Figure 6.12. Curves are obtained from the sticks by a 0.1 eV Gaussian convolution of the calculated transitions, providing a visual representation (the curve for CF1 is plotted as a full line, normalized to experiment at 4.75 eV).

The energy yields for fragments from bare precursors [AMP+H]$^+$ are presented in Figure 6.13a. The energy yield of protonated adenine base fragment, for bare precursor (circles in Figure 6.13a), shows distinctive resonant spectroscopic features, associated with absorption bands. One band is centered at about 4.75 eV (≈260 nm), which originates from the adenine base and is well known $\pi\pi^*$ transition [78] also found in laser-based experiments. The observed spectral band is in a very good agreement with the absorption band of the protonated adenine base found at 4.7 eV by Pedersen et al [90]. We can also observe a second absorption band centered at about 6.5 eV, which is a dominant photodissociation channel for the bare precursor. Benchmark calculations reported by P. Szalay et al [94], using coupled-cluster methods to find oscillator strengths for adenine base, revealed transitions $3\pi\pi^*$ (6.5 eV) and $4\pi\pi^*$ (6.88 eV). The present experimental results are in a very good agreement with our theoretical absorption spectrum (Figure 6.13d), calculated by using the time-dependent density functional theory (TD-DFT), with B3LYP/6-31+G(d,p) basis set. The theoretical absorption spectrum is approximated by Gaussian convolution with 0.1 eV standard deviation, of calculated transition probabilities (oscillator strengths).

The fragmentation patterns of protonated AMP were reported by A. Bagag et al ([95] and references therein). The process requiring multiple bond cleavages is the mechanism of formation of the fragments [d-H]$^+$ (m/z 164) and [c-H]$^+$ (m/z 178), in MS^2 from Figure 6.11e. Therefore, the yield of the fragment [d-H]$^+$ starts increasing only at higher energies (diamonds in Figure 6.13a). It should be noted that in the present experiment conducted at room temperature, we do not have any control over the conformer formation and distributions. Also, the energies higher than the IE (resulting in a higher density and number of states) were not included in the TD-DFT calculation.

Figure 6.13b presents the energy yields of fragments originating from the hydrated precursor [AMP+H_2O+H]$^+$. The energy yields of fragments corresponding to protonated adenine base (stars) and the protonated adenine base bound with one water molecule (up triangles), also show the spectral features associated with $\pi\pi^*$ transition after photon absorption. The theoretical absorption spectrum of the protonated hydrated precursor presented in Figure 6.13d, for CF1’ (dashed line) is also in good agreement with the measured yield. However, we observe a significant reduction of the peak intensity for the fragment [A+H]$^+$ (Figure 6.11b). It should be noted that B. Liu et al [86] observed that the protection effects of nanosolvation for deprotonated adenine base upon collisions with sodium atoms starts for 10 added water molecules, while a significant dissociation reductions were observed above 13 added water molecules. In the electron capture dissociation (ECD) experiments the fragmentation was even increased with the addition of water molecules [87].

From the present findings, the photo-induced dissociation mechanisms of protonated bare and hydrated AMP nucleotide can be summarized as follows. The CID occurs on the ground electronic state, after statistical redistribution of the absorbed energy over the vibrational modes. UV photoexcitation can result in statistical and non-statistical fragmentation: (a) [AMP-H]$^-$ undergoes fast internal conversion to a vibrationally hot electronic ground state, followed by a thermal (statistical) fragmentation [80]; (b) $[AMP+H]^+$ dissociates directly from excited electronic state (according to present findings and [89], [90]) and (c) $[AMP+H_2O+H]^+$, as we propose, also dissociates from the excited electronic states faster than intramolecular vibrational energy redistribution.

6.1.2 K-shell excitation and ionization of Ubiquitin protein

Proteins play a very important role in vital biological functions of living organisms. The folding - an arrangement of their constituent polypeptide chains in the three-dimensional space, is closely correlated with actual functions that they perform in the living organisms [96]. With the advancements and technological developments of the experimental techniques, an increasing number of studies of protein structures is reported [97]. An already established experimental technique for probing the spectral properties of a wide range of samples including biomolecules is near-edge X-ray absorption fine structure (NEXAFS) spectroscopy [98]. At first, NEXAFS was dedicated to probing samples (with low-Z numbers) prepared as thin films, in order to resolve the structure of molecules bound to surfaces. Recently, Y. Zubavichus and coworkers [99], reported a study where they probed the amino acids and proteins prepared as thin films with soft X-ray photons. In this method, incident SR X-ray photons excite core electrons, usually the ones closest to the nucleus (K-shell), into higher molecular orbitals. If the photon energy is high enough (above K-shell IE), direct transitions into the ionization continuum is also possible. It should be noted that transitions of core electrons into particular molecular excited states prefer certain photon polarizations. Since the polarization of SR produced in modern third generation synchrotrons is completely tunable, NEXAFS technique can be also highly selective. The sensitivity of the technique is also high, provided by the unmatched brilliance of the SR compared to any other X-ray source. An important aspect of the technique is that the incident photon energies are in the range from just slightly below up to 30 eV or so, above the ionization threshold of the molecular target. In this energy range, near-edge X-ray absorption fine structure is characterized by strong and distinctive features, similar to shape resonances [100]. Close inspection of such resonances reveals the electron structure of the target molecules.

With the advent of ESI technique it has become possible to isolate large biomolecular targets such as proteins in the gas phase. By subjecting the trapped biomolecular ions to soft X-ray photons with subsequent acquisition of action tandem mass spectra over near-edge energies, we can perform the action NEXAFS. A. Milosavljević et al [18] recently performed action NEXAFS of the Cytochrome C protein. Our results from the action NEXAFS study involving Ubiquitin protein [101] are presented in this Section.

By means of electrospray ionization, we produced the precursor ions of the Ubiquitin protein with charge states from +4 to +11, which were subjected to X-ray photons in the range of (282-304) eV for C-edge and (394-414) eV for N-edge.

In order to reveal the relaxation processes undergoing in a protein after soft X-ray photon absorption, Auger decay process has to be closely inspected below and above the inner-shell IE. Figure 4.1 presents the scheme for K-shell excitation/ionization of a protein followed by an Auger decay.

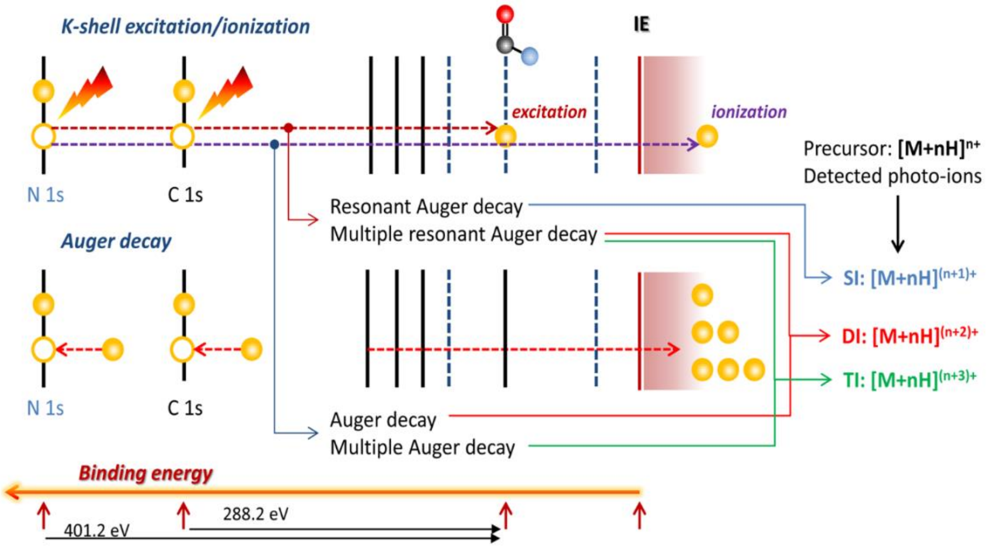

Figure 6.14 - Schematic representation of the K-shell excitation/ionization of a protein, followed by an Auger decay. Adopted from [101].

Below the IE, resonant absorption of a soft X-ray photon leads to excitation of the core electron from K-shell into an unoccupied, bonding molecular orbitals, forming a core hole. A valence electron fills the core hole in the order of femtoseconds and the system relaxes with an ejection of an electron. The process is called the resonant Auger decay [102]. It is possible that multiple valence electrons are ejected owing to a multiple Auger Decay [103]. However, the single ionization of the precursor ion is the most probable relaxation channel. In general, for n-time multiply charged protein precursor, resulting relaxation channels are represented by relation (6.2) [101]:

$$[\mathrm{M}+\mathrm{nH}]^{\mathrm{n}+}+\mathrm{h}\nu \rightarrow [\mathrm{M}+\mathrm{nH}]^{\bullet(\mathrm{n}+\mathrm{k})+}+\mathrm{ke}^{-}\text{, where } \mathrm{k}=1,2,\ldots \tag{6.2}$$

Above the K-shell IE, a core electron is directly ejected into the ionization continuum creating a core hole, which triggers the normal Auger decay. In this process, the double or multiply ionized precursor ion is created. Relation (6.3) [101] describes the resulting process:

$$[\mathrm{M}+\mathrm{nH}]^{\mathrm{n}+}+\mathrm{h}\nu \rightarrow [\mathrm{M}+\mathrm{nH}]^{\bullet(\mathrm{n}+1+\mathrm{k})+}+(\mathrm{k}+1)\mathrm{e}^{-}\text{, where } \mathrm{k}=1,2,\ldots \tag{6.3}$$

MS^2 obtained at a photon energy of 288.2 eV, for 5+ precursor charge state of the Ubiquitin protein is presented in Figure 6.15. The spectrum was normalized to the intensity of precursor ion [M+5H]$^{5+}$ designated at m/z 1714. Dominant relaxation channels correspond to single (SI), double (DI) and tipple ionization (TI) of the precursor ions. They appear in the spectrum at mass-to-charge ratios of 1428, 1224 and 1071 respectively. It could also be seen that peaks corresponding to ionization are followed by clearly resolved low-mass neutral losses. All these relaxation channels are a consequence of the resonant Carbon (1s→π^*_{amide}) X-ray photon absorption.

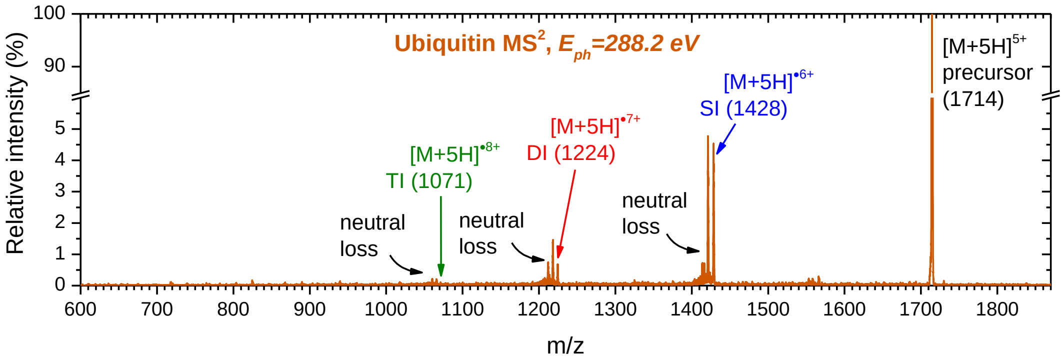

Figure 6.15 - Tandem ESI/photoionization mass spectrum of Ubiquitin protein, 5+ charge state precursor, obtained after photon impact at 288.2 eV. Adopted from [101].

The action K-shell NEXAFS around C-edge and N-edge energies of Ubiquitin protein was obtained by acquiring many action MS^2 around 300 eV and 400 eV photon energy regions respectively, with 0.2 eV energy steps. The ion yields for SI, DI and TI of Ubiquitin 5+ precursor [M+5H]$^{5+}$, were extracted from these MS^2 by integrating the area under the corresponding peaks, normalizing to the total ion current and the photon flux and finally by plotting against the photon energies. Figure 6.16 presents the obtained photoionization yields.

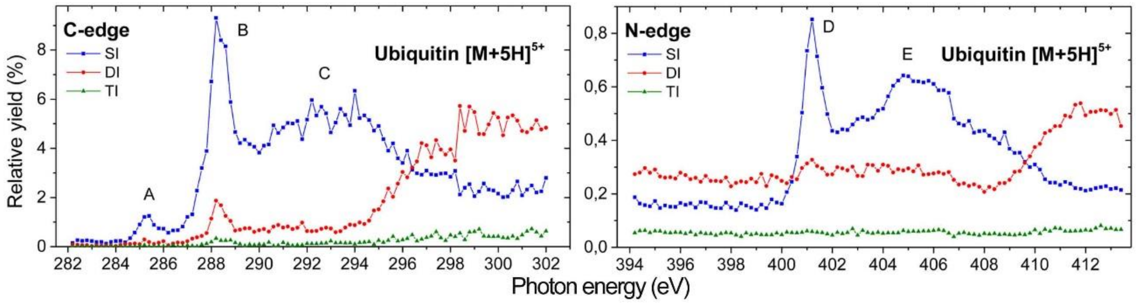

Figure 6.16 - K-shell photoionization energy yields of the Ubiquitin protein, 5+ charge state precursor: (a) C-edge and (b) N-edge. Peaks are integrated over the range Δm/z=±1 around, SI - single ionization [M+5H]$^{•6+}$ (m/z 1428), DI - double ionization [M+5H]$^{•7+}$ (m/z 1224) and TI - triple ionization [M+5H]$^{•8+}$ (m/z 1071). Adopted from [101].

Prominent spectroscopic features (bands) are visible for SI yields in Figure 6.16. The clearly resolved bands are marked with letters A, B and D. Bands A and B are associated with excitations of Carbon core electron 1s, into molecular orbitals corresponding to $\pi^*_{C=C}$ (aromatic) at 285.3 eV and $\pi^*_{C\text{-}N}$ (amide) at 288.2 eV, respectively. The excitation of Nitrogen 1s electron into molecular orbital corresponding to peptide bond $\pi^*_{C\text{-}N}$ (amide) at 401.2 eV is associated with band D. Bands C and E originates from an overlap of many transition contributions mainly associated with σ^* resonances [18].

DI yields from Figure 6.16, show an increase at around 294 eV (C-edge) and 409 eV (N-edge) as a result of the opening of the direct double ionization channel. Since the yields are not background subtracted it should be noted that DI can still dominantly occur even below the IE thresholds due to multiple resonant Auger decay, initiated by resonant Carbon (or Nitrogen) core 1s electron excitation into bonding molecular orbitals. Looking at relation (6.2), if we take k=2 (for double Auger decay) and n=5 (5+ charge state), it would yield $[M+5H]^{\bullet 7+}$ with m/z 1224 - corresponding to DI peak. Considering the C-edge, both SI (from resonant Auger decay) and DI yields (from resonant double Auger decay) below the IE, are dominantly triggered by the same process C $1s \rightarrow \pi^*_{amide}$. Therefore, their shapes in this energy region should in principle be similar, which indeed is the case (see Figure 6.17).

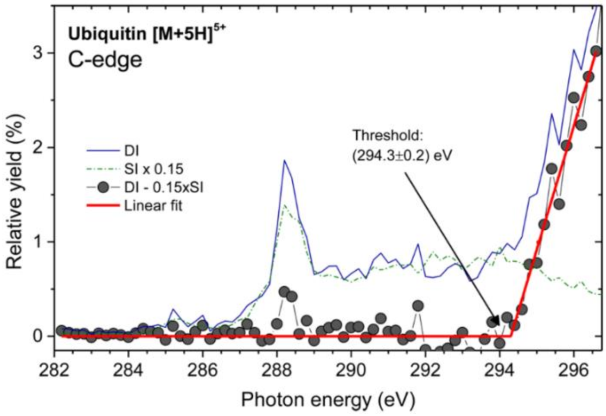

Figure 6.17 - Normalized single (SI, $[M+5H]^{6+,}$ m/z 1427−1429) and double (DI, $[M+5H]^{7+,}$ m/z 1223−1225) C K-edge photoionization yields of the 5+ charge state precursor $[M+5H]^{5+}$ of ubiquitin protein. Circles represent a difference DI − 0.15 × SI, resulting in normal Auger decay contribution of DI yields fitted to a linear threshold model (line). Adopted from [101].

In order to remove the multiple Auger contribution in DI yield, we performed the following procedure. By downscaling the SI with a factor of 0.15 and fitting the difference Δ=DI-0.15*SI with a linear threshold, we obtain the appearance energy (threshold) for DI. The obtained threshold curve (thick red line in Figure 6.17) now represents the contribution to direct K-shell ionization, which is possible only above IE. With this procedure we obtained the IE of 5+ charge state of Ubiquitin protein at (294.3±0.2) eV.

6.2 Electron experiments

6.2.1 Test measurements

Testing of the experimental setup is performed in two steps. The first step involves tuning the electrode voltages to optimal values and the characterization of the electron beam in the continuous mode. In the second step, the trapped ions are subjected to the pulsed beam of electrons of a defined energy during an optimal irradiation time, which has been defined previously.

In order to perform the optimization of the electrode voltages in the electron gun, the ion trap in the LTQ was temporarily modified, to allow for the electron current measurements. The electrical setup for the current measurement is presented in Figure 6.18. During the current measurements, all ion optics lenses including the ion trap and the detectors were turned off. Only the internal turbo pump has to be switched on.

The ion trap in the LTQ is equipped with two end disc plates, which appeared convenient for current measurement. The size of the aperture on both plates is 2 mm. This aperture was used for the beam profile measurement. The original wires in LTQ which supply the voltage to the front and back disc plates were disconnected from the ion trap. Two Teflon insulated Copper wires are connected instead, one on each plate of the ion trap. The front plate of the ion trap is grounded. The back plate is closed with the Aluminum foil, connected to the pico-ampere meter and polarized to +24 V relative to the ground, as depicted in Figure 6.18. The distance between the last electrode of the electron gun and the front plate of the ion trap is approximately 110 mm. The back plate is positioned at 65 mm from the front plate. Therefore, the final distance from the electron gun to the current measuring point was around[15] 175 mm.

---

[15] This distance is a close estimation, since flexible bellows position is changed during optimal alignment. Also, it can contract slightly once the pressure inside the vacuum manifold reaches ultra-high vacuum. For this reason, a final distance is estimated with uncertainty of up to 5 mm.

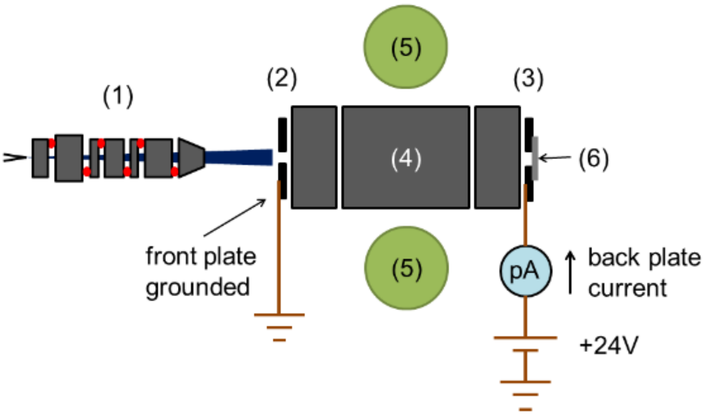

Figure 6.18 - An electrical scheme for the current measurement: 1) electron gun, 2) LTQ front plate - grounded, 3) LTQ back plate - connected to the pico-ampere meter, 4) ion trap, 5) ion detectors and 6) aluminum foil attached to back plate.

By measuring the continuous electron current on the back plate of the ion trap, optimal adjustment of the electrode voltages and characterization of the geometrical properties of the electron beam inside the ion trap was done. The results of the measurements are presented in Figure 6.19. The smallest spot size of the electron beam (or optimal focusing) on the back plate of the ion trap is indicated by the maximal back plate current reading. Optimal focusing, for a given electron energy is achieved by adjusting the voltage on the electrode V in the electron gun (for reference see Figure 4.34 or Figure 4.39). The back plate currents measured for different electron energies are presented in Figure 6.19a.

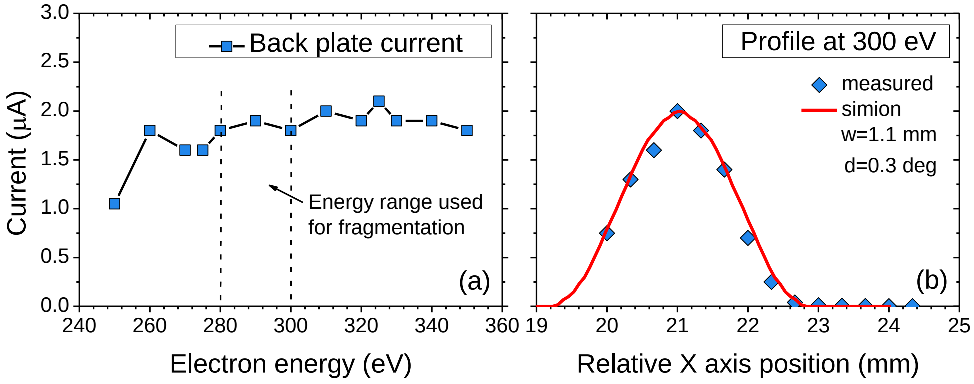

Figure 6.19 - Electron current measured at the back plate of the ion trap: a) plot of the back plate current versus the electron energy and b) electron beam profile. Simulated profile in SIMION is obtained for the beam width of 1.1 mm and pencil angle of 0.3 degrees and is in a good agreement with the measured profile.

The back plate current does not change significantly within the energy span of almost 100 eV. In particular, we were interested in a small energy range around 300 eV, corresponding to C K-shell edge. The mentioned energy range of (280-300) eV is indicated by the dashed lines in Figure 6.19a. The current in this part of the energy range is practically constant around the value of 1.8 μA. Therefore, a normalization of the ion fragment intensities in the marked energy range was not necessary.

The electron beam profile is obtained by moving the LTQ mass spectrometer sideways relative to the vacuum assembly. The recorded profile for the electron energy of 300 eV is presented in Figure 6.19b. Due to the limitation in the maximal sideway extension of the flexible bellows, the measured profile is not fully completed. A programing code is written in PC program SIMION, in order to simulate the geometrical properties of the electron beam. The code is presented in Appendix 8.1. A good agreement with the measured beam profile is obtained for a simulated electron beam width of 1.1 mm and a pencil angle (divergence) of 0.3 degrees. According to the simulation, the electron beam width at the front plate of the ion trap is ≈2 mm. The obtained beam profile is very similar to the measured beam profiles for the same electron gun in the experimental setup UGRA from Belgrade. This was expected since no external electric fields from the ion trap are present during the electron current measurements. After the initial testing of the electron gun in the continuous mode, all original electrode connections of the ion trap were reverted back to its previous state.

The trapped molecular ions are activated in collisions with electrons, during the activation time. Part of the electron energy is absorbed by a molecular ion, which leads to the fragmentation and ionization. An important question is for how long activation time should last, before reaching a saturation of the signal intensity or even a detector damage?[16]. To establish optimal activation time under present experimental conditions, trapped molecular ions were probed with different electron beam pulse widths.

Prior to the ion activation, tests with lowered detector multiplier voltages were performed, in order to find their safe operating values. The beam of electrons was introduced in an empty ion trap, without selecting any ions. The detection and the mass spectrum acquisition was turned on, but with zero electron multiplier voltages on both detectors. For safety reasons, we decided to use only one detector. The electron multiplier voltages were gradually increased until normal values were reached, while constantly checking the mass spectrum. Since no abnormalities were present in the mass spectrum, typical working multiplier voltage of -1234 V (for positive ion mode) was set on the first detector, while the other one was kept at 0 V.

Precursor ions of Ubiquitin protein with charge state 7+ were produced by ESI and isolated in the ion trap. The trapped ions were subjected to short bursts of 300 eV electrons during a specified activation time (defined by the pulse width). An averaged tandem mass spectrum was recorded during 3 min for every pulse width. By this procedure, the MS^2 were obtained for pulse widths of: 2, 5, 10, 20, 50, 100, 200, 500 and 1000 ms. The MS^2 acquisition delay for each pulse width is presented in Table 6.1. The intensities of several selected ion fragments of the interest were extracted and plotted against pulse widths in

---

[16] See Section 4.3, for description of the LTQ mass spectrometer detection system.

Figure 6.20. An example of one of the action MS^2 obtained for 500 ms pulse width, is presented in Figure 6.21.

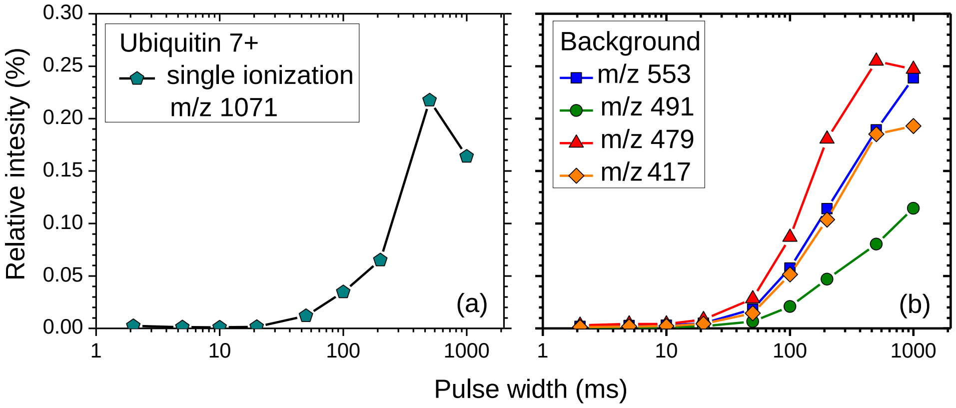

Figure 6.20 - Ion signal versus pulse width, measured for Ubiquitin 7+ precursor: a) peak at m/z 1071 corresponding to the single ionization of the parent ion and b) fragments originating from the electron background noise.

Table 6.1 - Acquisition parameters for the obtained MS^2 for Ubiquitin protein.

Pulse width [ms]	**2**	**5**	**10**	**20**	**50**	**100**	**200**	**500**	**1000**
Act. time [ms]	30	30	30	100	100	200	400	1000	2000
Acq. delay [ms]	28	25	20	80	50	100	200	500	1000

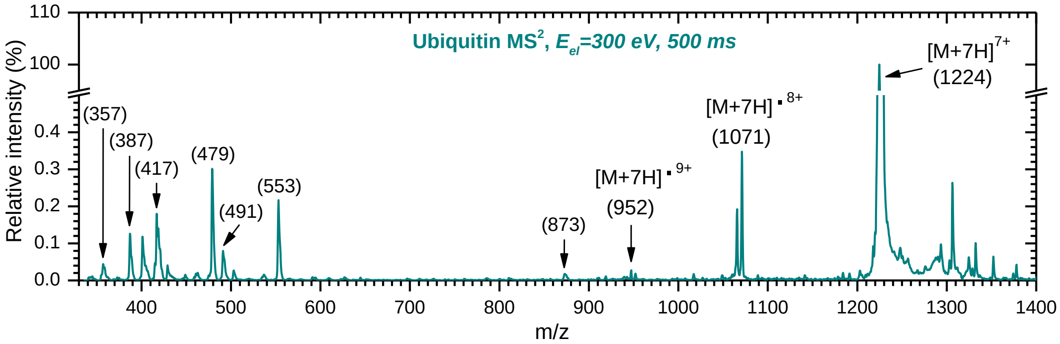

Figure 6.21 - Tandem mass spectrum recorded for Ubiquitin protein, precursor charge state 7+, for the electron energy of 300 eV and the pulse width of 500 ms. The spectrum was not background subtracted and contains both ion fragments and the noise signal.

The ion fragment designated at m/z 1071 in Figure 6.21 corresponds to the single ionization of the parent Ubiquitin precursor ion. The intensities of this ion fragment obtained for different pulse widths are presented in Figure 6.20a. The peaks in the low mass region in Figure 6.21 with mass-to-charge ratios 553, 479, 417, 387, 357 do not originate from the isolated precursor ion. The intensities of the background noise peaks in relation to the pulse widths are presented in Figure 6.20b. They can be observed in the MS^2 even when no ions were isolated in the ion trap, thus we consider them as the noise signal. Both the ion fragments and the background start increasing for pulse widths higher than 10 ms, although the background is always slightly higher. Maximum of the intensity for ion fragment m/z 1071 is at 500 ms, while background continue to increase even further with increasing the pulse width. Therefore, based on the fragment intensity values presented in Figure 6.20, 500 ms is selected as optimal activation time (electron beam pulse width) for Ubiquitin protein.

6.2.2 MS^2 examples - Ubiquitin, Substance P and Melittin

Several large bio-molecular targets were introduced into the gas phase and activated in collisions with soft X-Ray energy electrons. In order to demonstrate the effectiveness of the electron activation method, MS^2 are presented for protein Ubiquitin, peptides Substance P and Melittin.

It should be noted that peaks with relatively high intensities appear in the low mass region in every MS^2. Their origin is not from the trapped precursor ions and they are regarded as the background noise. The most probable cause of the background could be the ionization of residual impurities on the ion trap electrode surface, as well as from ionization of neutral species produced by ESI. Another possibility could be the direct detection of reflected electrons by electron multipliers in the detectors. Increasing the acquisition delay reduces the background, but with an expense of a decrease in ion fragment intensities. Therefore, depending on the abundance of the produced precursor ions, both the electron beam pulse width and the acquisition delay have to be optimized. For the purpose of the background noise subtraction, MS^2 for each molecular target was recorded three times: a) electrons and ions, b) electrons only and c) ions only. The final MS^2 presented below were obtained by (b) from (a). Additionally, MS^2 obtained with electrons only is presented for each target, to reflect the slight change of the experimental conditions (regarding the neutral species content).

Ubiquitin, $[M+7H]^{7+}$

Ubiquitin is a small protein composed of 76 amino acids, which exists in almost all eukaryotic cells and has a molecular weight of 8565 g/mol.

The precursor ions with charge state 7+ from Ubiquitin protein, were selected in the ion trap and subjected to the electron impact at 288 eV electron energy. Figure 6.22 presents the MS^2 recorded without any ions produced, whereas Figure 6.23 presents the background subtracted MS^2 obtained for 288 eV electron energy.

The tandem mass spectrum presented in Figure 6.22 contains strong peaks designated at mass-to-charge ratios 360, 387, 401, 417, 479, 491, 553 and 873. The MS^2 is recorded for the electron energy of 288 eV, for 500 ms pulse width, 200 ms acquisition delay and is normalized to the intensity of the strongest peak at m/z 479. The mentioned peaks that dominate the spectrum, along with all other visible peaks, represent the noise signal since there are no trapped precursor ions. Without a precise knowledge of the residual content in the ion trap, it is not possible to assign these peaks. Therefore, so far, their assignment remains unknown.

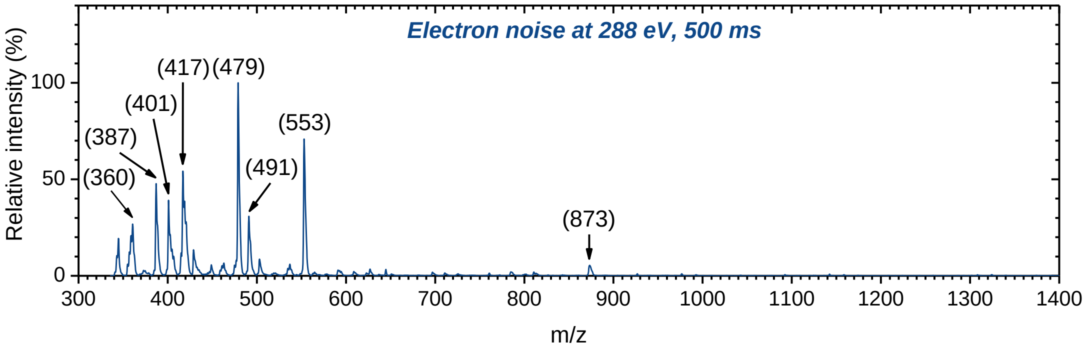

Figure 6.22 - Mass spectrum recorded with no isolated ions, for electron impact energy of 288 eV, 500 ms pulse width and 200 ms acquisition delay, acquired during 3 min.

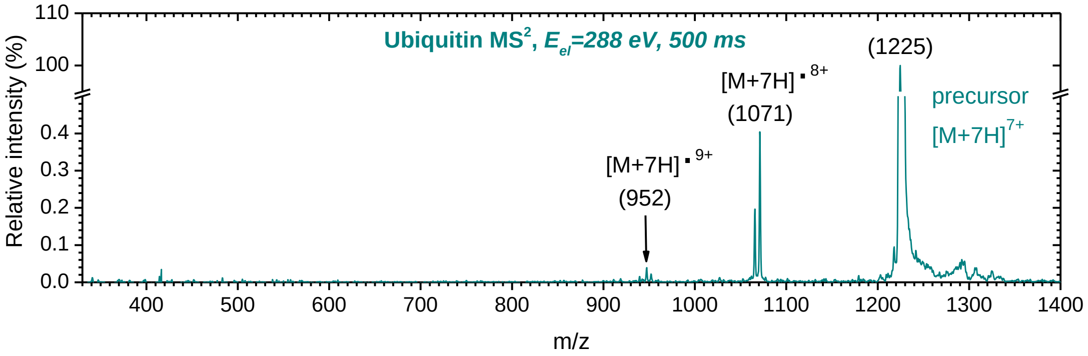

Figure 6.23 - Tandem mass spectrum recorded for 288 eV electron impact with protein Ubiquitin, 7+ charge state precursor. Electron beam pulse width is 500 ms, with acquisition delay of 200 ms, acquired during 3 min.

MS^2 presented in Figure 6.23 was acquired during 3 min, it is background subtracted and normalized to the intensity of the precursor ions designated at m/z 1225. Distinctive peaks are observed at mass-to-charge ratios 1071 and 952. They correspond to the single and double K-shell ionization of the precursor ions, respectively. More details are given in the Section 6.2.3.

Substance P, [M+H]$^+$

Consisted of 11 amino acids, Substance P is a neuropeptide with a molecular weight of 1347 g/mol. It acts as a neurotransmitter and neuromoderator. A comprehensive review of the Substance P was reported by S. Harrison at al [104].

The singly charged precursor ions of Substance P peptide are selected in the ion trap and subjected to electron impact at two energies. Figure 6.24 presents the MS^2 obtained with no ions selected, for 293 eV electron energy. Background subtracted MS^2 obtained for electron energies of 288 eV and 293 eV, are presented in Figure 6.25 and Figure 6.26 respectively.

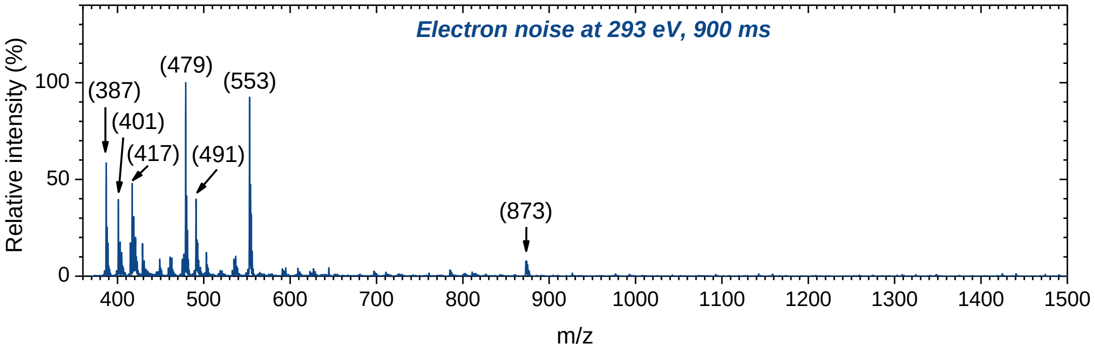

Figure 6.24 - Mass spectrum recorded with no isolated ions, for electron impact energy of 293 eV, 900 ms pulse width and 100 ms acquisition delay, acquired during 3 min.

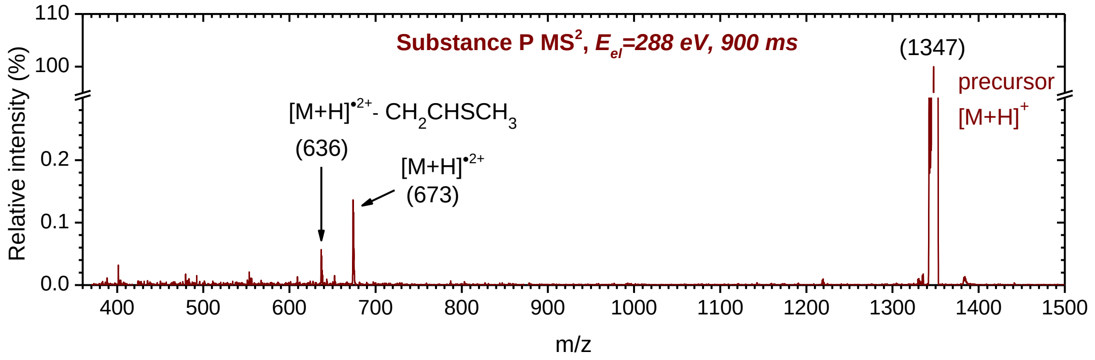

Figure 6.25 - Tandem mass spectrum recorded for 288 eV electron impact with peptide Substance P, singly charged precursor. Electron beam pulse width is 900 ms, with acquisition delay of 100 ms, acquired during 15 min.

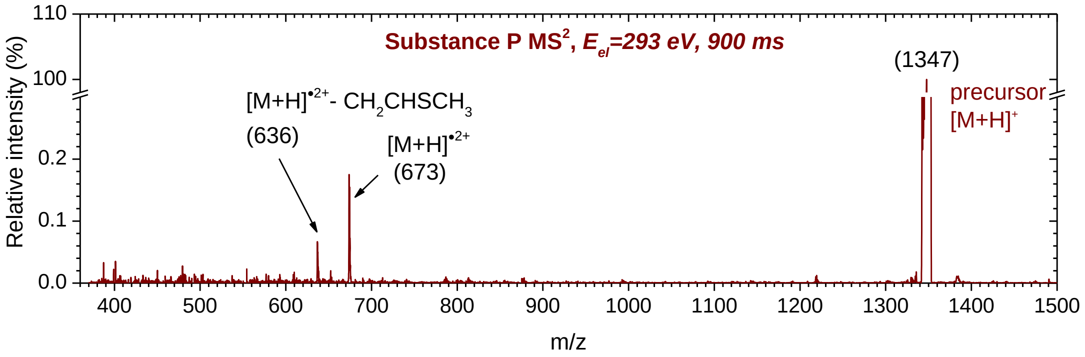

Figure 6.26 - Tandem mass spectrum recorded for 293 eV electron impact with peptide Substance P, singly charged precursor. Electron beam pulse width is 900 ms, with acquisition delay of 100 ms, acquired during 15 min.

Compared with the MS^2 presented in Figure 6.22, the same peaks corresponding to the noise signal dominate the lower mass region of the MS in Figure 6.24. A distribution of peak intensities is slightly different, given that the electron beam pulse width, the energy and the acquisition delay are also different. A decreased acquisition delay of 100 ms, yields higher overall noise. Unassigned noise peaks in Figure 6.24 with mass-to-charge ratios of 387, 553 and 873 show relative intensity increase, in comparison with the same peaks obtained at an electron energy of 288 eV (Figure 6.22).

Besides singly charged Substance P precursor ion [M+H]$^+$ designated at m/z 1374, the tandem mass spectra presented in Figure 6.25 and Figure 6.26 also reveal the ion fragments. In order to compensate for the low abundancy of precursor ions produced by ESI, the electron beam pulse width was increased to 900 ms and the MS^2 were acquired during 15 min. The peak at m/z 673 corresponds to the radical cation [M+H]$^{\bullet 2+}$ originating from the single ionization of the precursor ion, due to the Auger decay. After the neutral loss of CH_2CHSCH_3, part of the methionine residue usually present in proteins, radical cation [M+H]$^{\bullet 2+}$ forms the ion fragment with a mass-to-charge ratio of 636. This ion fragment is also reported by Canon et al [15], in a comprehensive fragmentation study of the trapped Substance P cations, activated with VUV photons from synchrotron radiation. Comparing the two MS^2 presented in Figure 6.25 and Figure 6.26, we observe a slight increase in the relative intensities of ion fragments at m/z 673 and 636, for the electron activation energy of 293 eV.

Melittin, [M+2H]$^{2+}$

Melittin peptide is present in the honey bee venom and is composed of 26 amino acids, with a molecular weight of 2846 g/mol.

Doubly charged precursor ions of Melittin peptide, are selected in the ion trap and subjected to the electron impact at the energy of 293 eV. Figure 6.27 presents the MS obtained with no ions selected, at 293 eV electron energy. A background-subtracted MS^2 obtained for electron energy of 293 eV is presented in Figure 6.28.

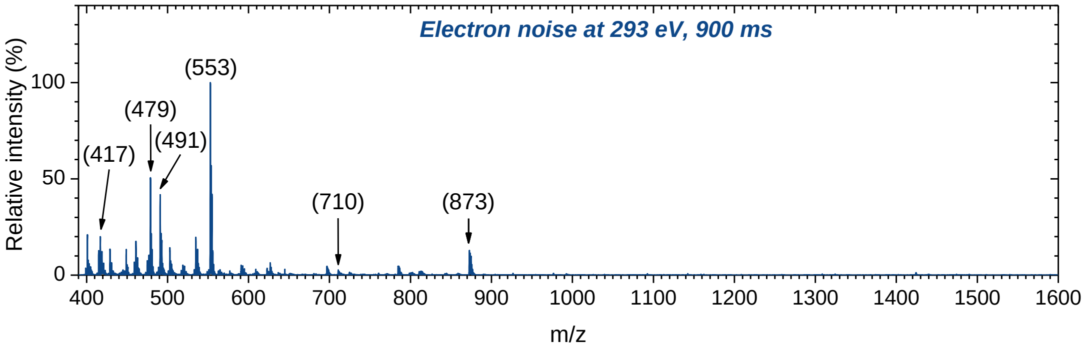

Figure 6.27 - Mass spectrum recorded with no isolated ions, for electron impact energy of 293 eV, 900 ms pulse width and 100 ms acquisition delay, acquired during 5 min.

The electron noise mass spectrum presented in Figure 6.27 is also characterized by the distinctive peaks in the low mass region. The peak designated at m/z 553 shows up as the strongest and followed by the peak at m/z 479. Even though the electron energy, the pulse width and the acquisition time are the same as for the Substance P in Figure 6.24, the distribution of the noise peak intensity is different. The different noise peak distributions suggest that experimental conditions are changed if a new analyte solution was injected into ESI, even though the precursor ions were not isolated in the ion trap. Compared with the electron noise obtained for Ubiquitin and Substance P, the noise peak observed at m/z 873 in Figure 6.27 appears with an increased intensity.

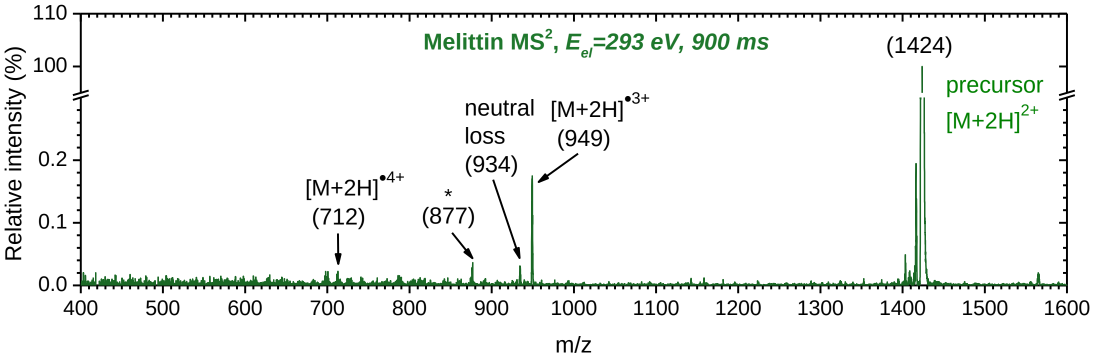

Figure 6.28 - Tandem mass spectrum recorded for 293 eV electron impact with peptide Melittin, doubly charged precursor. Electron beam pulse width is 900 ms, with acquisition delay of 100 ms, acquired during 25 min.

The tandem mass spectrum presented in Figure 6.28 shows a strong ion fragment at m/z 949, corresponding to the radical cation $[M+H]^{\bullet 3+}$. It is formed by single ionization of the precursor ion at m/z 1424 followed by an Auger decay. After a neutral loss of about 45 amu from the radical cation $[M+H]^{\bullet 3+}$, the peak with the mass-to-charge ratio of 934 is formed. The radical cation $[M+H]^{\bullet 4+}$ that corresponds to double ionization of the Melittin precursor ion would appear in the spectrum at m/z 712. Although the MS^2 in Figure 6.28 is background subtracted, it is not entirely clear if the small peak observed at m/z 712 can be assigned to this radical cation. The electron noise MS^2 from Figure 6.27, does show a small noise peak at m/z 710. This noise peak is very close to the radical cation peak at m/z 712, thus there is a possibility that we observe a noise signal instead. Another peak at m/z 877 also remains unassigned so far. It might be assigned to a neutral loss from $[M+H]^{\bullet 3+}$, corresponding to 216 amu. However, the presence of a broad noise signal peak at m/z 873, clearly visible in the MS^2 from Figure 6.27, brings the ion origin of the peak at m/z 877 into question.

6.2.3 Electron induced action spectroscopy of Ubiquitin protein

Multiply charged precursor ions of Ubiquitin protein, with 7+ charge state were produced by electrospray ionization and activated with electrons. Electron energy was scanned near Carbon K-edge, from 280 eV to 300 eV. The same target was also probed with soft X-ray photons, by A. Milosavljevic et al [101]. The two obtained action MS^2 for practically the same incident energies of 288 eV, are compared in Figure 6.29 [105].

Figure 6.29a presents the action MS^2 obtained for the electron activation of the trapped precursor ions $[M+7H]^{7+}$ at m/z 1225, at the electron energy of 288 eV. The dominant relaxation channel corresponds to the single ionization of the precursor ion, thus forming the radical cation $[M+7H]^{\bullet 8+}$ with a mass-to-charge ratio of 1071. The triggering process of the Auger decay, in this case is the direct inner-shell excitation by the electron impact. A strong peak is observed near m/z 1066 corresponding to a neutral loss of about 42 amu from the radical cation $[M+7H]^{\bullet 8+}$. Given the reduced m/z resolution, we can tentatively assign the peak due to the amino acid side chain losses. A second strong channel is observed at m/z 952, corresponding to the formation of the radical cation $[M+7H]^{\bullet 9+}$, originating from the double ionization of the precursor ions. The intensive peak at m/z 947 is ascribed to the neutral loss (of about 42 amu) from the doubly ionized precursor ion. Other peaks with very low intensities are also present in the spectrum, although their assignments are not significant for the present study.

Figure 6.29b presents the action MS^2 obtained for the Ubiquitin 7+ precursor ions, at the photon energy of 288.2 eV. These action NEXAFS results are recently reported by A. Milosavljević et al [101]. The experiment is performed by coupling the same LTQ XL mass spectrometer to the soft X-ray beamline PLEIADES, at the synchrotron SOLEIL. It should be noted that m/z resolution of the X-ray action spectrum is higher than the one obtained for the electron activation. The energy of 288 eV, corresponds to a maximum in measured C 1s near-edge excitation function [101]. It could be seen that both fragmentation patterns are very similar. Indeed, in both cases, the ionization of the protein precursor ion, is the result of a resonant Auger decay process. It is triggered by the Carbon 1s electron excitation into higher unoccupied molecular orbitals, resulting in a core hole formation. The system relaxes and an electron is ejected, resulting in a single ionization. Even though the triggering process of the Auger decay is entirely different (photons or electrons), the ionization pattern seems to be very similar.

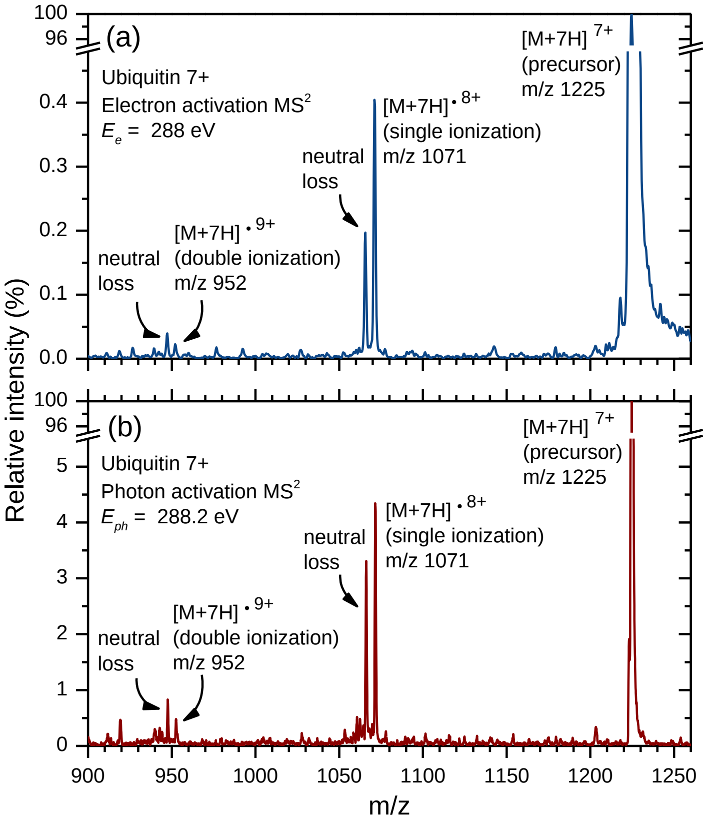

Figure 6.29 - Comparison of tandem mass spectra of Ubiquitin 7+ precursor, for energies near Carbon K-edge activated with: (a) electrons and (b) photons.

If the incident energy is lower than the ionization threshold, governed by the selection rules of a dipole transitions, the X-ray photon can be absorbed by the protein if its energy matches with the energy required by the core electron to undergo a transition from its ground state to the particular unoccupied bound excited state. In short, the photon absorption is a resonant process. In the case of the electron impact, the lower part of the incident electron energy is transferred to the core electron undergoing a transition. The remaining energy is carried away by the scattered electron, suffering the energy loss. Upon core hole formation valence electron fills the core vacancy in the order of femtoseconds [106] and an electron is ejected. In both cases, the process is called the resonant Auger decay, in which the single ionization of the protein precursor ion dominantly occurs. It should be noted that even below the ionization threshold the multiple resonant Auger decay can still occur [103, 107] in which system relaxes with more than one ejected electrons.

In the present experiment, the incident electron energy is only slightly above the transition energy. Thus, the excitation process is performed under so-called near-threshold conditions [108].

The acquisition of many action MS^2 spectra for different photon energies yields the action NEXAFS. In the case of the electron activation, action near-edge electron excitation function (NEEEF) is obtained. Figure 6.30 presents the obtained NEEEF action spectra, for the single and double ionization of the 7+ charge state precursor ions from Ubiquitin protein.

A comparison between the obtained NEEEF and NEXAFS action spectra, obtained for single ionization of the same Ubiquitin protein, is presented in Figure 6.31. The presented energy yields are extracted from MS^2, by normalizing the area under the corresponding peak in the mass spectrum to the total ion current and by plotting it against the incident energy. In the experiment involving photons, an additional normalization to the photon flux was performed. In order to preserve the electron beam geometry and keep the incident electron current constant, the electron gun was refocused for each energy point. The voltages required to refocus the electron gun were determined during the test measurements, prior to the experiment involving activation of trapped ions.

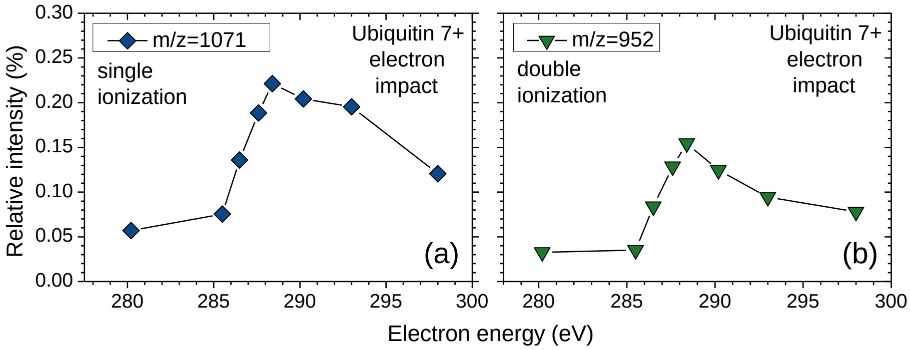

Figure 6.30 - Energy yields of single (a) and double (b) ionization of Ubiquitin protein, 7+ charge state precursor, obtained with electron impact.

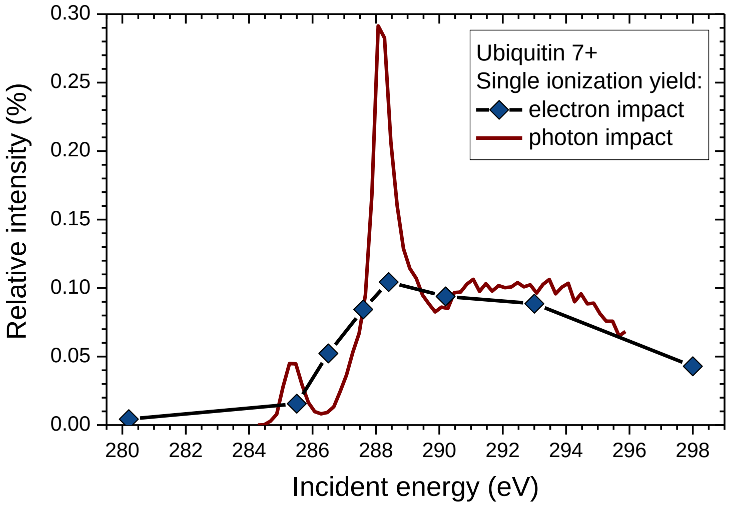

Figure 6.31 - Comparison of single ionization energy yields, obtained for Ubiquitin protein 7+ charge state precursor, for electron and photon impact.

In order to be able to compare the two energy yields from Figure 6.31, both yields are additionally normalized to the same area under the presented curves. The dashed line represents the NEXAFS spectrum, while diamonds represents the normalized NEEEF spectrum for the obtained single ionization (SI) of the Ubiquitin precursor ions. The clear spectroscopic feature appears for both SI yields. For the electron impact, the increase of the cross sections starts at the energy of 284.5 eV, corresponding to the Carbon 1s → $\pi^*_{\text{C=C}}$ (aromatic) transition. The maximum is reached at the energy of 288 eV, which corresponds to the Carbon 1s → $\pi^*_{\text{C-N}}$ (amide) transition. Cross sections of both SI yields, decreases slowly with further increase of the incident energy.

SI yields presented in Figure 6.31 are in a very good agreement, even though the triggering process is intrinsically different. This fact could be of a high importance for the studies involving the radiation damage [109]. Furthermore, the similarity in the obtained action MS^2 (Figure 6.29) as well as in the ionization yields (Figure 6.31), is a proof of principle for our experimental setup for electron activation of trapped ions.

7 Conclusions

The work presented in this Thesis involved the gas-phase photon and electron action spectroscopy of trapped biopolymer ions, as well as bare and hydrated nucleotide ions. The activation of trapped ions was performed by either synchrotron radiation or electron beam produced by a custom designed electron gun. The photon action spectroscopy was performed using the previously developed setup and during the work on this Thesis, the experimental procedures have been improved and new interesting results have been collected and discussed. The experimental setup for coupling a focusing electron gun with the LTQ XL linear ion trap mass spectrometer has been developed during this Thesis. It allowed for performing, for the first time, the electron impact action spectroscopy of trapped macromolecular ions, in the C K-edge ionization region.

The energy dependent fragmentation study of protonated peptide Leu-enk in the VUV photon domain of (5.7-14) eV or (217.5-88.56) nm was performed. In the obtained fragment ion yields, we were able to observe the distinctive spectroscopic band centered at c.a. 6.9 eV ascribed to the peptide $\pi_2\pi_3^*$ (*NV1*) transition. For fragments b_2, b_3, b_4 and y_2 we could also observe the second spectral band centered at c.a. 9.6 eV ascribed to the $\pi_1\pi_3^*$ (*NV2*) transition. We propose that the photo-fragmentation below the IE threshold proceeds on the hot ground electronic state after an internal conversion, following the electronic excitation of the target. The measured photo-dissociation yields of the selected ionic fragments from Leu-enk dimer precursor reveal the absorption bands at about 6.7–7.1 eV (185–175 nm), which is similar to the monomer precursor.

The UV/VUV photo-dissociation of both bare and monohydrated protonated AMP nucleotide isolated in the gas phase, revealed spectral bands located at 4.75 eV and 6.5 eV. It should be noted that the band at 6.5 eV has not been directly measured previously and agree very well with our TD-DFT calculations. However, our studies also showed that the nanosolvation of the AMP nucleotide, with even one water molecule, significantly reduced the dissociation. This could be due to different absorption properties of the hydrated species, according to theoretical analysis.

The inner-shell X-ray action spectroscopy near C and N K-edge of multiply charged Ubiquitin protein (from +4 to +11 charge states) allowed to clearly distinguish the band at 284.5 eV, ascribed to Carbon 1s → $\pi^*_{C=C}$ (aromatic) transition, as well as dominant strong absorption band at 288.2 eV corresponding to Carbon 1s→ π^*_{C-N} (amide) transition. For the N-edge, the spectroscopic band was observed at 401.2 eV corresponding to Nitrogen 1s→ π^*_{C-N} (amide) transition. IE for 5+ charge state precursor ion of Ubiquitin protein was measured at (294.3±0.2) eV.

Finally, we have presented the energy-tunable focused electron beam activation of m/z selected trapped protein ions by coupling an electron gun to a linear quadrupole ion trap mass spectrometer. We have shown that the electron and the X-ray activation of the charged precursor ion of Ubiquitin protein produce very similar MS^2 patterns, which is defined by the resonant Auger decay, regardless of the triggering process. We could also measure the electron-induced single ionization ion yield, that revealed a maximum centered at about 288 eV, in the accord with the soft X-ray measurements. The performed experiments represent a proof of principle for an electron-impact activation method for MS^2 of trapped macromolecular ions, which can be also of interest for top-down protein sequencing.

8 Appendix

8.1 Faraday cup simulation in SIMION

This program was used to simulate and record the electron beam profile for the preset beam width and angle divergence. The final result is plotted in the graph in Microsoft Excel, although that part of the code is not necessary for the simulation. The main program code is contained in the LUA file. The geometry of the electrodes is contained in a separate geometry file (GEM), independent of the main LUA code. Definition of particles is also contained in an independent file (PARTICLES). All three pieces of the code are presented in the following sections.

8.1.1 Faraday cup - LUA code

```
simion.workbench_program()
--global adjustables
adjustable _y_range_mm          -- Y-axis range to scan [mm]
adjustable _points              -- number of data points
adjustable _dy_mm               -- electron beam initial width (window) [mm]
adjustable _da_deg              -- electron beam initial divergence (pupil angle) [mm]
  --Create Excel object (if not exist).
  local excel   -- Excel object
      if not excel then
        _G.excel = _G.excel or luacom.CreateObject("Excel.Application")
        excel = _G.excel
      end
  local wb = excel.Workbooks:Add()     -- Excel workbook
  local ws = wb.Worksheets(1)          -- Excel worksheet
  excel.Visible = false                -- don't show excel window
  -- create function for ploting graph in excel
  local function plot_chart()
    local chart = excel.Charts:Add()
    chart.ChartType = -4169  -- scatter XY
    chart.HasTitle = true
    chart.HasLegend = false
    chart.ChartTitle:Characters().Text = "Faradey cup simulation"
    local range = ws.UsedRange
    chart:SetSourceData(range, 2)
    chart.Axes(1,1).HasTitle = 1
    chart.Axes(1,1).AxisTitle:Characters().Text = "Y(mm)"
    chart.Axes(1,2).HasTitle = 1
    chart.Axes(1,2).AxisTitle:Characters().Text = "Transmission(%)"
  end
-- global help variables
local y_step = _y_range_mm / _points
local current_y = _y_range_mm
-- Counters.
local run=1
```

```
local num_particles
local num_hits
-- SIMION intialize segment.  Called for each particle construction.
function segment.initialize_run()
  assert(current_y)
  assert(y_step > 0)
  assert(_dy_mm > 0)
  assert(_da_deg > 0)
  -- Regenerate particle definitions
  local PL = simion.import 'particlelib.lua'
  PL.reload_fly2('particles.fly2', {
  --variables to pass to FLY2 file.
    current_y=current_y,
    y_step=y_step,
    _dy_mm=_dy_mm,
    _da_deg=_da_deg,
  })
  -- Reset the counter before each rerun
  num_hits = 0
  num_particles = 0
   if run == 1 then  -- when first particle in run is created.
      -- Print parameters used.
      print("Initial parameters:")
      print(string.format("dY=%g[mm], dA=%g[deg]", _dy_mm, _da_deg))
      print(" ")
      print("Y[mm] T[%]")
      print("----------")
   end
end
-- called on each particle initialization inside a PA instance...
function segment.initialize()
end
-- called on each particle termination inside a PA instance...
function segment.terminate()
  -- Count total number of particles
  num_particles = num_particles + 1
  -- Count particles that splat beyond some distance
  if ion_px_mm >= 75.5 then
      num_hits = num_hits + 1
  end
end
-- called on end of each run...
function segment.terminate_run()
  -- Count number of runs
  run=run+1
  -- Print summary and store some data at end of each run.
  local transmission = 100 * num_hits / num_particles
  if run > 2 then       -- skip the first run
  print(current_y+y_step, transmission)
  end
  -- set next y position to scan
  current_y = current_y - y_step
  --fill excel cells with data
```

```
  if run > 2 then       -- skip the first run
    ws.Cells(run,1).Value2 = current_y + 2*y_step
    ws.Cells(run,2).Value2 = transmission
  end
  -- rerun the ions
  sim_rerun_flym = 1
  -- stop reruns if enough data points are reached
  if run > 2*_points+2 then
  sim_rerun_flym = 0
  --Plot chart, make excel visible and reset number of runs
  excel.Visible = true
  plot_chart()  -- create chart
  run=0
  end
end
```

8.1.2 Faraday cup - GEM file

```
pa_define(1957,201,1,cylindrical,y_mirror)
  e(1) ;{fill{within{box(0,0,4,200)}          ;start disc
 locate(1105,0,0)
      {
       within{box(0,0,11,200)}                ;f.c.
       notin{box(0,0,11,8)}                   ;f.c. hole
       locate(663,0,0)
         {
          within{box(0,0,4,200)}              ;detector disc
          }}}}
```

8.1.3 Faraday cup - PARTICLES file

```
local var = _G.var or {}
local y0 = var.current_y
local y_step = var.y_step
local dy = var._dy_mm
local da = var._da_deg
particles {
  coordinates = 0,
  standard_beam {
    n = 121,
    tob = 0,
    mass = 0.00054857990946,
    charge = -1,
    x = 0.401,
    y = arithmetic_sequence
      {
        first = y0+(dy/2),
        step = -(dy/10),
        n = 11
      },
    z = 0,
    ke = 1,
    az = 0,
    el = arithmetic_sequence
```

```
          {
            first = da/2,
            step = -(da/10),
            n = 11
          },
        cwf = 1,
        color = 3
      }
    }
```

8.2 Simulation of the linear quadrupole RF+DC ion trap

This program was used to simulate the transmission of the electron beam through the linear quadrupole ion trap from the LTQ mass spectrometer. This simulation consists of few separate code segments. Particle definitions are used without special coding and are created through the user interface of the SIMION program. The main part of the code (LUA) is presented in the following section, while 3 geometry files with the information of electrode dimensions are given in the sections that follow next.

8.2.1 Ion trap - LUA file

```
simion.workbench_program()
-- Definition of variables.
adjustable DC_voltage_V = 100.0                    -- DC voltage [V]
adjustable RF_frequency_Hz = 1E+6                  -- RF frequancy [Hz]
adjustable RF_voltage_V = 400                      -- RF voltage [V]
adjustable phase_in_deg = 0                        -- Phase angle at ion entrance [deg]
adjustable phase_RF_deg = 180.0                    -- Phase angle between RF rods [deg]
adjustable disk_DC_voltage_V = 0                   -- Disk electrode DC voltage [V]
adjustable katode_V = 0                            -- Katode DCvoltage [V]
adjustable pe_update_each_usec = 0.0001            -- PE display update time step [usec]
adjustable time_step_min = 0.0001                  -- Min time step [usec]
-- Initialising static potentials on Disk electrodes and kathode in instances 1 and 3 only.
function segment.init_p_values()
   if ion_instance == 1 then      -- entrance PA
      adj_elect03 = disk_DC_voltage_V
      adj_elect04 = katode_V
    elseif ion_instance == 3 then  -- exit PA
      adj_elect03 = disk_DC_voltage_V
   end
 end
-- SIMION fast_adjust segment.  Called to override electrode potentials.
function segment.fast_adjust()
local omega = 2 * math.pi * RF_frequency_Hz * 1E-6
local phase_in = phase_in_deg * (math.pi/180)
local phase_RF = phase_RF_deg * (math.pi/180)
  -- Set electrode voltages.
  adj_elect01 = RF_voltage_V * sin (omega * Ion_Time_of_Flight + phase_in) + DC_voltage_V
  adj_elect02 = RF_voltage_V * sin (omega * Ion_Time_of_Flight + phase_in + phase_RF) -
DC_voltage_V
 end
```

```
-- SIMION other_actions segment. Called on each time-step.
local next_pe_update = 0   -- next time to update PE surface display [usec]
function segment.other_actions()
     -- Trigger PE surface display updates. If TOF reached next PE display update time...
   if ion_time_of_flight >= next_pe_update then
      -- Request a PE surface display update.
      sim_update_pe_surface = 1
      -- Compute next PE display update time (usec).
      next_pe_update = ion_time_of_flight + pe_update_each_usec
   end
end
-- SIMION segment called by SIMION to override time-step size on each time-step.
  function segment.tstep_adjust()

 ion_time_step = min(ion_time_step, time_step_min)
 end
```

8.2.2 Ion trap - front section GEM file

```
pa_define (72,72,232,p,xy,e,1)
locate(0,0,0,1,0,0)
{e(4) ; Cathode
{fill{within{box3d(-72,0,0,72,72,5) circle(0,0,10,10)}}}}
locate(0,0,155,1,0,0){e(3) ; Front plate disc
{fill{within{box3d(-72,0,0,72,72,6) circle(0,0,61,61)}
notin{box3d(-72,0,0,72,72,6) circle(0,0,6,6)}}}}
locate(0,0,166,1,0,0){
locate(0,0,0,1,0,0)
{e(1) ; Y-axis electrodes
{fill{within{box3d(-52,0,0,52,72,60) hyperbola(0,0,16,17)}}}}
locate(0,0,0,1,0,-90)
{e(2) ; X-axis elektrodes
{fill{within{box3d(-52,0,0,52,72,60) hyperbola(0,0,16,17)}}}
```

8.2.3 Ion trap - center section GEM file

```
pa_define (72,72,1,p,xy,e,1)
locate(0,0,0,1,0,0){
locate(0,0,0,1,0,0)
{e(1) ; Y-axis electrodes
{fill{within{box(-52,0,52,72) hyperbola(0,0,16,17)}}}}
locate(0,0,0,1,0,-90)
{e(2) ; X-axis electrodes
{fill{within{box(-52,0,52,72) hyperbola(0,0,16,17)}}}}}
```

8.2.4 Ion trap - back section GEM file

```
pa_define (72,72,82,p,xy,e,1)
locate(0,0,70,1,0,0)
{e(3) ; Detector disk
{fill{
within{box3d(-72,0,0,72,72,6) circle(0,0,61,61)}
notin{box3d(-72,0,0,72,72,6) circle(0,0,6,6)}}}}
locate(0,0,5,1,0,0){
locate(0,0,0,1,0,0)
```

```
{e(1) ; Y-axis electrodes
{fill{within{box3d(-52,0,0,52,72,60) hyperbola(0,0,16,17)}}}}
locate(0,0,0,1,0,-90)
{e(2) ; X-axis electrodes
{fill{within{box3d(-52,0,0,52,72,60) hyperbola(0,0,16,17)}}}}
```

9 References

[1] M. A. Śmiałek, P. Limão-Vieira, N. J. Mason, and A. V. Solov'yov, "Radiation damage of biomolecular systems: Nano-scale insights into Ion-beam cancer therapy. 2nd Nano-IBCT conference ∗," *Eur. Phys. J. D*, vol. 68, no. 10, 2014.

[2] I. Baccarelli, F. A. Gianturco, A. Grandi, R. R. Lucchese, and N. Sanna, "Electron-Driven Molecular Processes Induced in Biological Systems by Electromagnetic and Other Ionizing Sources," *Adv. Quantum Chem.*, vol. 52, no. 06, pp. 189–230, 2007.

[3] E. Alizadeh and L. Sanche, "Precursors of solvated electrons in radiobiological physics and chemistry," *Chem. Rev.*, vol. 112, no. 11, pp. 5578–5602, 2012.

[4] M. Yamashita and J. B. Fenn, "Electrospray Ion Source. Another Variation on the Free-Jet Theme," *J. Phys. Chem.*, vol. 434, no. 125, pp. 4451–4459, 1984.

[5] E. De Hoffmann and V. Stroobant, *Mass Spectrometry - Principles and Applications*, Third edit. John Wiley and Sons, Ltd, 2007.

[6] K. Hirsch, J. T. Lau, P. Klar, A. Langenberg, J. Probst, J. Rittmann, M. Vogel, V. Zamudio-Bayer, T. Möller, and B. von Issendorff, "X-ray spectroscopy on size-selected clusters in an ion trap: from the molecular limit to bulk properties," *J. Phys. B At. Mol. Opt. Phys.*, vol. 42, no. 15, pp. 154029–154036, 2009.

[7] R. Thissen, J. M. Bizau, C. Blancard, M. Coreno, C. Dehon, P. Franceschi, A. Giuliani, J. Lemaire, and C. Nicolas, "Photoionization Cross Section of Xe^+ Ion in the Pure $5p^5$ $^2P_{3/2}$ Ground Level," *Phys. Rev. Lett.*, vol. 100, no. 22, pp. 1–4, 2008.

[8] L. Nahon, N. De Oliveira, G. A. Garcia, J. F. Gil, B. Pilette, O. Marcouillé, B. Lagarde, and F. Polack, "DESIRS: A state-of-the-art VUV beamline featuring high resolution and variable polarization for spectroscopy and dichroism at SOLEIL," *J. Synchrotron Radiat.*, vol. 19, no. 4, pp. 508–520, 2012.

[9] A. R. Milosavljević, C. Nicolas, J. F. Gil, F. Canon, M. Réfrégiers, L. Nahon, and A. Giuliani, "VUV synchrotron radiation: A new activation technique for tandem mass spectrometry," *J. Synchrotron Radiat.*, vol. 19, no. 2, pp. 174–178, 2012.

[10] A. R. Milosavljević, A. Giuliani, C. Nicolas, J.-F. Gil, J. Lemaire, M. Réfrégiers, and L. Nahon, "Gas-phase spectroscopy of a protein," *J. Phys. Conf. Ser.*, vol. 257, no. 1, p. 012006, 2010.

[11] A. R. Milosavljević, C. Nicolas, J. Lemaire, C. Dehon, R. Thissen, J.-M. Bizau, M. Réfrégiers, L. Nahon, and A. Giuliani, "Photoionization of a protein isolated in vacuo.," *Phys. Chem. Chem. Phys.*, vol. 13, no. 34, pp. 15432–15436, 2011.

[12] A. R. Milosavljević, V. Z. Cerovski, F. Canon, L. Nahon, and A. Giuliani, "Nanosolvation-induced stabilization of a protonated peptide dimer isolated in the Gas phase," *Angew. Chemie - Int. Ed.*, vol. 52, no. 28, pp. 7286–7290, 2013.

[13] S. Bari, O. Gonzalez-Magaña, G. Reitsma, J. Werner, S. Schippers, R. Hoekstra, and T. Schlathölter, "Photodissociation of protonated leucine-enkephalin in the VUV range of 8-40 eV," *J. Chem. Phys.*, vol. 134, no. 2, pp. 6–10, 2011.

[14] O. González-Magaña, G. Reitsma, S. Bari, R. Hoekstra, and T. Schlathölter, "Length effects in VUV photofragmentation of protonated peptides.," *Phys. Chem. Chem. Phys.*, vol. 14, no. 13, pp. 4351–4354, 2012.

[15] F. Canon, A. R. Milosavljević, L. Nahon, and A. Giuliani, "Action spectroscopy of a

protonated peptide in the ultraviolet range," *Phys. Chem. Chem. Phys.*, vol. 17, no. 17, pp. 25725–25733, 2015.

[16] H. W. Jochims, M. Schwell, J. L. Chotin, M. Clemino, F. Dulieu, H. Baumgärtel, and S. Leach, "Photoion mass spectrometry of five amino acids in the 6-22 eV photon energy range," *Chem. Phys.*, vol. 298, no. 1–3, pp. 279–297, 2004.

[17] M. Schwell, H. W. Jochims, H. Baumgärtel, F. Dulieu, and S. Leach, "VUV photochemistry of small biomolecules," *Planet. Space Sci.*, vol. 54, no. 11, pp. 1073–1085, 2006.

[18] A. R. Milosavljević, F. Canon, C. Nicolas, C. Miron, L. Nahon, and A. Giuliani, "Gas-phase protein inner-shell spectroscopy by coupling an ion trap with a soft X-ray beamline," *J. Phys. Chem. Lett.*, vol. 3, no. 9, pp. 1191–1196, 2012.

[19] K. B. Shelimov, D. E. Clemmer, R. R. Hudgins, and M. F. Jarrold, "Protein structure in Vacuo: Gas-phase conformations of BPTI and cytochrome c," *J. Am. Chem. Soc.*, vol. 119, no. 9, pp. 2240–2248, 1997.

[20] B. A. Budnik, K. F. Haselmann, and R. A. Zubarev, "Electron detachment dissociation of peptide di-anions: An electron-hole recombination phenomenon," *Chem. Phys. Lett.*, vol. 342, no. 3–4, pp. 299–302, 2001.

[21] B. A. Budnik, Y. O. Tsybin, P. Häkansson, and R. A. Zubarev, "Ionization energies of multiply protonated polypeptides obtained by tandem ionization in Fourier transform mass spectrometers," *J. Mass Spectrom.*, vol. 37, no. 11, pp. 1141–1144, 2002.

[22] R. Uy and F. Wold, "Posttranslational covalent modification of proteins," *Science*, vol. 198, no. 4320, pp. 890–896, 1977.

[23] H. A. B. Johansson, "Fragmentation of Amino Acids and Microsolvated Peptides and Nucleotides using Electrospray Ionization Tandem Mass Spectrometry," Licentiate Thesis, Stocholm University, Stocholm, 2010.

[24] P. Roepstor and Fohlman J, "Proposal for a common nomenclature for sequence ions in mass-spectra of peptides," *Biomed. Mass Spectrom.*, vol. 26, no. 11, pp. 672–682, 1984.

[25] A. I. S. Holm, "Bare and Solvated DNA and Peptides. Spectroscopy and Mass Spectrometry," PhD Thesis, Aarhus University, Danemark, 2009.

[26] P. Rossmann, M. G.; Argos, "Protein Folding," *Annu. Rev. Biochem.*, vol. 50, p. 497−532, 1981.

[27] W. Kohn, "Electronic structure of matter - wave functions and density functionals - Nobel Lecture," vol. 71, no. 5, pp. 213–237, 1999.

[28] W. Kohn and L. J. Scham, "Self-Consistent Equations Including Exchange and Correlation Effects*," *Phys. Rev.*, vol. 140, no. 1951, 1965.

[29] M. Dole, L. L. Mack, and R. L. Hines, "Molecular beams of macroions," *J. Chem. Phys.*, vol. 49, no. 5, pp. 2240–2249, 1968.

[30] J. B. Fenn, M. Mann, C. K. A. I. Meng, S. F. Wong, and C. M. Whitehouse, "Electrospray Ionization for Mass Spectrometry of Large Biomolecules," *Science*, vol. 246, no. 6, 1989.

[31] V. Gabellca and E. De Pauw, "Internal energy and fragmentation of ions produced in electrospray sources," *Mass Spectrom. Rev.*, vol. 24, no. 4, pp. 566–587, 2005.

[32] V. Katta, D. T. Chow, and M. F. Rohde, "Applications of in-source fragmentation of protein ions for direct sequence analysis by delayed extraction MALDI-TOF mass

spectrometry.,” *Anal. Chem.*, vol. 70, no. 20, pp. 4410–4416, 1998.

[33] S. Banerjee and S. Mazumdar, “Electrospray Ionization Mass Spectrometry: A Technique to Access the Information beyond the Molecular Weight of the Analyte,” *Int. J. Anal. Chem.*, vol. 2012, pp. 1–40, 2012.

[34] G. Taylor, “Disintegration of Water Drops in an Electric Field,” *Proceedings of the Royal Society A: Mathematical, Physical and Engineering Sciences*, vol. 280, no. 1382. pp. 383–397, 1964.

[35] L. Rayleigh, “On the equilibrium of liquid conducting masses charged with electricity,” *Philisophical Mag.*, vol. 14, no. 87, pp. 184–186, 1882.

[36] P. Kebarle and U. H. Verkcerk, “Electrospray: From Ions in solution to Ions in the gas phase, what we know now,” *Mass Spectrom. Rev.*, vol. 28, no. 6, pp. 898–917, 2009.

[37] J. V. Iribarne and B. A. Thomson, “On the evaporation of small ions from charged droplets,” *J. Chem. Phys.*, vol. 64, no. 6, pp. 2287–2294, 1976.

[38] G. Schmelzeisen-Redeker, L. Bütfering, and F. W. Röllgen, “Desolvation of ions and molecules in thermospray mass spectrometry,” *Int. J. Mass Spectrom. Ion Process.*, vol. 90, no. 2, pp. 139–150, 1989.

[39] J. B. Fenn and S. Nguyen, “Gas-phase ions of solute species from charged droplets of solutions,” *Proc. Natl. Acad. Sci. U. S. A.*, vol. 104, no. 4, pp. 1111–1117, 2007.

[40] M. S. Wilm and M. Mann, “Electrospray and Taylor-Cone theory, Dole’s beam of macromolecules at last?,” *Int. J. Mass Spectrom. Ion Process.*, vol. 136, no. 2–3, pp. 167–180, 1994.

[41] M. Wilm and M. Mann, “Analytical properties of the nanoelectrospray ion source.,” *Anal. Chem.*, vol. 68, no. 1, pp. 1–8, 1996.

[42] P. Wolfgang, “Electromagnetic traps for charged and neutral particles,” *Rev. Mod. Phys.*, vol. 62, no. 3, 1990.

[43] J. E. Coutant and F. W. McLafferty, “Metastable ion characteristics,” *Int. J. Mass Spectrom. Ion Phys.*, vol. 8, no. 4, pp. 323–339, 1972.

[44] S. Bari, O. Gonzalez-Magaña, G. Reitsma, J. Werner, S. Schippers, R. Hoekstra, and T. Schlathölter, “Photodissociation of protonated leucine-enkephalin in the VUV range of 8-40 eV,” *J. Chem. Phys.*, vol. 134, no. 2, pp. 1–9, 2011.

[45] R. Zubarev, N. L. Kelleher, and F. W. McLafferty, “Electron capture dissociation of multiply charged protein cations. A Nonergodic Process,” *J. Am. Chem. Soc*, vol. 120, no. 16, pp. 3265–3266, 1998.

[46] K. Biemann, “Four decades of structure determination by mass spectrometry: From alkaloids to heparin,” *J. Am. Soc. Mass Spectrom.*, vol. 13, no. 11, pp. 1254–1272, 2002.

[47] T. Scientific, “LTQ Series Hardware Manual,” *Revision A*, no. April. pp. 1–165, 2009.

[48] D. D. Pommeranchuck and I. Ivanenko, “On the maximal energy, obtainable in a betatron,” *Phys. Rev.*, vol. 65, no. 11–12, p. 343, 1944.

[49] J. Schwinger, “Electron radiation in high energy accelerators,” *Phys. Rev.*, vol. 70, p. 798, 1946.

[50] J. Schwinger, “On the Classical Radiation of Accelerated Electrons,” *Phys. Rev.*, vol. 75, no. 12, pp. 1912–1925, 1949.

[51] D. Tomboulian and P. Hartman, “Ultraviolet radiation from the Cornell synchrotron,”

Phys. Rev., vol. 91, no. 6, pp. 1577–1578, 1953.

[52] K. Codling and R. P. Madden, “Characteristics of the ‘synchrotron light’ from the NBS 180-MeV machine,” *J. Appl. Phys.*, vol. 36, no. 2, pp. 380–387, 1965.

[53] R. P. Madden and K. Codling, “Recently Discovered Auto-Ionizing States of Krypton and Xenon in the λ380–600-Å Region,” *Phys. Rev. Lett.*, vol. 54, no. 2, pp. 268–269, 1964.

[54] R. P. Madden and K. Codling, “New autoionizing atomic energy levels in He, Ne, and Ar,” *Phys. Rev. Lett.*, vol. 10, no. 12, pp. 516–518, 1963.

[55] C. Kuntz, E. Rowe, W. Gudat, A. Kotani, Y. Toyozawa, and K. Codling, *Synchrotron radiation techniques and applications,*. Berlin/Heidelberg/New York: Springer, 1979.

[56] “PLÉIADES beamline.” [Online]. Available: http://www.synchrotron-soleil.fr/Recherche/LignesLumiere/PLEIADES. [Accessed: 05-Mar-2016].

[57] A. R. Milosavljević, C. Nicolas, J. F. Gil, F. Canon, M. Réfrégiers, L. Nahon, and A. Giuliani, “Fast in vacuo photon shutter for synchrotron radiation quadrupole ion trap tandem mass spectrometry,” *Nucl. Instruments Methods Phys. Res. Sect. B Beam Interact. with Mater. Atoms*, vol. 279, pp. 34–36, 2012.

[58] A. R. Milosavljević, S. Madžunkov, D. Šević, I. Čadež, and B. P. Marinković, “Experimental determination of the differential cross-section surface for elastic electron–atom (molecule) scattering,” *J. Phys. B At. Mol. Opt. Phys.*, vol. 39, no. 3, pp. 609–623, 2006.

[59] D. J. Manura and D. A. Dahl, “SIMION Version 8.0, User Manual.” Idaho National Engineering and Environmental Laboratory, Scientific Instruments Services, 2007.

[60] J. C. Nickel, K. Imre, D. F. Register, and S. Trajmar, “Total electron scattering cross sections: I. He, Ne, Ar, Xe,” *J. Phys. B*, vol. 18, pp. 125–133, 1985.

[61] D. Manura, “Additional Notes on the SIMION HS1 Collision Model Derivation of Mean Relative Speed,” 2007.

[62] M. Pellegrini, E. M. Marcotte, M. J. Thompson, D. Eisenberg, and T. O. Yeates, “Assigning protein functions by comparative genome analysis: protein phylogenetic profiles,” *Proc. Natl. Acad. Sci. U. S. A.*, vol. 96, no. 8, pp. 4285–4288, 1999.

[63] C. B. Anfinsen, “Principles that gouvern the folding of protein chains,” *Science (80-.).*, vol. 181, no. 4096, pp. 223–230, 1973.

[64] M. Lj. Ranković, F. Canon, L. Nahon, A. Giuliani, and A. R. Milosavljević, “VUV action spectroscopy of protonated leucine-enkephalin peptide in the 6-14 eV range,” *J. Chem. Phys.*, vol. 143, no. 24, p. 244311, 2015.

[65] Judit Sztaray, A. Memboeuf, L. Drahos, and K. Vekey, “Leucine Enkephalin - A Mass Spectrometry Standard,” *Mass Spectrom. Rev.*, vol. 30, no. 298, 2011.

[66] V. S. Rakov, O. V. Borisov, and C. M. Whitehouse, “Establishing low-energy sequential decomposition pathways of leucine enkephalin and its N- and C-terminus fragments using multiple-resonance CID in quadrupolar ion guide,” *J. Am. Soc. Mass Spectrom.*, vol. 15, no. 12, pp. 1794–1809, 2004.

[67] J. Laskin, “Energetics and dynamics of fragmentation of protonated leucine enkephalin from time-and energy-resolved surface-induced dissociation studies,” *J. Phys. Chem. A*, vol. 110, no. 27, pp. 8554–8562, 2006.

[68] P. D. Schnier, W. D. Price, E. F. Strittmatter, and E. R. Williams, “Dissociation

energetics and mechanism of leucine enkephalin $(M+H)^+$ and $(2M+X)^+$ ions (X=H, Li, Na, K, and Rb) measured by blackbody infrared radiative dissociation," *J. Am. Soc. Mass Spectrom.*, vol. 8, no. 97, pp. 771–780, 1997.

[69] T. Tabarin, R. Antoine, M. Broyer, and P. Dugourd, "Specific photodissociation of peptides with multi-stage mass spectrometry," *Rapid Commun. Mass Spectrom.*, vol. 19, no. 20, pp. 2883–2892, 2005.

[70] N. C. Polfer, B. C. Bohrer, M. D. Plasencia, B. Paizs, and D. E. Clemmer, "On the dynamics of fragment isomerization in collision-induced dissociation of peptides," *J. Phys. Chem. A*, vol. 112, no. 6, pp. 1286–1293, 2008.

[71] K. Biemann, "Sequencing of peptides by tandem mass spectrometry and high-energy collision-induced dissociation.," *Methods Enzymol.*, vol. 193, no. 1981, pp. 455–479, 1990.

[72] L. Serrano-Andrés and M. P. Fülscher, "Theoretical study of the electronic spectroscopy of peptides. 1. The peptidic bond: Primary, secondary, and tertiary amides," *J. Am. Chem. Soc.*, vol. 118, no. 48, pp. 12190–12199, 1996.

[73] L. Serrano-Andrés and M. P. Fülscher, "Theoretical study of the electronic spectroscopy of peptides. III. Charge Transfer transitions in polypeptides," *J. Am. Chem. Soc.*, vol. 120, no. 9, pp. 10912–10920, 1998.

[74] L. Serrano-Andrés and M. P. Fülscher, "Theoretical study of the electronic spectroscopy of peptides. 2. Glycine and N-acetylglycine," *J. Am. Chem. Soc.*, vol. 118, no. 48, pp. 12200–12206, 1996.

[75] L. Serrano-Andrés and M. P. Fülscher, "Charge transfer transitions in neutral and ionic polypeptides: A theoretical study," *J. Phys. Chem. B*, vol. 105, no. 38, pp. 9323–9330, 2001.

[76] N. C. Polfer, J. Oomens, S. Suhai, and B. Paizs, "Infrared spectroscopy and theoretical studies on gas-phase protonated Leu-enkephalin and its fragments: Direct experimental evidence for the mobile proton," *J. Am. Chem. Soc.*, vol. 129, no. 18, pp. 5887–5897, 2007.

[77] A. R. Milosavljević, V. Z. Cerovski, M. L. Ranković, F. Canon, L. Nahon, and A. Giuliani, "VUV photofragmentation of protonated leucine-enkephalin peptide dimer below ionization energy," *Eur. Phys. J. D*, vol. 68, no. 3, p. 68, 2014.

[78] C. T. Middleton, K. de La Harpe, C. Su, Y. K. Law, C. E. Crespo-Hernández, and B. Kohler, "DNA Excited-State Dynamics: From Single Bases to the Double Helix," *Annu. Rev. Phys. Chem.*, vol. 60, no. 1, pp. 217–239, 2009.

[79] J. C. Marcum, A. Halevi, and J. M. Weber, "Photodamage to isolated mononucleotides--photodissociation spectra and fragment channels.," *Phys. Chem. Chem. Phys.*, vol. 11, no. 11, pp. 1740–51, 2009.

[80] J. C. Marcum, S. H. Kaufman, and J. M. Weber, "UV-photodissociation of non-cyclic and cyclic mononucleotides," *Int. J. Mass Spectrom.*, vol. 303, no. 2–3, pp. 129–136, 2011.

[81] V. Gabelica, F. Rosu, T. Tabarin, C. Kinet, R. Antoine, M. Broyer, E. De Pauw, and P. Dugourd, "Base-dependent electron photodetachment from negatively charged DNA strands upon 260-nm laser irradiation," *J. Am. Chem. Soc.*, vol. 129, no. 15, pp. 4706–4713, 2007.

[82] L. M. Nielsen, S. Ø. Pedersen, M. B. S. Kirketerp, and S. B. Nielsen, "Absorption by DNA single strands of adenine isolated in vacuo: The role of multiple chromophores," *J.*

Chem. Phys., vol. 136, no. 6, pp. 8–13, 2012.

[83] S. B. Nielsen, J. U. Andersen, J. S. Forster, P. Hvelplund, B. Liu, U. V. Pedersen, and S. Tomita, "Photodestruction of Adenosine 5'-Monophosphate (AMP) Nucleotide Ions in vacuo: Statistical versus Nonstatistical Processes," *Phys. Rev. Lett.*, vol. 91, no. 4, p. 048302, 2003.

[84] R. Otto, J. Brox, S. Trippel, M. Stei, T. Best, and R. Wester, "Single solvent molecules can affect the dynamics of substitution reactions.," *Nat. Chem.*, vol. 4, no. 7, pp. 534–8, 2012.

[85] N. S. Nagornova, T. R. Rizzo, and O. V. Boyarkin, "Interplay of intra- and intermolecular H-bonding in a progressively solvated macrocyclic peptide.," *Science*, vol. 336, no. 6079, pp. 320–3, 2012.

[86] B. Liu, S. B. Nielsen, P. Hvelplund, H. Zettergren, H. Cederquist, B. Manil, and B. A. Huber, "Collision-induced dissociation of hydrated adenosine monophosphate nucleotide ions: Protection of the ion in water nanoclusters," *Phys. Rev. Lett.*, vol. 97, no. 13, pp. 1–4, 2006.

[87] B. Liu, N. Haag, H. Johansson, H. T. Schmidt, H. Cederquist, S. B. Nielsen, H. Zettergren, P. Hvelplund, B. Manil, and B. A. Huber, "Electron capture induced dissociation of nucleotide anions in water nanodroplets," *J. Chem. Phys.*, vol. 128, no. 7, 2008.

[88] A. R. Milosavljević, V. Z. Cerovski, F. Canon, M. L. Ranković, N. Škoro, L. Nahon, and A. Giuliani, "Energy-dependent UV photodissociation of gas-phase adenosine monophosphate nucleotide ions: The role of a single solvent molecule," *J. Phys. Chem. Lett.*, vol. 5, no. 11, pp. 1994–1999, 2014.

[89] S. K. Kim, T. Ha, and J. Schermann, "Photoionization of 2-pyridone and 2-hydroxypyridine," *Phys. Chem. Chem. Phys.*, vol. 12, no. 14, pp. 3334–3335, 2010.

[90] S. Ø. Pedersen, K. Støchkel, C. S. Byskov, L. M. Baggesen, and S. B. Nielsen, "Gas-phase spectroscopy of protonated adenine, adenosine 5'-monophosphate and monohydrated ions.," *Phys. Chem. Chem. Phys.*, vol. 15, no. 45, pp. 19748–19752, 2013.

[91] S. B. Nielsen and T. I. Sølling, "Are conical intersections responsible for the ultrafast processes of adenine, protonated adenine, and the corresponding nucleosides?," *ChemPhysChem*, vol. 6, no. 7, pp. 1276–1281, 2005.

[92] Y. Zhao and D. G. Truhlar, "A new local density functional for main-group thermochemistry, transition metal bonding, thermochemical kinetics, and noncovalent interactions," *J. Chem. Phys.*, vol. 125, no. 19, pp. 1–18, 2006.

[93] M. Valiev, E. J. Bylaska, N. Govind, K. Kowalski, T. P. Straatsma, H. J. J. Van Dam, D. Wang, J. Nieplocha, E. Apra, T. L. Windus, and W. A. De Jong, "NWChem: A comprehensive and scalable open-source solution for large scale molecular simulations," *Comput. Phys. Commun.*, vol. 181, no. 9, pp. 1477–1489, 2010.

[94] P. G. Szalay, T. Watson, A. Perera, V. F. Lotrich, and R. J. Bartlett, "Benchmark studies on the building blocks of DNA. 1. Superiority of coupled cluster methods in describing the excited states of nucleobases in the Franck-Condon region," *J. Phys. Chem. A*, vol. 116, no. 25, pp. 6702–6710, 2012.

[95] A. Bagag, A. Giuliani, and O. Laprévote, "Atmospheric pressure photoionization mass spectrometry of nucleic bases, ribonucleosides and ribonucleotides," *Int. J. Mass Spectrom.*, vol. 264, no. 1, pp. 1–9, 2007.

[96] M. G. Rossmann and P. Argos, "Protein Folding," *Annu. Rev. Biochem.*, vol. 50, pp.

497–532, 1981.

[97] N. Jones, “Crystallography: Atomic secrets,” *Nature*, vol. 505, pp. 602–603, 2014.

[98] G. Hähner, “Near edge X-ray absorption fine structure spectroscopy as a tool to probe electronic and structural properties of thin organic films and liquids.,” *Chem. Soc. Rev.*, vol. 35, no. 12, pp. 1244–1255, 2006.

[99] Y. Zubavichus, A. Shaporenko, M. Grunze, and M. Zharnikov, “NEXAFS spectroscopy of biological molecules: From amino acids to functional proteins,” *Nucl. Instruments Methods Phys. Res. Sect. A Accel. Spectrometers, Detect. Assoc. Equip.*, vol. 603, no. 1–2, pp. 111–114, 2009.

[100] G. J. Schulz, “Resonance in the elastic scattering of electrons in helium,” *Phys. Rev. Lett.*, vol. 10, no. 3, pp. 104–105, 1963.

[101] A. R. Milosavljević, C. Nicolas, M. Lj. Ranković, F. Canon, C. Miron, and A. Giuliani, “K-Shell Excitation and Ionization of a Gas-Phase Protein: Interplay between Electronic Structure and Protein Folding,” *J. Phys. Chem. Lett.*, vol. 6, no. 16, pp. 3132–3138, 2015.

[102] O. Travnikova, C. Miron, M. Bässler, R. Feifel, M. N. Piancastelli, S. L. Sorensen, and S. Svensson, “Resonant Auger decay study of C1s → π* core-excited OCS,” *J. Electron Spectros. Relat. Phenomena*, vol. 174, no. 1–3, pp. 100–106, 2009.

[103] L. Journel, R. Guillemin, A. Haouas, P. Lablanquie, F. Penent, J. Palaudoux, L. Andric, M. Simon, D. Céolin, T. Kaneyasu, J. Viefhaus, M. Braune, W. B. Li, C. Elkharrat, F. Catoire, J. C. Houver, and D. Dowek, “Resonant double Auger decay in carbon K -shell excitation of CO,” *Phys. Rev. A - At. Mol. Opt. Phys.*, vol. 77, no. 4, pp. 1–14, 2008.

[104] J. S. Gillespie, “Substance P,” *J. Neurol. Neurosurg. Psychiatry*, vol. 40, no. 11, p. 1126, 1977.

[105] M. Lj. Ranković, A. Giuliani, and A. R. Milosavljević, “Electron impact action spectroscopy of mass / charge selected macromolecular ions : Inner-shell excitation of ubiquitin protein,” *Appl. Phys. Lett.*, vol. 108, p. 064101, 2016.

[106] C. Nicolas and C. Miron, “Lifetime broadening of core-excited and -ionized states,” *J. Electron Spectros. Relat. Phenomena*, vol. 185, no. 8–9, pp. 267–272, 2012.

[107] A. P. Hitchcock, “Core Excitation and Ionization of Molecules,” *Phys. Scr.*, vol. T31, pp. 159–170, 1990.

[108] A. P. Hitchcock, “Inner shell excitation spectroscopy of molecules using inelastic electron scattering,” *J. Electron Spectros. Relat. Phenomena*, vol. 112, no. 1–3, pp. 9–29, 2000.

[109] B. Boudaïffa, P. Cloutier, D. Hunting, M. A. Huels, and L. Sanche, “Resonant formation of DNA strand breaks by low-energy (3 to 20 eV) electrons.,” *Science*, vol. 287, no. 5458, pp. 1658–1660, 2000.

Biography

Ranković Miloš was born in 17.06.1986. Belgrade, Serbia. He attended the elementary school and electro-technical high school “Nikola Tesla” in Belgrade, Serbia. In the year of 2005. Miloš started his academic studies in physics at Faculty of Physics, University of Belgrade, at the group ”Applied physics and informatics”. In July 2012. he graduated with the average score 8.97 (out of 10) and scored 10 (out of 10) for the B.Sc. Diploma Work with the title “The application of acoustic measurements in volumetric analysis” (written in Serbian). Miloš started his Ph.D. studies in December 2012. at Faculty of Physics, University of Belgrade, at the group “Physics of atoms and molecules”. In April 2013. he has been accepted as the research associate at the Institute of Physics Belgrade and joined the project ОИ 171020 with the title “The physics of collisions and photo-processes in atomic, (bio) molecular and nano-dimensional systems”, financed by the Ministry of Education, Science and Technological Development of Serbia. Miloš is currently a research assistant and works in the “Laboratory for Atomic Collision Processes” at the Institute of Physics Belgrade.

Publications

I Papers and letters in international journals

(a) The papers that came out as contributions from this Ph.D. Thesis:

P7. **M. Lj. Ranković**, A. Giuliani and A. R. Milosavljević, “Design and performance of an instrument for electron impact tandem mass spectrometry and action spectroscopy of mass/charge selected macromolecular ions stored in RF ion trap”,
Eur. Phys. J. D **70**, 7 (2016).

P6. **M. Lj. Ranković**, A. Giuliani and A. R. Milosavljević, “Electron impact action spectroscopy of mass/charge selected macromolecular ions: inner-shell excitation of ubiquitin protein”,
Appl. Phys. Lett. **108**, 064101 (2016).

P5. **M. Lj. Ranković**, F. Canon, L. Nahon, A. Giuliani, and A. R. Milosavljević, “VUV action spectroscopy of protonated leucine-enkephalin peptide in the 6-14 eV range”,
J. Chem. Phys. **143**, 244311 (2015).

P4. A. R. Milosavljević, C. Nicolas, **M. Lj. Ranković**, F. Canon,
C. Miron and A. Giuliani, “K-Shell Excitation and Ionization of a Gas-Phase Protein: Interplay Between Electronic Structure and Protein Folding”,
J. Phys. Chem. Lett. **6**, 16 (2015).

P2. A. R. Milosavljević, V. Z Cerovski, F. Canon, **M. Lj. Ranković**, N. Škoro, L. Nahon and A. Giuliani, “Energy-Dependent UV Photodissociation of Gas-Phase Adenosine Monophosphate Nucleotide Ions: The Role of a Single Solvent Molecule”,
J. Phys. Chem. Lett. **5**, 11 (2014).

P1. A. R. Milosavljević, V. Z. Cerovski, **M. Lj. Ranković**, F. Canon, L. Nahon, and A. Giuliani, “VUV photofragmentation of protonated leucine-enkephalin peptide dimer below ionization energy”,
Eur. Phys. J. D **68**, 68 (2014).

(b) Papers outside of the topic of this Ph.D. Thesis:

P3. A. R. Milosavljević, **M. Lj. Ranković**, D. Borka, J. B. Maljković, R.
J. Bereczky, B. P. Marinković and K. Tőkési, “Study of electron transmission through a platinum tube”,
Nucl. Instr. Meth. **B** (2015).

II Invited lectures at international conferences

IT2. M. Lj. Ranković, A. Giuliani and A. R. Milosavljević, “Design and performance of an instrument for gas phase electron spectroscopy of trapped molecular ions”,
The 3rd CELINA (*Chemistry for Electron-Induced nanofabrication*) Meeting, 18 may - 20 may 2016, Kraków, Poland, STSM report (Oral presentation and abstract).

IT1. M. Lj. Ranković, F. Canon, L. Nahon, A. Giuliani and A. R. Milosavljević, “Photodissociation of protonated Leucine-Enkephalin peptide in the VUV range”,
Proc. XXIX ICPEAC15 International Conference on Photonic, Electronic and Atomic Collisions, 22 July - 28 July 2015, Toledo, Spain, Special report (Oral presentation and abstract).

III Contributions at international conferences

CI9. M. Lj. Ranković, F. Canon, L. Nahon, A. Giuliani and A. R. Milosavljević, “Photoinduced fragmentation of gas-phase protonated leucine-enkephalin peptide in the VUV range”,
Journal of Physics: Conference Series **635**, 012034 (2015).

CI8. I. Bačić, M. Lj. Ranković, F. Canon, V. Cerovski, C. Nicolas, A. Giuliani and A. R. Milosavljević, “Gas-phase X-ray action spectroscopy of protonated nanosolvated substance P peptide around O K-edge”,
Proc. WG2 Expert Meeting on Biomolecules, COST Action CM1204, XLIC - XUV/X-ray Light and fast Ions for ultrafast Chemistry, 27-30 April 2015, Poster presentation P08, p.71.

CI7. M. Lj. Ranković, V. Cerovski, F. Canon, L. Nahon, A. Giuliani and A. R. Milosavljević, “VUV action spectroscopy of bare and hydrated protonated leucine-enkephalin peptide”,
Proc. WG2 Expert Meeting on Biomolecules, COST Action CM1204, XLIC - XUV/X-ray Light and fast Ions for ultrafast Chemistry, 27-30 April 2015, Poster presentation P07, p.69.

CI6. M. Lj. Ranković, J. Rackwitz, I. Bald and A. R. Milosavljević, “Optimization of a Low-Energy Electron Gun by Electron Ray-Tracing Simulations”,
Proc. 27th Summer School and Int. Symp. on Physics of Ionized Gases – SPIG 2014, 26th - 29th August 2014, Belgrade, Serbia, Poster Presentation 1.10, pp.58-61.

CI5. A. R. Milosavljević, C. Nicolas, M. Lj. Ranković, F. Canon, C. Miron and A. Giuliani, “N K-Shell X-Ray Tandem Mass Spectrometry of Gas-Phase Ubiquitin Protein”,
Proc. 27th Summer School and Int. Symp. on Physics of Ionized Gases – SPIG 2014, 26th - 29th August 2014, Belgrade, Serbia, Poster Presentation 1.9, pp.54-57.

CI4. J. B. Maljković, M. Lj. Ranković, R. J. Bereczky, B. P. Marinković, K. Tőkési, A. R. Milosavljević, “Electron transmission through a metallic capillary”,
Proc. 26th International Conference on Atomic Collisions in Solids (ICACS-26), 13th – 18th July 2014, Debrecen, Hungary, Poster presentation P23, p.59.

CI3. A. R. Milosavljević, J. B. Maljković, R. J. Bereczky, M. Lj. Ranković, B. P. Marinković and K. Tőkési, “Transport of electrons through a long metallic microcapillary: characterization of the outgoing low-energy electron beam”,
Proc. The First Annual Meeting of COST Action CM1301 (CELINA), 19-22 March 2014, Erlangen, Germany, Poster presentation P22, p.47.

CI2. A. R. Milosavljević, M. Lj. Ranković, J. B. Maljković, R. J. Bereczky, B. P. Marinković and K. Tökési, “Kinetic Energy Distribution of Electrons Scattered Inside a Platinum Tube at the Incident Energy of 200 eV”,
Proc. 27th Summer School and Int. Symp. on Physics of Ionized Gases – SPIG 2014, 26th - 29th August 2014, Belgrade, Serbia, Poster Presentation 2.11, pp.210-213.

CI1. A. R. Milosavliević, F. Canon, V. Z. Cerovski, M. Lj. Ranković, L. Nahon, A. Giuliani, “VUV photodissociation of bare and nanosolvated protonated nucleotide isolated in the gas phase”,
Proc. 2nd NANO-IBCT Conference 2013 (Radiation Damage in Biomolecular Systems: Nanoscale Insights into Ion-Beam Cancer Therapy), 20-24 May 2013, Sopot, Poland, Poster presentation p.91.

Прилог 1.

Изјава о ауторству

Потписани-а Милош Ранковић

број уписа D29/2012

Изјављујем

да је докторска дисертација под насловом

Фотонска и електронска акциона спектроскопија трапираних биомолекуларних јона: од изолованих до наносолватисаних честица

- резултат сопственог истраживачког рада,
- да предложена дисертација у целини ни у деловима није била предложена за добијање било које дипломе према студијским програмима других високошколских установа,
- да су резултати коректно наведени и
- да нисам кршио/ла ауторска права и користио интелектуалну својину других лица.

Потпис докторанда

У Београду, 15.04.2016.

Ранковић Милош

Прилог 2.

Изјава о истоветности штампане и електронске верзије докторског рада

Име и презиме аутора Милош Ранковић

Број уписа D29/2012

Студијски програм Физика атома и молекула

Наслов рада ФОТОНСКА И ЕЛЕКТРОНСКА АКЦИОНА СПЕКТРОСКОПИЈА ТРАПИРАНИХ БИОМОЛЕКУЛАРНИХ ЈОНА: ОД ИЗОЛОВАНИХ ДО НАНОСОЛВАТИСАНИХ ЧЕСТИЦА

Ментор Др Александар Милосављевић

Потписани Милош Ранковић

изјављујем да је штампана верзија мог докторског рада истоветна електронској верзији коју сам предао/ла за објављивање на порталу **Дигиталног репозиторијума Универзитета у Београду.**

Дозвољавам да се објаве моји лични подаци везани за добијање академског звања доктора наука, као што су име и презиме, година и место рођења и датум одбране рада.

Ови лични подаци могу се објавити на мрежним страницама дигиталне библиотеке, у електронском каталогу и у публикацијама Универзитета у Београду.

Потпис докторанда

У Београду, 15.04.2016.

Ранковић Милош

Прилог 3.

Изјава о коришћењу

Овлашћујем Универзитетску библиотеку „Светозар Марковић“ да у Дигитални репозиторијум Универзитета у Београду унесе моју докторску дисертацију под насловом:

ФОТОНСКА И ЕЛЕКТРОНСКА АКЦИОНА СПЕКТРОСКОПИЈА ТРАПИРАНИХ БИОМОЛЕКУЛАРНИХ ЈОНА: ОД ИЗОЛОВАНИХ ДО НАНОСОЛВАТИСАНИХ ЧЕСТИЦА

која је моје ауторско дело.

Дисертацију са свим прилозима предао/ла сам у електронском формату погодном за трајно архивирање.

Моју докторску дисертацију похрањену у Дигитални репозиторијум Универзитета у Београду могу да користе сви који поштују одредбе садржане у одабраном типу лиценце Креативне заједнице (Creative Commons) за коју сам се одлучио/ла.

1. Ауторство

2. Ауторство - некомерцијално

[✓ 3. Ауторство – некомерцијално – без прераде]

4. Ауторство – некомерцијално – делити под истим условима

5. Ауторство – без прераде

6. Ауторство – делити под истим условима

(Молимо да заокружите само једну од шест понуђених лиценци, кратак опис лиценци дат је на полеђини листа).

Потпис докторанда

У Београду, 15.04.2016.

Ранковић Милош

1. Ауторство - Дозвољавате умножавање, дистрибуцију и јавно саопштавање дела, и прераде, ако се наведе име аутора на начин одређен од стране аутора или даваоца лиценце, чак и у комерцијалне сврхе. Ово је најслободнија од свих лиценци.

2. Ауторство – некомерцијално. Дозвољавате умножавање, дистрибуцију и јавно саопштавање дела, и прераде, ако се наведе име аутора на начин одређен од стране аутора или даваоца лиценце. Ова лиценца не дозвољава комерцијалну употребу дела.

3. Ауторство - некомерцијално – без прераде. Дозвољавате умножавање, дистрибуцију и јавно саопштавање дела, без промена, преобликовања или употребе дела у свом делу, ако се наведе име аутора на начин одређен од стране аутора или даваоца лиценце. Ова лиценца не дозвољава комерцијалну употребу дела. У односу на све остале лиценце, овом лиценцом се ограничава највећи обим права коришћења дела.

4. Ауторство - некомерцијално – делити под истим условима. Дозвољавате умножавање, дистрибуцију и јавно саопштавање дела, и прераде, ако се наведе име аутора на начин одређен од стране аутора или даваоца лиценце и ако се прерада дистрибуира под истом или сличном лиценцом. Ова лиценца не дозвољава комерцијалну употребу дела и прерада.

5. Ауторство – без прераде. Дозвољавате умножавање, дистрибуцију и јавно саопштавање дела, без промена, преобликовања или употребе дела у свом делу, ако се наведе име аутора на начин одређен од стране аутора или даваоца лиценце. Ова лиценца дозвољава комерцијалну употребу дела.

6. Ауторство - делити под истим условима. Дозвољавате умножавање, дистрибуцију и јавно саопштавање дела, и прераде, ако се наведе име аутора на начин одређен од стране аутора или даваоца лиценце и ако се прерада дистрибуира под истом или сличном лиценцом. Ова лиценца дозвољава комерцијалну употребу дела и прерада. Слична је софтверским лиценцама, односно лиценцама отвореног кода.